

Estimation of aquifer properties using electrical resistivity data in parts of Nsukka L.G.A., Enugu State

Johnson Cletus Ibuot, Daniel Nnaemeka Obiora*, Maximus C. Ugwuanyi, Agatha Ngozi Okwesili and Gladys Ujunwa Edeh

Department of Physics and Astronomy, University of Nigeria, Nsukka, Enugu State, Nigeria

*Corresponding author email: daniel.obiora@unn.edu.ng

Abstract

The study was carried out to investigate the variation of hydrodynamic parameters in parts of Nsukka Local Government Area, Enugu State, via vertical electrical sounding (VES) technique employing Schlumberger electrode configuration. The results from measured parameters were used in estimating other parameters such as hydraulic conductivity, transmissivity, porosity, formation factor and tortuosity. The third layer was delineated as aquiferous layer, with relative thickness compared to the overlying layers. The range of results obtained shows a high variation of these parameters, hydraulic conductivity ranges from 0.0989 to 0.5079m/day with an average of 0.3025m/day. Transmissivity has range between 6.5779 and 57.9546m²/day, with the average value of 18.7491m²/day; porosity ranged from 27.6863 to 29.3226%, and its average is 28.6524%. Formation factor and tortuosity range from 0.00043 to 0.00049 and 0.1129 to 0.1167 respectively. Their variation was clearly displayed on the contour maps, and this was attributed to changes in properties of subsurface, such as grain sizes, pore shapes and sizes. The result of this study will be a useful guide in exploration and abstraction of groundwater repositories in the study area.

Keywords: Aquifer, hydraulic conductivity, porosity, transmissivity, VES

Introduction

The study of groundwater resources has increased dramatically over the last decade due to man's search for potable and dependable water for domestic, agricultural and industrial purposes (Ibuot *et al.*, 2013; George *et al.*, 2015; Obiora *et al.*, 2015). The Groundwater occurs in a water bearing formation (aquifer), which the physical and hydrogeological properties vary widely from place to place. In exploring for groundwater using electrical methods, the main concern of the earth scientists is the resistivity or conductivity of rocks. The resistivity may vary with depth or the variation may be laterally. A good knowledge of the subsurface aquifer repositories is relevant for quantitative description of the groundwater repositories (Martinez *et al.*, 2008). This will contribute in solving the hydrogeological and hydrological problems such as wildcat drilling, failed or dry wells/boreholes. The

hydrogeological properties such as porosity and transmissivity make electrical methods suitable for groundwater study (Muchingami *et al.*, 2012). The electrical and hydraulic conductivities determined from the inherent rock/soil properties may be derived from the measured primary geoelectric and geohydraulic properties (George *et al.*, 2015).

The soil is characterized by voids (pores) linking the soil/rock particles and referred to as porosity, which is given by the relation;

$$\text{Porosity } (\phi) = \frac{\text{volume of pores}}{\text{total rock volume}} = \frac{V_p}{V} 1$$

Porosity depends not only on the grain composition of the soil but also on the way it is formed and pressure to which it is exposed (Halek and Svec, 1979). Porosity is a formation property whose spatial variability depends on several factors like density, clay contents, tortuosity, hydraulic conductivity (Jackson *et al.*, 1978).

Vertical electrical sounding (VES) has been used by several researchers (Dahlinet al., 2013; Loke et al., 2013; George et al., 2014; Obiora et al., 2016) since it is cheaper and faster than other methods in the investigation of subsurface. Also, its efficiency is high in areas with high contrasting resistivity, such as between the weathered overburden and bedrock unit (Telford et al., 1990). Archie's law summarized the occurrence of groundwater in rocks and soil in equation 2;

$$\rho = a\rho_w\phi^{-m} \quad 2$$

where ρ is the bulk resistivity, ρ_w is water resistivity, ϕ is porosity, a and m are empirical parameters (a is the pore geometric factor and m is the cementation factor). Cementation factor is fixed but varies with formation lithostratigraphy, permeability dependent factors and geologic age of geomaterials (Archie, 1942; Keller, 1982) according to different tabulated values.

According to Fadhil et al. (2013), tortuosity factor (pore geometry factor) relates inversely with the formation hardness and geologic age of formation. A pore geometry factor of 0.62 and cementation factor of 2.15 were realized by Winsauer et al. (1952) who experimented on compacted sandstones as shown in the Humble equation:

$$F = \frac{0.62}{\phi^{2.15}} \quad 3$$

where F is the formation factor.

Tortuosity (τ) is the ratio of actual distance travelled by the fluid through the porous media to the assumed straight pore channel paths. It is estimated using the relation;

$$\tau = (F\phi)^{1/2} \quad 4$$

This geohydraulic parameter depends on the geometry, nature of grain size, non-uniformity of pore grain orientations and type of pore grains and pore channels and hydraulic pressure (George *et al.*, 2015).

The objectives of this study are to determine the depth, thickness and extent

of potential water bearing formations and to generate map of the shallow subsurface showing the variations of aquifer parameters in the study area. These were achieved via nine vertical electrical sounding points employing Schlumberger electrode configuration and constraint with a nearby borehole in the study area.

Location and Geology of the study Area

The study area is located within latitudes 6°52'N and 6°58'N and longitudes 7°20'E and 7°27'E and covers part of Nsukka and Igbo-Eze South local Government Areas of Enugu State (Figure 1). The region has an undulating topography and the elevation varies between 359 m and 413 m above sea level. The study area is accessible through a network of major and minor roads in addition to several foot paths. The study area is found within the Anambra sedimentary basin whose rocks are the Upper Cretaceous in age. The geologic formations are the upper Nsukka Formation and the underlying Ajali Sandstone. The major land forms typical of this area are residual hills and dry valleys. These two major geomorphic structures are the resultant effect of weathering and differential erosion of clastic materials which are remnant of the Nsukka Formation. Ofomata (1967) recognized five types of these residual hills according to their shapes. These residual hills sometimes form outliers on the Ajali Sandstone and are capped by thick deposit of red earthy material and laterite. These laterites are permeable, particularly those of Ajali Sandstone thereby allowing easy water percolation into the groundwater table during the rainy season. The Ajali Sandstone consists mainly of medium to coarse grained characteristically white coloured Sandstone but may be occasionally iron stained. The Sandstone is very permeable and readily recharged in its outcrop belt around the Idah-Nsukka-Enugu escarpment (Agagu *et al.*, 1985). Nsukka Formation has a significant groundwater

potential and hosts a number of low to moderate yield wells in Nsukka areas. A number of perched aquifer emerges from it and quite a number of low yield wells also tap the perched aquifer in Nsukka areas (Ezeigbo and Ozioko, 1987). The laterite capping in the area is aquiferous because it is porous and permeable due to its vesicular nature. These lateritic caps may be

underlain by less pervious clay beds, leading to the formation of perched aquifer in some areas. Perched aquifer discharge is seen in Asho hill in Nsukka, Aku hill in Obukpa, Abile hill in Ibagwa-aka and Awula in Ibagwa-Ani. In many areas however, the laterite cap has been washed out and the clay bed underlying is missing, hence perched aquifer does not exist.

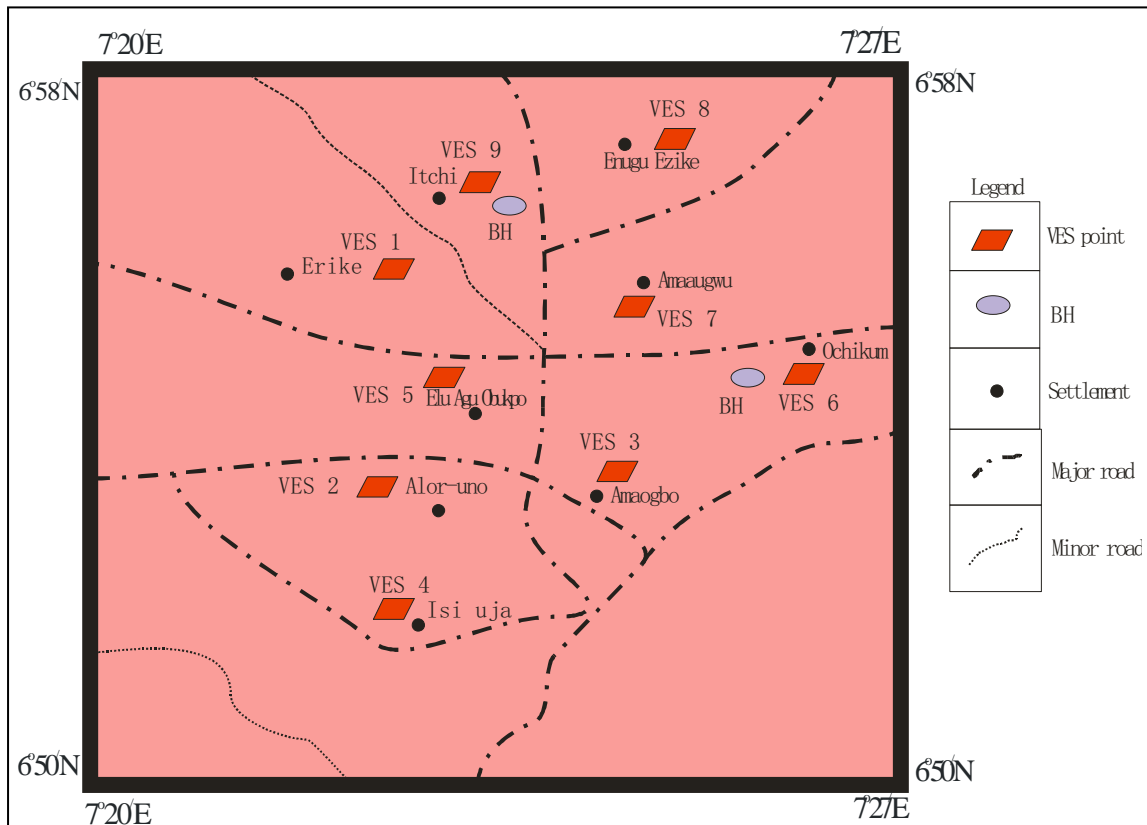


Figure 1: Map of the study area showing the VES points

Materials and Methods

The resistivity survey was carried out using a signal averaging system branded ABEM SAS 300 Terrameter and its accessories. The half current electrode ($AB/2$) spacing ranged from 1.5 to 500m, while the half potential electrode ($MN/2$) spacing ranged from 0.5 to 42m and it was completed with nine VES sounding stations. The apparent resistivity ρ_a for each electrode was calculated using equation 5:

$$\rho_a = \pi \left(\frac{a^2}{b} - \frac{b}{4} \right) R = KR \tag{5}$$

where the geometric factor, $K = \pi \left(\frac{a^2}{b} - \frac{b}{4} \right)$
 $a = \frac{AB}{2}, b = \frac{MN}{2}, R =$ apparent resistance in Ω .

The measured field parameters were used as input parameters in a WINRESIST software to generate a set of curves (Figures 2 &3) from which the true values of resistivity, depths and thicknesses of each layer within the maximum current electrode separation were obtained. The results were constraint using borehole data from nearby boreholes (Figure 4).

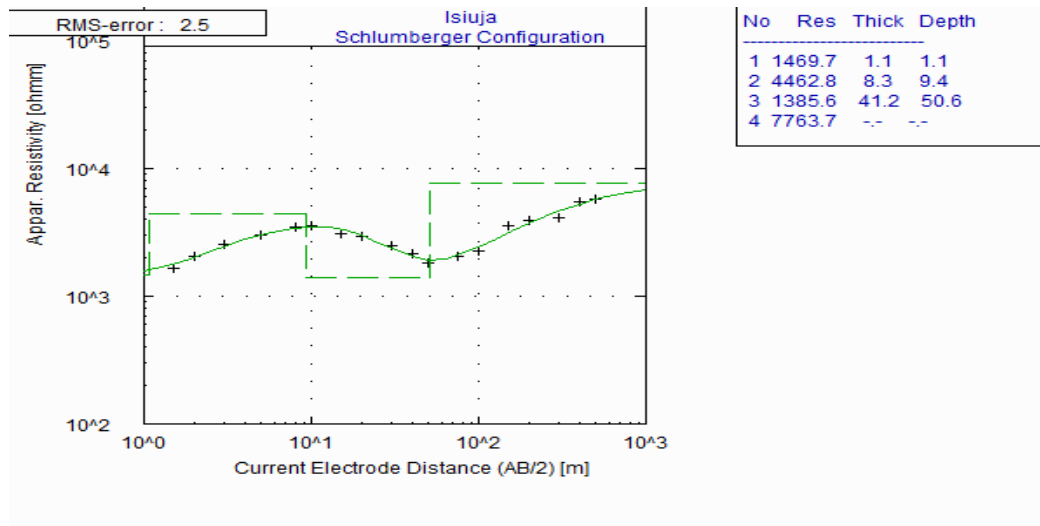


Figure 2: Typical VES curve for Isiuja (VES 4)

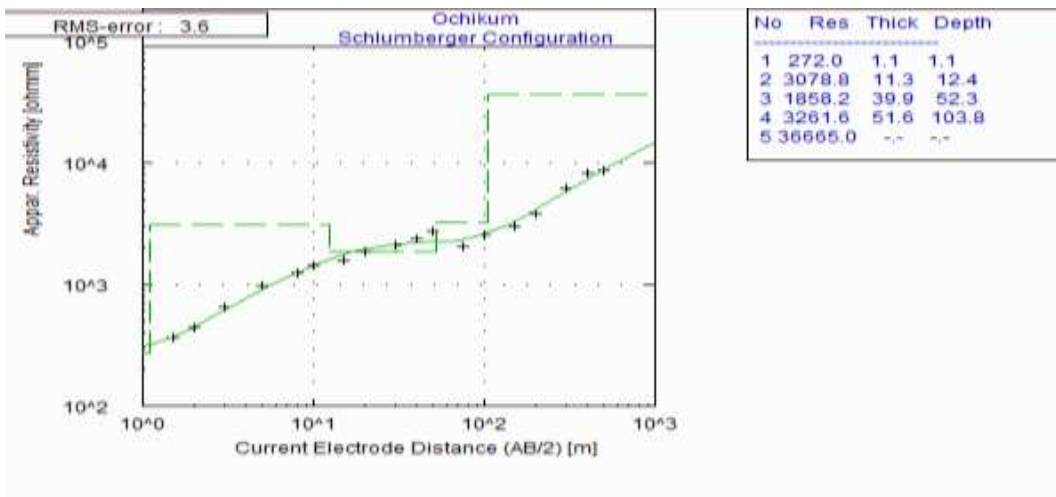


Figure 3: Typical VES curve for Ochikum (VES 6)

The values of aquifer resistivity and thickness were used to compute other parameters (hydraulic conductivity, transmissivity, porosity, formation factor and tortuosity).

The hydraulic conductivity (K) which depends on the intrinsic permeability of the material, degree of saturation, fluid viscosity and particulate size distribution of geounit (Niwas and Celik, 2012) was computed using equation 6 from(Heigold et al., 1979);

$$K = 386.40R_{rw}^{-.93283} \tag{6}$$

where R_{rw} is the resistivity of the aquifer. The expression can provide a general idea of water-producing capabilities of the

aquifer from surficial electrical methods (Heigold et al., 1979). Niwas and Singhal (1981) established a relationship for estimating aquifer transmissivity (equation 7). Transmissivity describe the ability of an aquifer to transmit water, which plays an important role in abstraction.

$$T = \frac{KS}{\sigma} = Kh \tag{7}$$

where σ is the inverse of resistivity (conductivity), h is the aquifer thickness, S is the longitudinal conductance and K is the hydraulic conductivity.

Porosity exerts significant influence on other formation properties such as transverse resistance, longitudinal conductance and transmissivity (Robinson

and Metternicht, 2006; Soupios *et al.*, 2007). Equation 8 which relates effective porosity to hydraulic conductivity was established by Marotz (1968) using a sandstone sample;

$$\phi_{eff} = 25.5 + 4.5 \ln K \quad 8$$

Results and Discussion

The results revealed the subsurface to be highly heterogeneous, ranging from three to five geoelectric layers (Table 1), with their depths and thicknesses within the maximum current electrode separation. The lithologs (Figure 4) from two existing boreholes in the area reveal the subsurface geological formations to consist of lateritic sand, sandstone, medium-coarse grained sandstone, extremely coarse sandstone and well-sorted scattered medium grained sandstone. The lithologs were used to constrain the result from VES models. The fifth layer is undefined in most of the VES stations except in VES 6 and 9. The

variation of resistivity across the study area indicates the top layer lithology as dominated by lateritic sand. The second layer indicates the presence of sandstone and is underlain by a relatively thick layer which is medium-coarse grained sandstone. The third layer is relatively thick and more resistive compared to the overlying layers, and the zone constitutes the aquifer in the study area. The values of aquifer resistivity and thickness were used to compute the hydraulic parameters (Table 2). The contour map (Figure 5) shows variation of resistivity in the study area; high aquifer resistivity was observed across the E-SW part of the study area; and the resistivity falls within the part with relatively high aquifer thickness (Figure 6). The hydraulic conductivity and transmissivity were computed from equations 6 and 7 respectively, and ranged from 0.0989 to 0.5079 m/day and

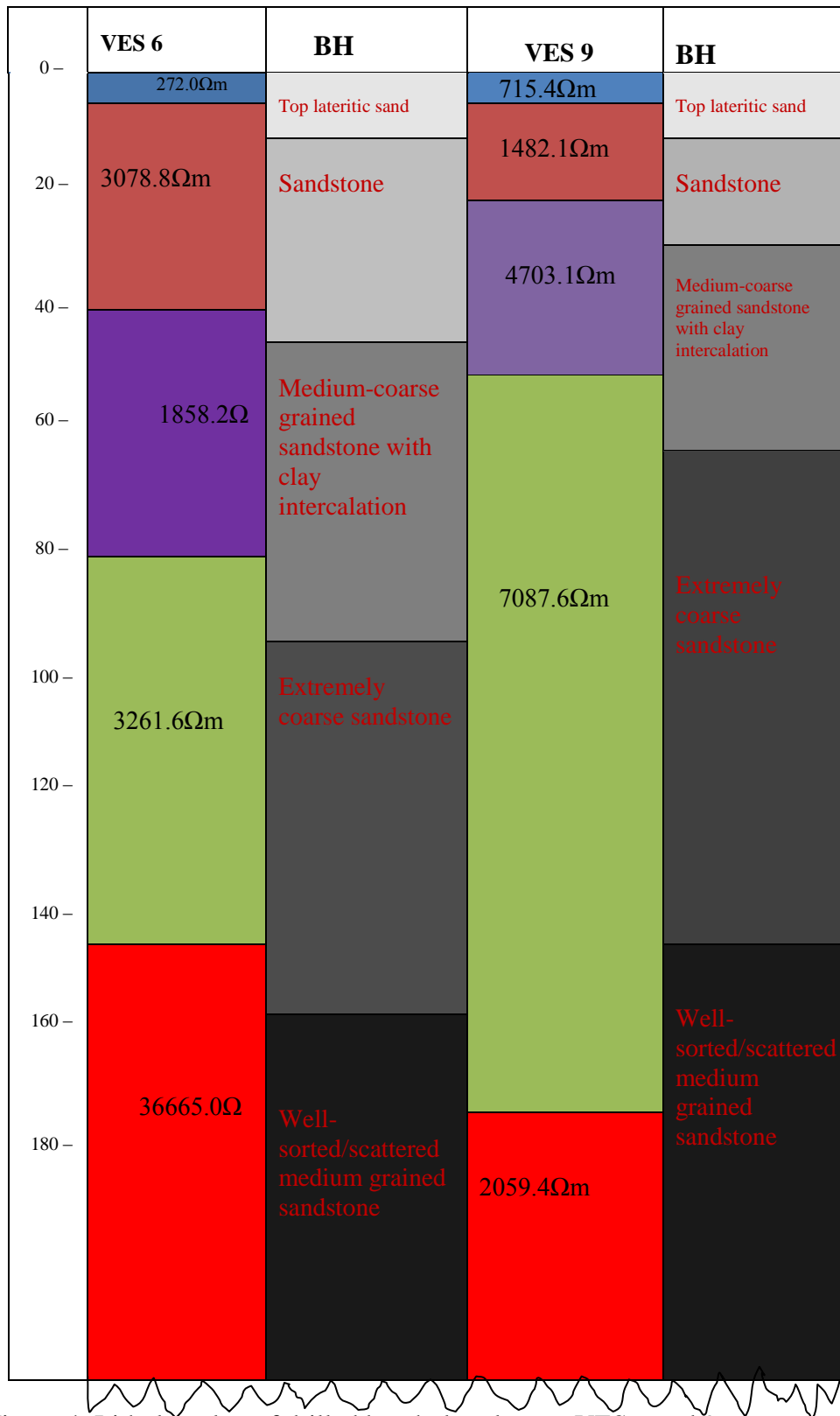


Figure 4: Lithology log of drilled boreholes close to VES 6 and 9.

6.5779 to 57.9546m²/day. Hydraulic conductivity controls the rate at which groundwater flow under a given hydraulic

gradient, and groundwater flow directions could be predicted from the zone having high hydraulic conductivity.

The contour map (Figure 7) shows the variation of hydraulic conductivity, it is observed to be high in the northern part of the study area and low in the southern part. Comparing the resistivity contour map

(Figure 5) with Figure 7, it shows an inverse relationship, where zones with high aquifer resistivity correspond to zone with low hydraulic conductivity.

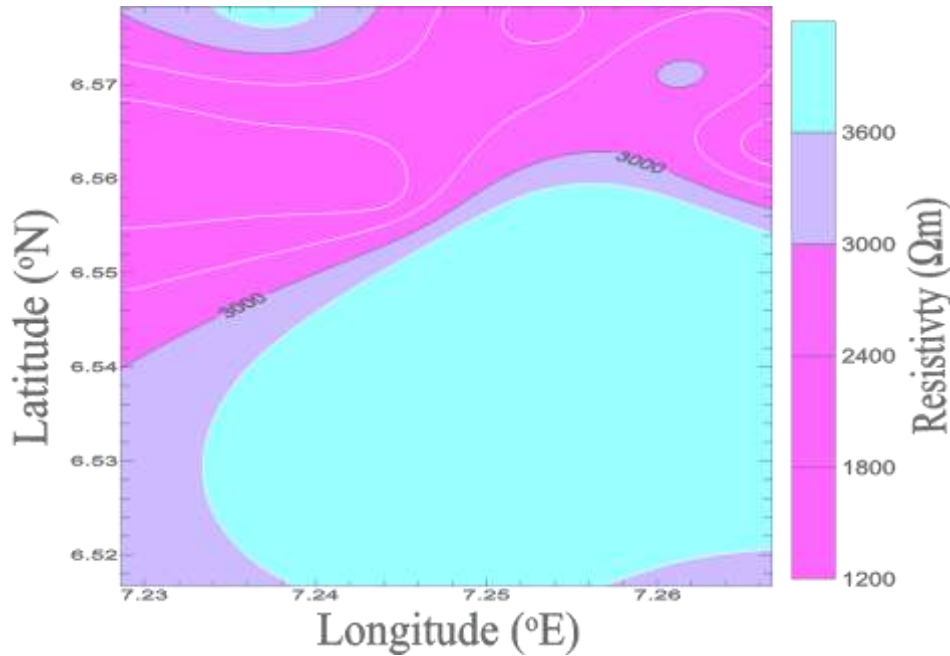


Figure 5: Contour map of aquifer resistivity

Table 1: Summary of results from computer modelling for nine sounding stations

VES No	Location	No of layers	Curve types	Layer Resistivity (Ωm)					Thickness (m)					Depth (m)				
				ρ_1	ρ_2	ρ_3	ρ_4	ρ_5	h_1	h_2	h_3	h_4	h_5	d_1	d_2	d_3	d_4	d_5
1	Erike	4	KH	1022.9	1391.1	3332.4	16034.4	-	3.6	24.0	81.3	-	-	3.6	27.7	109.0	-	-
2	Alor-uno	3	H	2155.3	1272.3	2836.1	-	-	2.9	13.4	-	-	-	2.9	16.2	-	-	-
3	Amaogbo	4	KH	772.2	4823.5	1436.9	20998.8	-	0.9	9.2	34.1	-	-	0.9	9.2	34.1	-	-
4	Isuija	4	KH	1469.7	4462.8	1385.6	7763.7	-	1.1	8.3	41.2	-	-	1.1	9.4	50.6	-	-
5	Eluagu	4	AA	127.0	794.4	4107.1	18144.4	-	0.9	16.7	175.0	-	-	0.9	17.6	192.6	-	-
6	Ochikum	5	KHA	272.0	3078.8	1858.2	3261.6	366665.0	1.1	11.3	39.9	51.6	-	1.1	12.4	52.3	103.8	-
7	Amaugwu	4	KH	121.6	1989.4	1226.6	4261.2	-	3.2	5.2	114.1	-	-	3.2	8.4	122.5	-	-
8	Ibagwa	4	AA	489.4	1442.3	4111.3	7517.2	-	1.0	16.6	42.6	-	-	1.0	17.6	60.3	-	-
9	Itchi Rd Ibagwa	5	AAA	715.4	1482.1	4703.1	7087.6	2059.4	1.9	12.2	29.3	121.8	-	1.9	14.1	43.4	165.2	-

Table 2: Computed aquifer geohydraulic parameters.

VES No	Location	Longitude (°E)	Latitude (°N)	Aquifer resistivity (Ωm)	Aquifer thickness (m)	Hydraulic conductivity (m/day)	Transmissivity (m ² /day)	Porosity (%)	Formation factor	Tortuosity
1	Erike	7.2633	6.5167	3332.4	81.3	0.2000	16.2553	28.3903	0.000466	0.1150
2	Alor-Uno	7.2667	6.5633	1272.3	13.4	0.4909	6.5779	29.2885	0.000436	0.1130
3	Amaogbo	7.2533	6.5767	1436.9	24.9	0.4382	10.9118	29.1750	0.000439	0.1132
4	Isuija	7.2438	6.5582	1385.6	41.2	0.4533	18.67757	29.2089	0.000438	0.1131
5	Eluagu	7.2400	6.5387	4107.1	175.0	0.1645	28.79129	28.1953	0.000473	0.1154
6	Ochikum	7.2615	6.5712	3261.6	51.6	0.2040	10.52576	28.4103	0.000465	0.1149
7	Amaugwu	7.2286	6.5646	1226.6	114.1	0.5079	57.95461	29.3226	0.000434	0.1129
8	Ibagwa	7.2377	6.5783	4111.3	42.6	0.1644	7.001942	28.1943	0.000473	0.1154
9	Itchi Rd. Ibagwa	7.2549	6.5497	7087.6	121.8	0.0989	12.04546	27.6863	0.000491	0.1167
	Average			3024.6	73.9889	0.3025	18.7491	28.6524	0.00046	0.1144
	Maximum			7087.6	175.0000	0.5079	57.3226	29.3226	0.00049	0.1167
	Minimum			1226.6	13.4000	0.0989	6.5779	27.6863	0.00043	0.1129

The contour map (Figure 8) shows the spatial distribution of aquifer transmissivity in the study area. Transmissivity increases in the eastwest direction and may be affected by the

uneven distribution of changes in the water-bearing zones, and its distribution shows the variational trend in size and potential of groundwater in the study area (George et al., 2015).

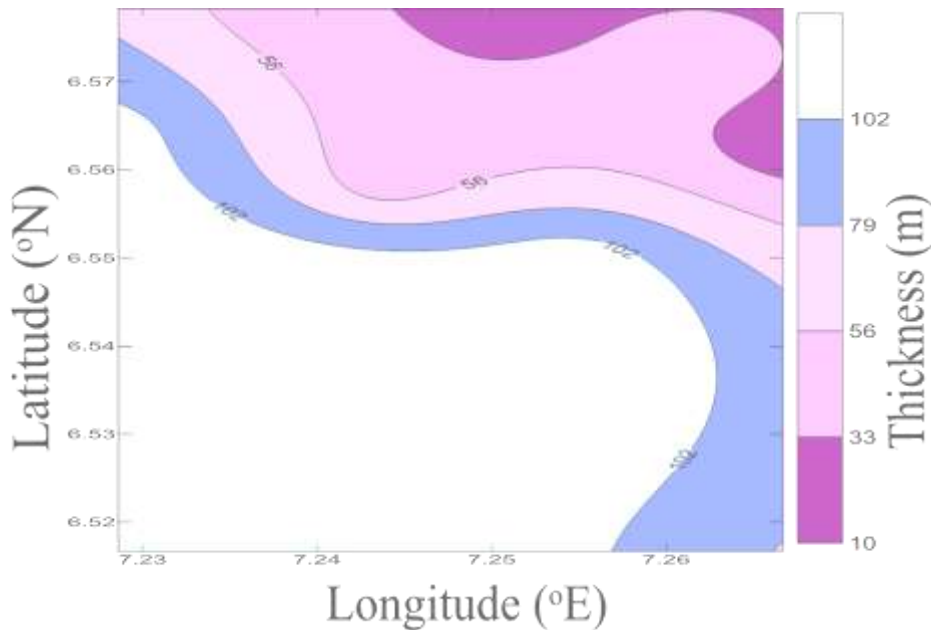


Figure 6: Contour map of aquifer thickness

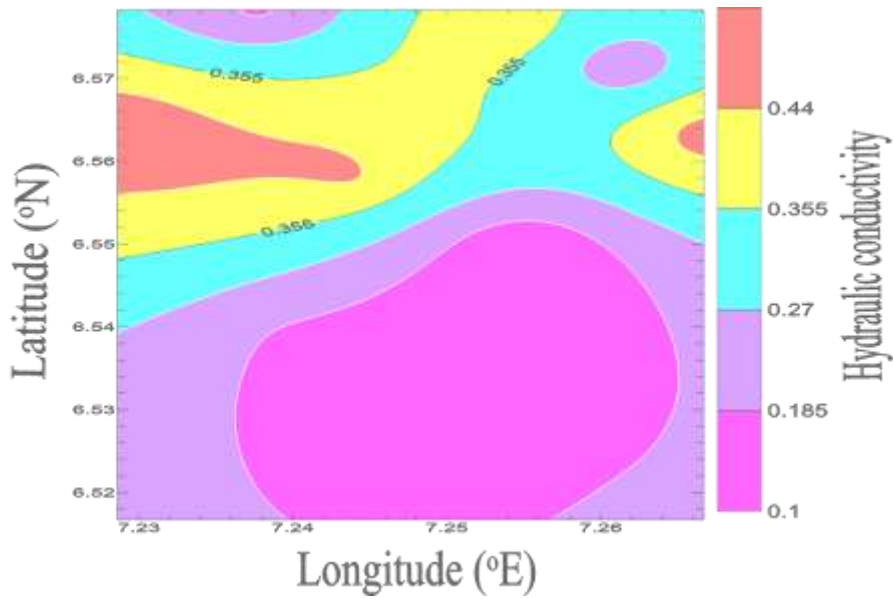


Figure 7: Contour map of hydraulic conductivity distribution.

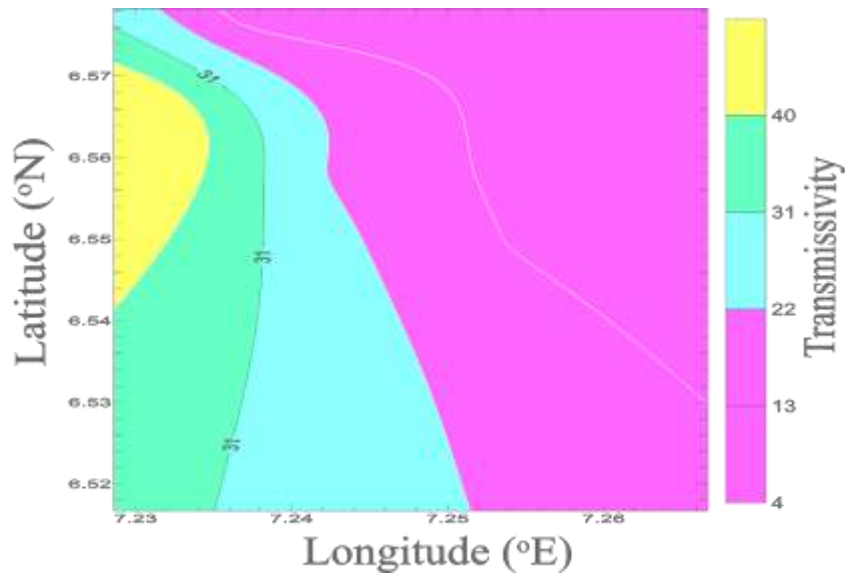


Figure 8: Contour map showing the variation of aquifer transmissivity

The aquifer porosity ranged from 27.6863% to 29.3226% with an average value of 28.65245% indicating a sandstone aquifer. The map (Figure 9) shows its variation, as low porosity is observed in

the southeastern zone and is in the reverse order to formation factor (Figure 10). This means that where porosity increases, formation factor decreases.

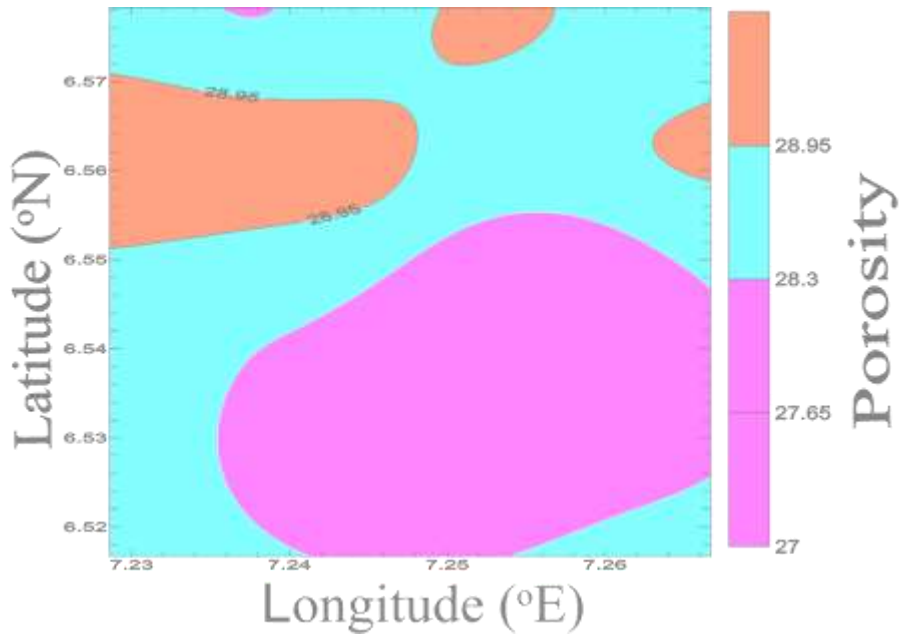


Figure 9: Contour map showing the distribution of porosity

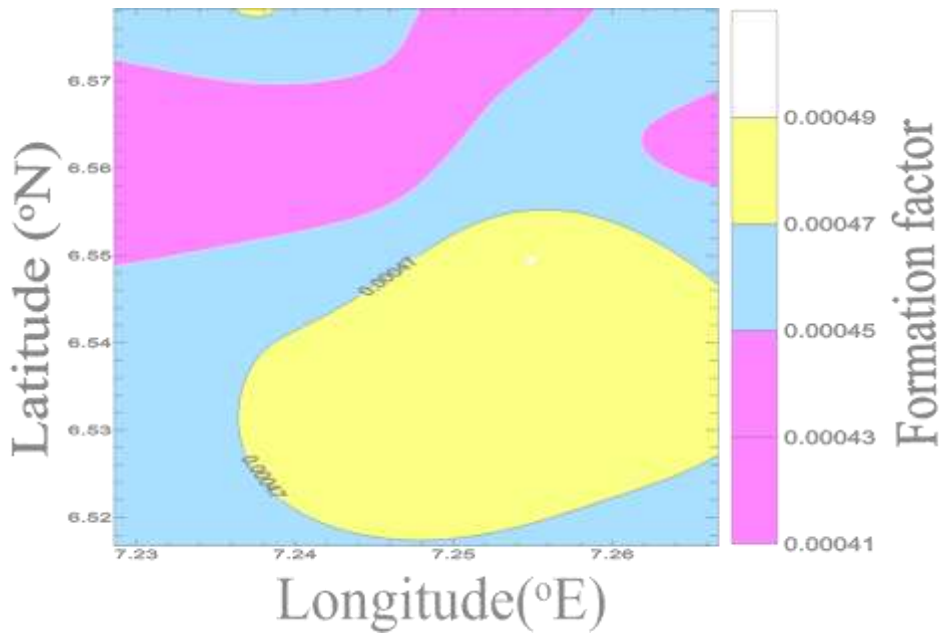


Figure 10: Contour showing variation of aquifer formation factor

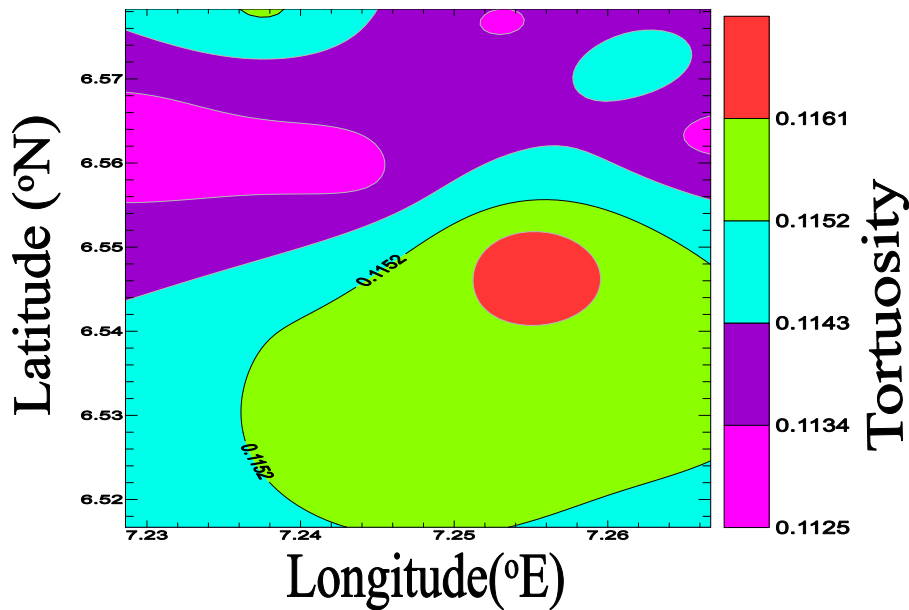


Figure 11: Contour map showing variation of tortuosity

Figure 11 is a contour map displaying the variation of tortuosity which is a parameter that depends on the formation pore system. It is observed from the map that tortuosity increases with formation factor and decrease in porosity. This may be due to changes in grain size of subsurface geomaterials. The high range observed from the distribution of these parameters is an indication that the sandstone aquifers are not well sorted and also due to the influence of geohydrodynamic properties.

Conclusion

The results from this study have delineated the subsurface hydraulic properties and their interrelationship with the groundwater repositories. These properties play important roles in groundwater abstraction and management. The resistivity of the subsurface shows the presence of clay sandstone mixture in the geological unit considered. The study has identified their interrelationship with the aquifer zone and their variations across the study area. Using the measured aquifer resistivity and thickness, estimation of the geohydrodynamic parameters were obtained. The results show the variation of these parameters across the study area, their interdependent on each other and may be influenced by the grain size

distribution of the aquifer geomaterials. The contour maps show the hydrogeological importance of these properties and how they can be useful reference in groundwater development and abstraction in areas where no geophysical study have been carried out within the study area.

References

- Agagu, O.K., Fayose, E.A. & Paters, S.W. (1985). Stratigraphy and Sedimentation in the senonian Anambra basin of Eastern Nigeria. *J. Min. Geol.*, 2, pp. 25-35.
- Archie, G.E. (1942). The electrical resistivity logs as an aid in determining some reservoir characteristics. *Transactions of the American Institute of Mineralogical and Metallurgical Engineers*, 146, 54-62.
- Dahlin, T. (2001). The development of DC resistivity imaging techniques. *Computers and Geosciences*, 27(9), 1019-1029.
- Ezeigbo, H.I. & Ozioko, D.C. (1987). Towards efficient rural-water supply to Nsukka area and environs. *Proc.*, 2nd NISWASA-Symposium Lagos.

- Fadhil, S.K., Ariffin, S., Ahmad, K. (2013). A review in correlation between cementation factor and carbonate rock properties. *Life Science Journal*, 10 (4), 2451–2458.
- George, N.J., Nathaniel, E.U. & Etuk, S.E. (2014). Assessment of economically accessible groundwater reserve and its protective capacity in eastern Obolo Local Government Area of Akwa Ibom State, Nigeria, using electrical resistivity method. *International Journal of Geophysics*, 2014, 1-10.
- George, N.J., Emah, J.B., & Ekong, U.N. (2015). Geohydrodynamic properties of hydrogeological units in parts of Niger Delta, Southern Nigeria. *Journal of African Earth Sciences*, 105, 55-63.
- Halek, V. & Svec, J. (1979). *Groundwater Hydraulics*. Elsevier Scientific Publishing Company, New York.
- Heigold, P.C., Gilkeson, R.H., Cartwright, K. & Reed, P.C. (1979). Aquifer Transmissivity from Surficial Electrical methods. *Ground Water*, 17(4), 338 – 345.
- Ibuot, J.C., Akpabio, G.T., & George, N.J. (2013). A survey of the repositories of groundwater potential and distribution using geoelectrical resistivity method in Itu Local Government Area (L.G.A), Akwa-Ibom State, Southern Nigeria. *Central European Journal of Geosciences*, 5(4), 538-547.
- Jackson, P.D., Taylor-Smith, D. & Stanford, P.N. (1978). Resistivity-porosity particles shape relationships for marine sands. *Geophysics*, 43, 1250-1268.
- Keller, G.V. (1982). Electrical properties of rocks and minerals. In: R.S. Carmichael (Ed.), *Handbook of Physical Properties of Rocks*, 1, pp 217-293, CRC Press, Boca Raton, FL.
- Loke, M.H., Chambers, J.E., Rucker, D.F., Kuras, O. & Wilkinson, P.B. (2013). Recent developments in direct-current geoelectrical imaging method. *Journal of Applied Geophysics*, 95, 135-156.
- Marotz, G. (1968). *Technische Grundlagen einer Wasserspeicherung im natürlichen Untergrund*. Verlag Wasser und Boden, Hamburg.
- Martínez, A.G., Takahashi, K., Núñez, E., Silva, Y., Trasmonte, G., Mosquera, K. & Lagos, P. (2008). A multi-institutional and interdisciplinary approach to the assessment of vulnerability and adaptation to climate change in the Peruvian Central Andes: problems and prospects. *Advances in Geosciences Journal*, 14, 257–260.
- Muchingami, I., Hlatywayo, D.J., Nel, J.M. & Chuma, C. (2012). Electrical resistivity survey for groundwater investigations and shallow subsurface evaluation of the basaltic-greenstone formation of the urban Bulawayo aquifer. *Physics and Chemistry of the Earth*, 50, 44–51.
- Niwas, S. & Celik, M. (2012). Equation estimation of porosity and hydraulic conductivity of Ruhrtal aquifer in Germany using near surface geophysics. *Journal of Applied Geophysics*, 84, 77-85.
- Niwas, S. & Singhal, D.C. (1981). Estimation of aquifer transmissivity from Dar Zarrouk parameters in porous media. *Hydrology*, 50, 393-399.
- Obiora, D.N., Ajala, A.E. & Ibuot, J.C. (2015). Evaluation of aquifer protective capacity of overburden units and soil corrosivity in Makurdi, Benue State, Nigeria, using electrical resistivity method. *Journal of Earth System Science*, 124(1), 125-135.

Obiora, D.N., Ibuot, J.C. & George, N.J. (2016). Evaluation of aquifer potential, geoelectric and hydraulic parameters in Ezza North, southeastern Nigeria, using geoelectricsounding. *Int. J. Environ. Sci. Technol.*, 13, 435-444.

Ofomata, G. E. K. (1967). Landforms on the Nsukka Plateau of Eastern Nigeria. *Nig. Geol.*, 1(10), 3-9.

Robinson, T.P. & Metternicht, G. (2006). Testing the performance of spatial interpolation techniques for mapping soil properties. *Comput. Electron. Agric.*, 50, 97-108

Soupios, P.M., Kouli, M., Vallianatos, F., Vafidis, A. & Stavroulakis, G. (2007). Estimation of aquifer hydraulic parameters from surficial geophysical methods- A case study of Keritis Basin in Chania (Crete-Greece). *Journal of Hydrology*, 338, 122 - 131.

Telford, W.M., Geldart, L.P., Sheriff, R.E. and Keys, D.A. (1990). *Applied Geophysics*, 2nd ed., Cambridge: Cambridge University Press.

Winsauer, W.O., Shearin, H.M., Masson, P.H. & Williams, M. (1952). Resistivity of brine saturated sands in relation to pore geometry. *Bull. Am. Assoc. Pet. Geol.* 36, 253-277.

Syntheses, Characterization and Antibacterial Screening of Nd(III) and Gd(III) Complexes of N-(benzothiazol-2-yl)benzenesulphonamide

Dorathy Nkemdilim Ezugwu^{1*}, Nnamdi Lawrence Obasi¹ and Ponnadurai Ramasami²

¹Department of Pure and Industrial Chemistry, University of Nigeria, 410001, Nsukka.

²Computational Chemistry Group, Department of Chemistry, Faculty of Science, University of Mauritius, Réduit, 80832, Mauritius, E-mail: ramchemi@intnet.mu

Corresponding author E-mail: * ichnkem@gmail.com

Abstract

Reaction of the DMF solution of the ligand, N-(benzothiazol-2-yl)benzenesulphonamide with aqueous solutions of Nd(III) and Gd(III) nitrates gave the respective metal complexes. These compounds were characterized using molar conductivity measurement, elemental microanalysis, IR, ¹H NMR, ¹³C NMR and mass spectral studies. The compounds were also, screened for in vitro antibacterial activity against a gram-positive bacteria strain (Staphylococcus aureus) and some gram-negative bacteria strains (Pseudomonas aeruginosa, Proteus spp, E. coli strain 6 and E. coli strain 13). Their antibacterial activities were compared with ciprofloxacin and gentamycin. The neodymium(III) complex was found to be more active against the tested bacteria strains than the gadolinium(III) complex and the standard drugs used.

Keywords: Complexes, neodymium, gadolinium, antibacterial activity.

Introduction

An enhanced global search for potent antimicrobial agent has led to the development of synthetic antimicrobial agent with a wide spectrum of activity (Gootz., 1990). Interestingly, sulfanilamide was the first synthetic antimicrobial agent active against a wide range of infections (Williamson *et al.*, 2007; Rosaleenet *al.*, 2012; Claudiuet *al.*, 2001; Jesmanet *al.*, 2011). Further development led to a range of sulphonamides which proved effective against most gram-positive and many gram-negative bacteria strains. Therefore, sulphonamides are the oldest antimicrobial agents, and the best bacteriostatic agents.

Their mode of action, efficacy, safety and pharmacological properties are well known. They act as competitive enzyme inhibitors and block the biosynthesis of the vitamin, folic acid, in bacterial cells by inhibiting the enzyme, dihydropteroatesynthetase, responsible for linking together the component parts of

folic acid (Rosaleenet *al.*, 2012; Lacey, 1979). This disrupts the biosynthesis of nucleic acids which leads to the cessation of cell growth and division. Thus, sulphonamides do not actively kill bacterial cells rather they prevent the cells from dividing and spreading. This gives the body's own defense systems enough time to gather their resources and wipe out the invader.

They remained the drugs of choice in the treatment of infectious diseases until the discovery of penicillins which largely superseded it in the fight against bacterial infections (Davenport, 2012). Due to the greater efficiency of penicillins, the use of sulphonamides became insignificant for a long period of time. However, the interest on sulphonamides has been revived with the discovery of new breed of longer lasting sulphonamides, like Sulphamethoxine, which are so stable in the body and can be taken only once a week.

Presently, they are used to treat many kinds of infections caused by bacteria and certain other microorganisms (Paige and Tollenfson, 2003; Korsinczky *et al.*, 2004). For instance, they are used to treat urinary tract infections, ear infections, frequent or long-lasting bronchitis, bacterial meningitis, certain eye infections, traveler's diarrhea. Particularly, silver sulfadiazine, an ointment containing a sulphonamide is valuable for the treatment of infections associated with severe burns (Obasiet *al.*, 2013). Also, the combination drug trimethoprim/sulfamethioxazole (TMP-SMZ) remains in use for many infections, including those associated with HIV infection (Lacey., 1979). It is mostly useful for prevention and treatment of *Pneumocystis carinii* pneumonia (PCP) which has been the most dangerous of the infections associated with HIV infection. Interestingly, sulphonyl chlorides are often chosen as building blocks in medicinal chemistry due to their ability to easily react with heterocyclic amines to create complex sulphonamides which are used in the treatment of infectious diseases (Anetaet *al.*, 2014). It has been reported that the metal complexes of sulfa drugs promote rapid healing of skin disorder. For instance, zinc(II) sulfadiazine is used in preventing bacterial infections in burnt animals and silver(I) sulfadiazine complex for human burnt treatment (Obasiet *al.*, 2013).

Lanthanides are the subject of increasing interest in bioinorganic and coordination chemistry. This is because of their successful applications as diagnostic tools in biomedical analysis (magnetic resonance imaging contrast agents) and as effective catalysts for the hydrolytic cleavage of phosphate ester bonds (Picard *et al.*, 2006; Aimeet *al.*, 2006; Franklin, 2001). Lanthanide complexes have been found to exhibit anticancer and fungicidal properties (Sharma *et al.*, 1981). However, despite their biological significance and potential applications, lanthanides complexes are yet to be adequately studied

(Raafatet *al.*, 2008; Sindhuet *al.*, 2013). This is because complexation of lanthanide(III) ions differs from that of d-block elements.

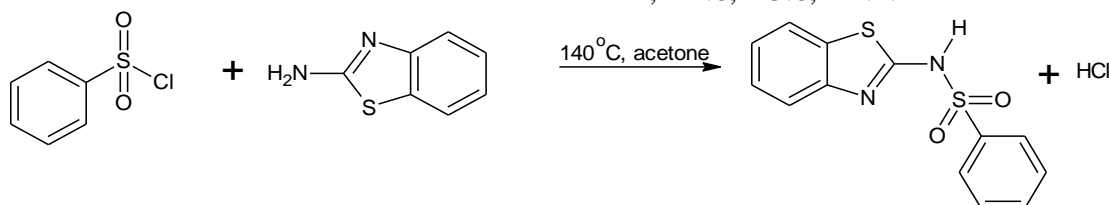
Lanthanide ions do not display pronounced stereochemical preferences for particular bonding modes. Consequently, the development of tailored receptors for Ln(III) remains a challenge to synthetic chemists. The synthesis, spectroscopic studies and antimicrobial screening of N-(benzothiazol-2-yl)benzenesulphonamide and its Cu(I), Ni(II), Mn(II), Co(II), and Zn(II) Complexes has earlier been reported (Obasiet *al.*, 2012). The spectral analyses confirmed the structures of the compounds synthesized and all the compounds showed varying activities against the cultured typed bacteria and fungi used. In this communication, the syntheses, characterization of Nd(III) and Gd(III) complexes of N-(benzothiazol-2-yl)benzenesulphonamide and their antimicrobial study are reported. Hence, this work is aimed at investigating the effect of coordination on the antibacterial activity.

Experimental

Reagents and Apparatus

All the reagents were of analytical grade and were used as supplied without further purification. The analyses of the ligand and its metal complexes were obtained as follows: The melting points were determined using Fischer Johns melting point apparatus at Department of Pure and Industrial Chemistry, University of Nigeria, Nsukka. Molar conductivity measurement were carried out at a concentration of 10^{-3} M using DMSO as solvent on WTW conductivity meter, LF 90, at National Centre for Energy Research Development, University of Nigeria, Nsukka. The elemental microanalysis was recorded on Euro EA 3000 Dual CHNS analyzer at Department of Chemistry, University of Mauritius. The IR spectra

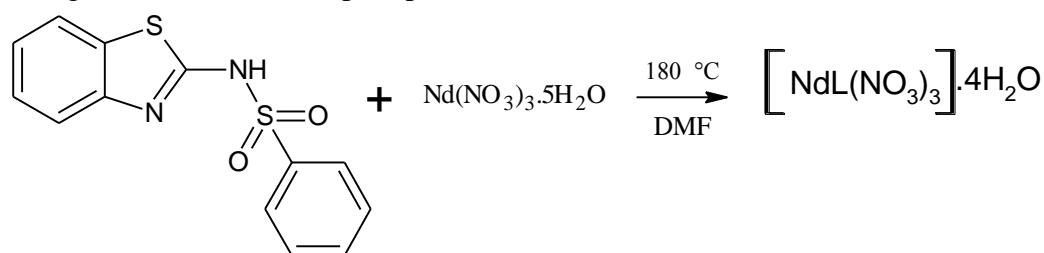
were recorded on FTIR-8400S Fourier transform infrared spectrophotometer (SHIMADZU) at National Research Institute for Chemical Technology (NARICT), Zaria, Kaduna State, Nigeria. The ^1H and ^{13}C NMR spectra were recorded on Bruker spectrometer spin 250, using DMSO-d_6 as solvent and TMS as an internal standard at Department of Chemistry, University of Mauritius. The Mass spectrometric analysis were recorded on Mass spectrometer-MICROMASS QUATRO II triple quadrupole Mass spectrometer at Department of Chemistry, Supramolecular Inorganic Chemistry Unit, Indian Institute of Technology, Kanpur, India.



Scheme 1: Synthesis of N-(benzothiazol-2-yl)benzenesulphonamide, [L]

Synthesis of the neodymium(III) complex, $[\text{NdL}(\text{NO}_3)_3] \cdot 4\text{H}_2\text{O}$

This was synthesized by the reaction of solution of the ligand, N-(benzothiazol-2-yl)benzenesulphonamide (0.58 g; 2.0 mmol) in DMF (10 mL) with aqueous solution of neodymium(III) nitrate pentahydrate (0.42 g; 1.0 mmol). The mixture was refluxed for 5 h at 180 °C, during which a lilac precipitate was



Scheme 2: Synthesis of neodymium(III) complex

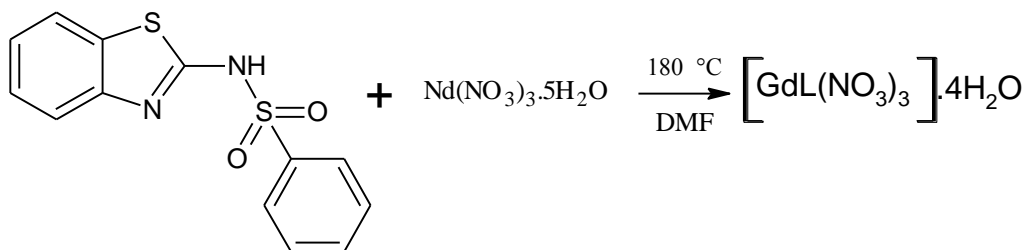
Syntheses of N-(benzothiazol-2-yl)benzenesulphonamide, [L]

The method of Obasiet *al* (2012) was employed in the synthesis of the ligand. To a solution of 2-aminobenzothiazole (3.00 g; 20 mmol) in acetone (12.50 mL) was added benzenesulphonylchloride (20 mL) with stirring. The mixture was refluxed for 1 h at 140 °C, during which, pinkish precipitate was formed. The precipitate was recrystallized in ethanol, dried in a stream of air and stored in a desiccator (Scheme 1). IR ($\nu \text{ cm}^{-1}$): 3406 (br), 2807 (w), 2722(w), 1579 (s), 1465 (m), 1162 (w), 897(m), 626 (s); ^1H NMR (δ/ppm): 7.4(5H,s), 7.8 (4H,m), 10.1(1H,t); ^{13}C NMR (δ/ppm): 168.8, 141.9, 139.6, 136.2, 129.0, 128.4, 127.6, 125.7, 124.6, 123.6, 114.4.

formed. Thereafter, it was filtered, dried in a stream of air and stored in desiccator (Scheme 2). mp: >360 °C, $\Omega(\mu\text{S}/\text{cm})$: 17.9; IR ($\nu \text{ cm}^{-1}$): 3407 (br), 3200 (br), 2920 (w), 2363 (w), 1585 (s), 1409(m), 1351 (m), 1126 (w), 777 (m), 618 (w), 408 (w). Anal. Calcd for $\text{C}_{13}\text{H}_{18}\text{S}_2\text{N}_5\text{O}_{15}$: C, 12.59; H, 1.18; N, 2.75; Anal: C, 12.85; H, 1.49; N, 1.77.

Synthesis of the gadolinium(III) complex, $[\text{GdL}(\text{NO}_3)_3] \cdot 4\text{H}_2\text{O}$

This was synthesized by the reaction of solution of the ligand, N-(benzothiazol-2-yl)benzenesulphonamide (0.58 g; 2.0 mmol) in DMF (10 mL) with aqueous solution of gadolinium(III) nitrate pentahydrate (0.43 g; 1.0 mmol). The mixture was refluxed for 6 h at 180 °C, during which a milky precipitate was



Scheme 3: Synthesis of gadolinium(III) complex

Antibacterial Activities

The antibacterial screening was carried out at the Department of Veterinary Pathology and Microbiology, University of Nigeria, Nsukka. The ligand and its metal complexes were screened *in vitro* for their antibacterial activities against gram-positive bacteria (*Staphylococcus aureus*) and gram-negative bacteria (*Pseudomonas aeruginosa*, *Proteus spp.*, *E. coli* strain 6 and *E. coli* strain 13) using the agar well diffusion method as described by Chahet *et al.*, (2006). The minimum inhibitory concentrations (MICs) of the test compounds were determined using the agar dilution method as described by Ojo *et al.*, (2007).

Results and Discussion

Equation of Reactions

Schemes 1-3 represent the equations of reactions for the synthesis of the ligand and its metal complexes.

formed. Thereafter, it was filtered, dried in a stream of air and stored in desiccator (Scheme 3). mp: >360 °C, Ω ($\mu\text{S}/\text{cm}$): 16.3; IR (ν cm^{-1}): 3421 (br), 3200 (br), 2925 (w), 2171 (w), 1581 (s), 1415 (m), 1351 (w), 1125 (w), 777 (m), 625 (w), 392 (w). Anal. Calcd for $\text{C}_{13}\text{H}_{18}\text{S}_2\text{N}_5\text{O}_{15}$: C, 12.72; H, 1.47; N, 2.28; Anal: C, 12.94; H, 1.37; N, 1.31.

Physical Properties and Molar Conductivity of the Compounds

The ligand is a pinkish crystalline substance with a melting point of 178 – 180 °C. The neodymium complex, is lilac in colour and crystalline in texture with a melting point >360 °C while the gadolinium complex is milky and crystalline with melting point >360 °C. The low conductance values of 17.9 and 16.3 $\mu\text{S}/\text{cm}$ indicate the non-electrolytic nature of the complexes in DMSO (Imran *et al.*, 2013; Mohanan *et al.*, 2009; Geary, 1971).

Mass Spectral Data of the Ligand

The mass spectra of the ligand (Fig. 1), agreed with the proposed structure. It showed molecular ion $[\text{C}_{13}\text{H}_9\text{S}_2\text{N}_2\text{O}_2]^+$ at $m/z = 289.01$ and important fragments at 156 $[\text{C}_6\text{H}_6\text{SNO}_2]^+$ and 148.95 $[\text{C}_7\text{H}_5\text{SN}_2]^+$.

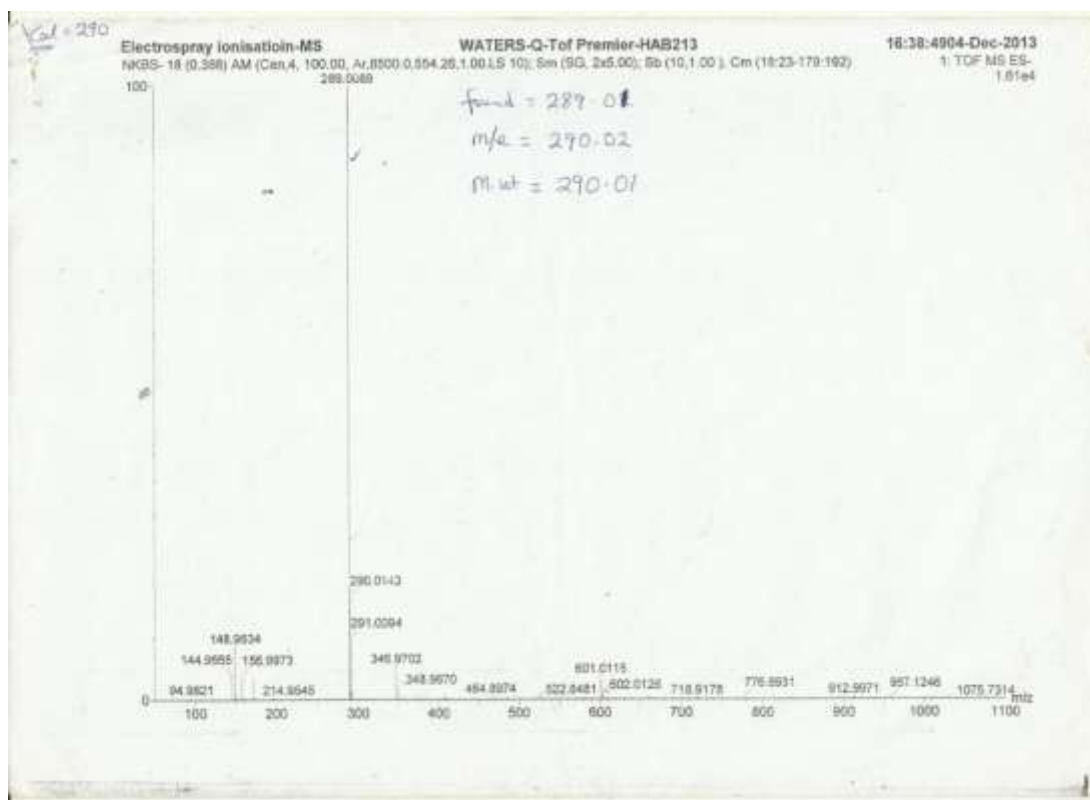


Fig. 1: Mass spectra of the ligand [L]

Elemental Microanalysis of the Compounds

For the complexes, the results of their elemental microanalysis (the percentage compositions of C, H and N) concur with the calculated values to a large extent. It showed that the complexes possess 1:1 metal ligand stoichiometry.

IR Spectra of the Compounds

The weak band (Figs. 2, 3 and 4) at; 3406 cm^{-1} , 3407 cm^{-1} and 3421 cm^{-1} for the ligand and its neodymium(III) and gadolinium(III) complexes respectively were assigned to N-H stretching vibrations. The marked difference observed in the frequency of the ligand compared with that of the gadolinium complex indicates coordination to the metal ion through the exocyclic nitrogen. Conversely, the insignificant difference of 1 cm^{-1} observed in the neodymium complex showed that the metal ion did not coordinate through the exocyclic nitrogen. In each of the complexes, the broad band observed at 3200 cm^{-1} was attributed to

OH vibrations of coordinated water. Two strong to medium peaks each between 1409-1585 cm^{-1} observed in the ligand and its metal complexes were assigned to C=N stretching vibrations. The difference in the frequencies of the ligand compared with that of the complexes show coordination of the ligand to the metal ion through the nitrogen atom of the thiazole ring. Also the peak at 1351 cm^{-1} in both complexes indicate coordination of nitrate ions. Peaks at 1162, 126 and 1125 for the ligand and its neodymium and gadolinium complexes respectively were assigned to SO_2 stretching vibration. The marked difference in the frequency of the ligand (>20 cm^{-1}) compared with that of the complexes still suggest coordination through the oxygen atom of the SO_2 group. Furthermore, the coordination of the ligand to the central metal ion through nitrogen and oxygen atoms, (M-N, M-O bonds) was confirmed by the peaks at 408 and 392 in the neodymium and gadolinium complexes respectively.

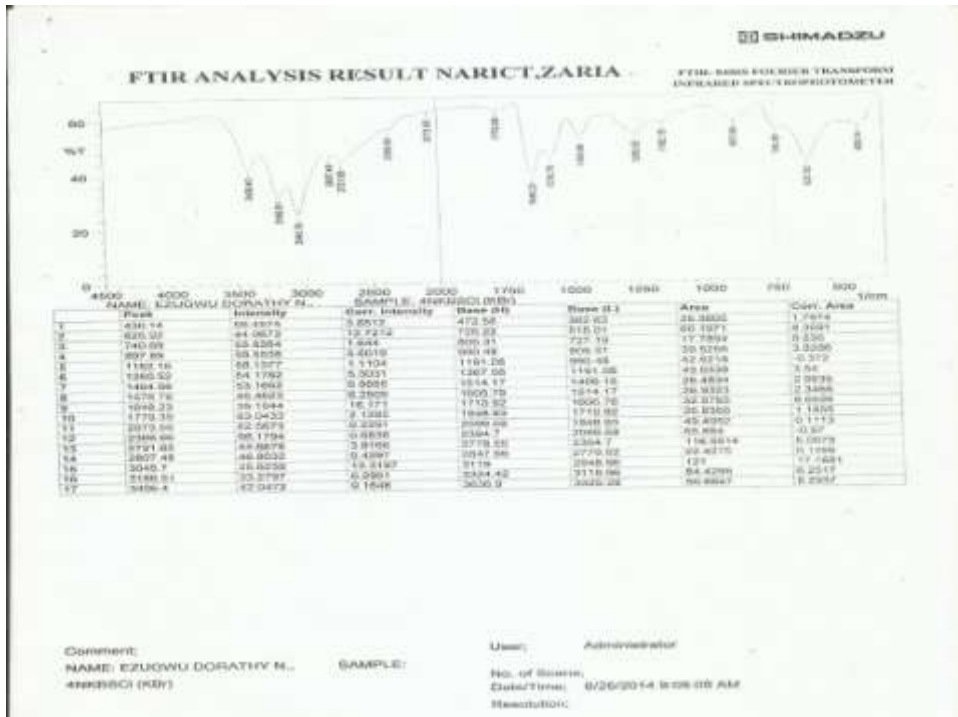


Fig. 2 :IR spectra of the ligand [L]

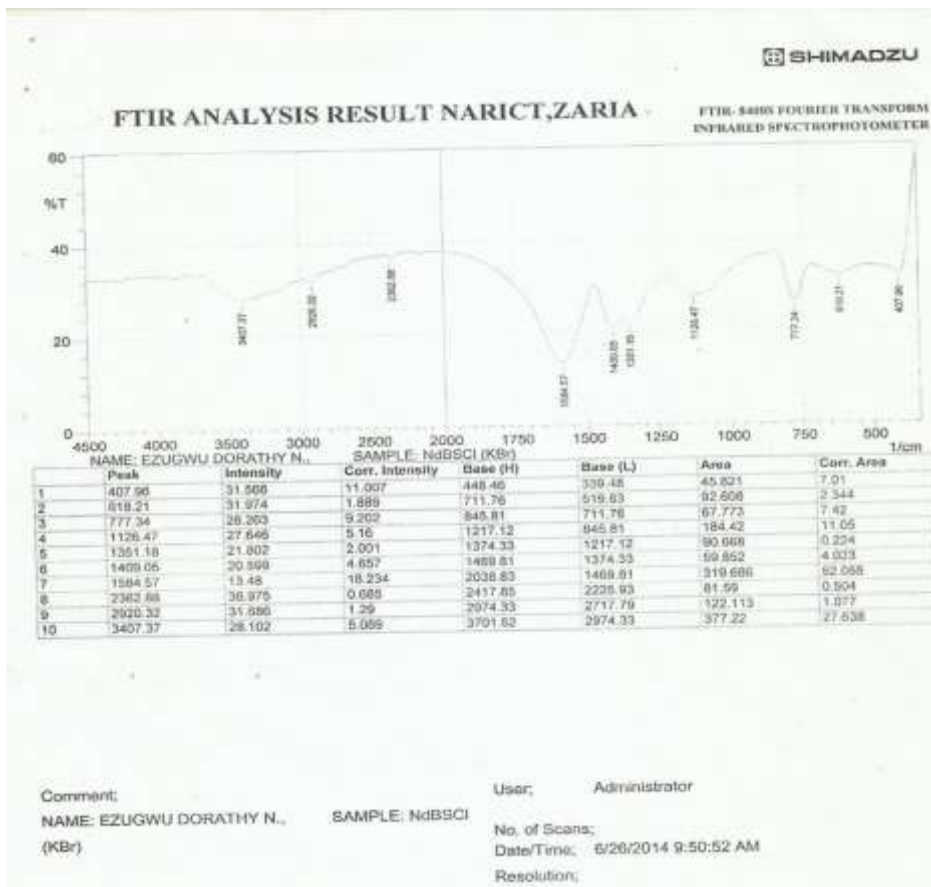


Fig. 3 :IR spectra of the Nd(III) complex, [Nd(NO₃)₃].H₂O

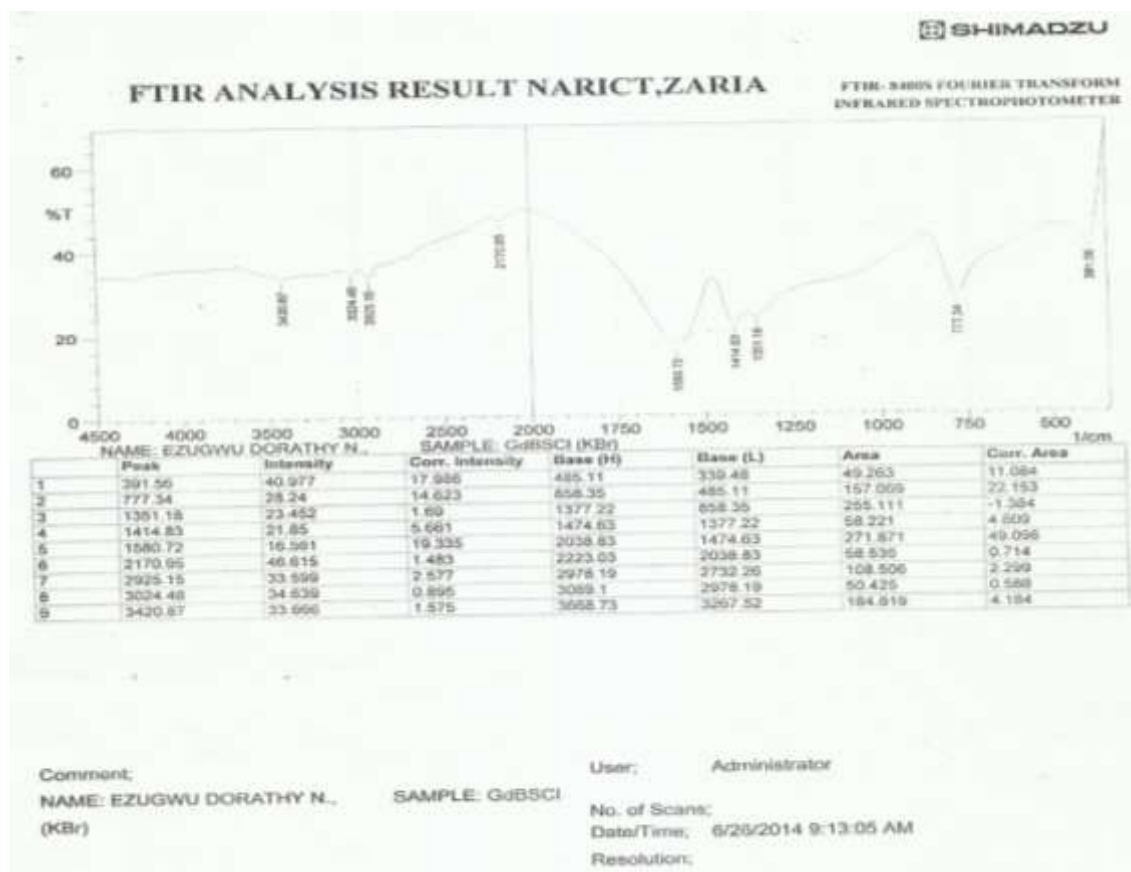


Fig. 4 :IR spectra of the Gd(III) complex, $[\text{Gd}(\text{NO}_3)_3] \cdot 4\text{H}_2\text{O}$

^1H and ^{13}C NMR Spectra of the compounds.

The ^1H NMR spectrum of the ligand (Fig. 5) showed characteristic singlet and multiplet signals appearing at 10.1 ppm (1H,s), 7.8 ppm (4H,m) and 7.4 ppm (5H,s). These were assigned to N-H protons, benzothiazole protons and phenyl protons respectively. Interestingly, this concurred with the anticipated results (Obasiet *al.*, 2012). However, The spectra of the complexes (Figs. 6 and 7), did not give realistic signals due to the

paramagnetic properties of Nd(III) and Gd(III) (Abid, 2013). The ^{13}C NMR spectrum of the ligand (Fig. 8) gave peaks at 168.8 ppm, 167.0 ppm, 141.9 ppm, 139.6 ppm, 136.2 ppm, 132.4 ppm and 129.0 ppm which were assigned to benzothiazole carbons, ($\text{C}_1\text{-C}_7$) respectively. Peaks at 128.4 ppm, 127.6 ppm, 125.7 ppm, 124.6 ppm, 123.6 ppm and 114.4 ppm were assigned to phenyl carbons, ($\text{C}_8\text{-C}_{13}$) respectively. Nevertheless, the ^{13}C NMR spectra of the complexes did not give meaningful results.

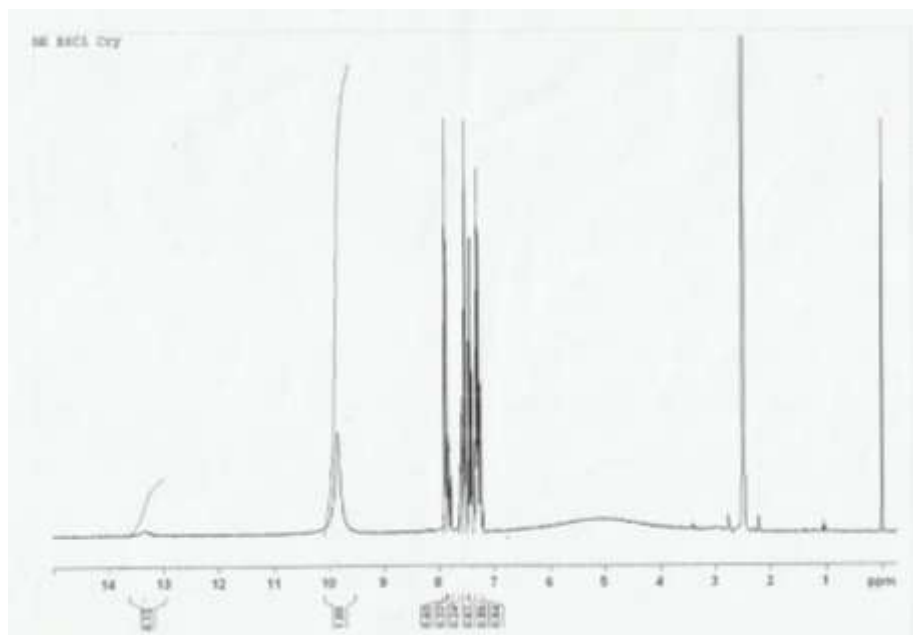


Fig. 5 : ^1H NMR spectra of the ligand, [L]

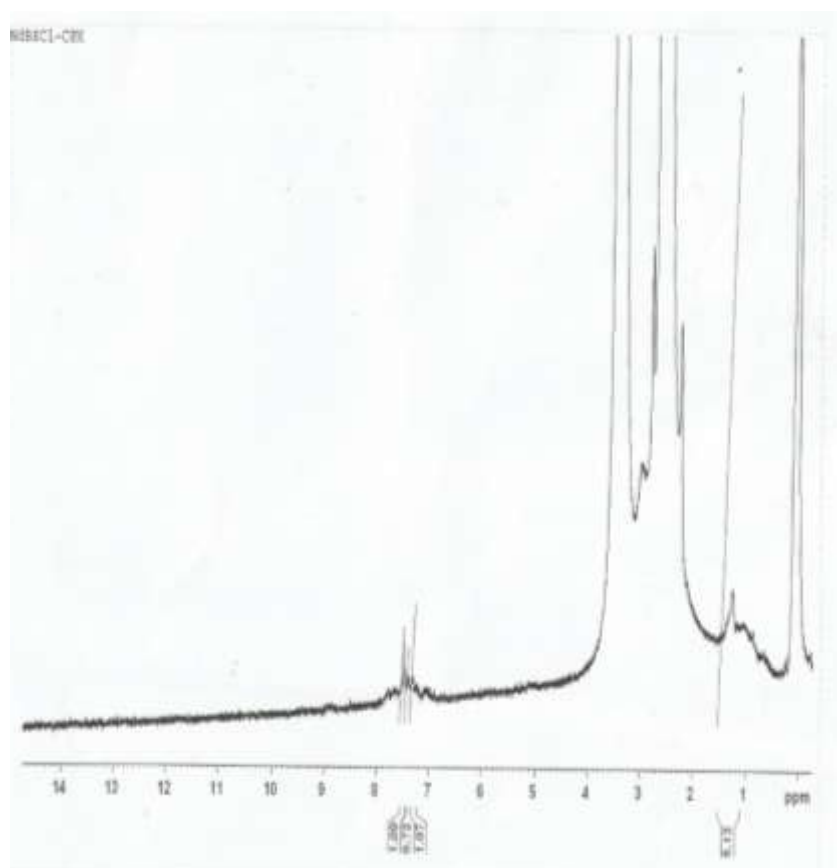


Fig. 6 : ^1H NMR spectra of Nd(III) complex, $[\text{NdL}(\text{NO}_3)_3] \cdot 4\text{H}_2\text{O}$

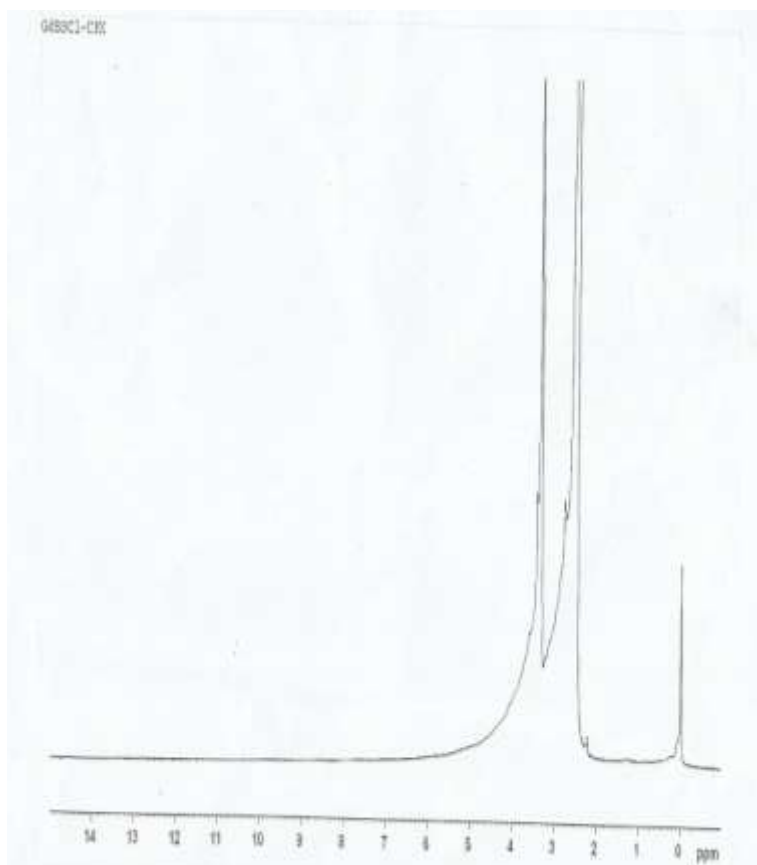


Fig.7 : ¹H NMR spectra of the Gd(III) complex, [GdL(NO₃)₃].4H₂O

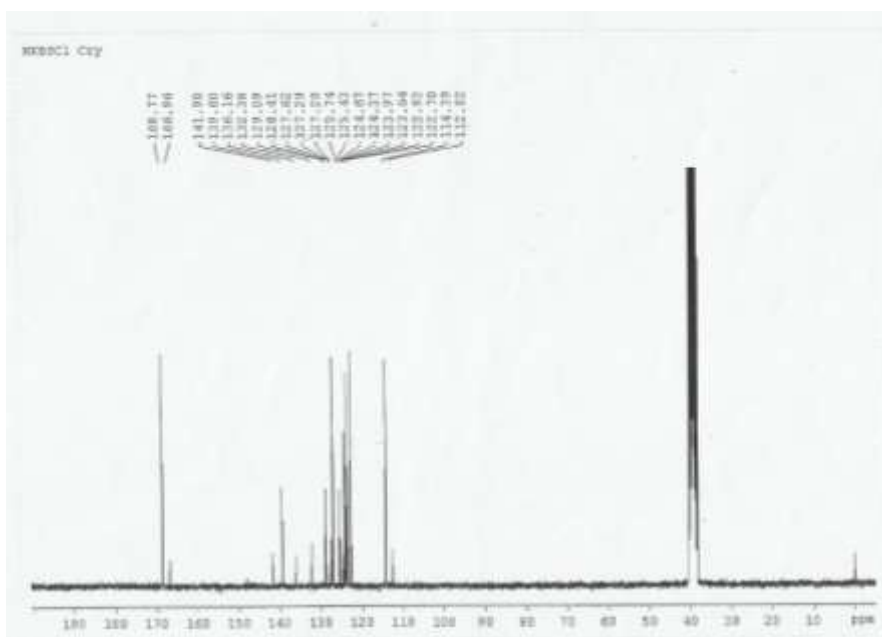


Fig. 8 : ¹³C NMR spectra of the ligand, [L]

Antibacterial Activities of the Compounds

Table 1 shows the inhibitory zone Diameter (IZD) in mm and minimum inhibitory concentration (MIC) in mg/mL. Based on the IZD values, the ligand and its neodymium complex were highly active against the tested gram-positive bacteria (*Staphylococcus aureus*). All the synthesized compounds showed varying activity against the tested gram-negative

bacteria (*E. coli* strain 6, *E. coli* strain 13, *Pseudomonas aeruginosa* and *Proteus spp.*). The neodymium complex was active against all the tested gram-positive and gram-negative bacteria. In most cases the MIC values were very much lower than the standard drugs (ciprofloxacin and gentamycin) used. This is a clear indication that the neodymium complex is more active against these microbes than the standard drugs.

Table 1: Antibacterial Activities of the ligand and its metal complexes

Samples	<i>E. coli</i> strain 6		<i>E. coli</i> strain 13		<i>S. aureus</i>		<i>P. aeruginosa</i>		<i>Proteus spp.</i>	
	IZD (mm)	MIC (mg/mL)	IZD (mm)	MIC (mg/mL)	IZD (mm)	MIC (mg/mL)	IZD (mm)	MIC (mg/mL)	IZD (mm)	MIC (mg/mL)
[L]	16	1.45	16	1.35	14	2.19	-	-	15	1.32
[NdL(NO ₃) ₃ (H ₂ O) ₄]	15	1.78	14	2.19	17	1.45	12	5.01	16	1.26
[GdL(NO ₃) ₃ (H ₂ O) ₄]	11	5.50	-	-	-	-	-	-	10	5.00
Ciprofloxacin	-	20.00	-	20.00	-	0.63	-	10.00	-	0.16
Gentamycin	-	100.00	-	100.00	-	2.50	-	20.00	-	5.00

Conclusions

Neodymium(III) and gadolinium(III) complexes of N-(benzothiazol-2-yl)benzenesulphonamide were synthesized. The compounds were characterized using various physical and spectral studies. The *in vitro* antibacterial screening of the complexes were carried out on both gram-positive bacterial strain (*Staphylococcus aureus*) and gram-negative bacterial strains (*Pseudomonas aeruginosa*, *Proteus spp.*, *E. coli* strain 6 and *E. coli* strain 13) using agar-well diffusion method. Results obtained revealed that the compounds showed varying activities against the tested bacteria. The antibacterial activity was

enhanced in the neodymium(III) complex. This shows that Nd(III) metal has synergetic effect on the antibacterial activity of the ligand. Therefore, antibacterial activity of coordinated compounds depends on the type of metal ion. However, some remarkable enhancement in the antibacterial activity of organic compounds upon coordination can be attributed to high toxicity of metal ion in normal cell process.

Acknowledgements

With deep sense of gratitude we wish to appreciate University of Nigeria Nsukka for providing research facilities. We are also grateful to University of Mauritius where some of the analyses were done.

References

- Aime, S.Crich, S.G. Gianolio, E. Giovenzana, G.B. Tei, L. and Terreno, E. (2006). High sensitivity lanthanide(III) based probes for MR-medical imaging. *Coordination Chemistry Rev. (250)*, 1562–1579.
- Aneta, K. Iwona, F. Justyna, L. and Danuta, B. (2014). Biological Activity and Synthesis of Sulphonamide Derivatives. *Chemik. (68)*, 620-628.
- Chah, K.F. Eze, C.A. Emuelosi, C.E. and Esimone, C.O. (2006). Antibacterial and Wound Healing properties of Methanolic Extracts of some Nigerian Medicinal plants, *J.Ethnopharmacology. (104)*, 164 – 167.
- Claudiu, T. Supuran, F. B. Silvia, T. W. Richard, C. and Andrea, S. (2001). Carbonic Anhydrase Inhibitors; Sulfonamides as Antitumor Agents. *J.Bioorg.and Med. Chem. (9)*, 703-714.
- Davenport, D. (2012). The War Against Bacteria. *PubMed, (1)*, 55-58.
- Franklin, S.J. (2001). Lanthanide-mediated DNA hydrolysis. *Current Opinion in Chemical Biology, (2)*, 201–208.
- Geary W.J. (1971). The use of conductivity measurements in organic solvent for characterization of coordination compounds. *CoordChemRev(7)*, 532.
- Gootz,(1990). Discovery and Development of New Antimicrobial Agents. *ClinMicrobial.Rev.(1)*, 13-31.
- Imran, A. Waseem, A. Wani and Kishwar, S. (2013). Empirical Formular to Molecular Structures of Metal Complexes by Molar Conductance. *Synthesis and Reactivity in inorganic and Nano –Metal Chemistry. (43)*, 1162 – 1170.
- Jesman, C. Mludzik, A. and Cybulska, M. (2011). History of Antibiotics and Sulphonamide = Discoveries. *J. National Center for Biotech Infom.(179)*, 320-322.
- Korsinczky, M. Fischer, K. Chen, N. Baker, J. Rieckmann, K. and Cheng, Q. (2004). Antimicrobial Agents and Chemotherapy. *J.Antimicrobial Chemotherapy (48)*, 2214-2222.
- Lacey, R.W. (1979). Mechanism of Action of Trimethoprim and Sulphonamides; Relevance to Synergy in vivo. *J. Antimicrobial Chemotherapy. (5)*, 75-83.
- Mohanan K, Athira CJ, Sindhu Y, Sujamol MS (2009). Synthesis, spectroscopic, characterization and thermal studies of some lanthanide(III) nitrates complexes with hydrazoderivatives of 4-aminoantipyrine. *J. Rare Earths (27)*. 705.
- Obasi, L.N. Okoye, C.O.B. Ukoha, P.O. and Chah, K.F. (2013). Syntheses, Characterization and Antimicrobial Screening of N-(benzothiazol-2-yl)-2,5-dichlorobenenesulphonamide and its Cu (I), N, (II), Mn(II), Co (II) and Zn (II) Complexes, *Asian J. of Chem. (25)*, 2199-2207.
- Obasi, L.N. Okoye C. O. Benedict, P. O. Ukoha, and A. O. Anaga; (2012). Syntheses, Characterization, and Antimicrobial Screening of N-(benzothiazol-2-yl)benzenesulphonamide and its Cu(I), Ni(II), Mn(II), Co(II), and

- Zn(II) Complexes. *E-Journal of Chemistry*, 9(4), 2354-2370.
- Ojo, O.O. Ajayi, A.O. and Anibjuwon, I.I. (2007). Antibacterial potency of Extract of lower plants. *Journal of Zhejiang University Sciences*. (8), 189- 191.
- Paige, J.C. and Tollenfson, L. (2003). *Veterinary Product; Residues and Resistant Pathogens in Food Safety; Contaminants and Toxins*, 3rd Edition, CABI Publishing Walling Food, UK (13), 290-306.
- Picard, C. Geum, N. and Nasso, I. (2006). A Dual Lanthanide Probe Suitable for Optical (Tb³⁺ luminescence) and Magnetic Resonance Imaging. *Bioorganic & Medicinal Chemistry Letters*, (20), 5309–5312.
- Raafat, M.I. Abdalla, M.K. Helen, R. (2008). ¹H NMR , IR and UV-Vis Spectroscopic Studies of some Schiff Bases Derived from 2-aminobenzothiazole and 2-amino-3-hydroxypyridine. *J.Chin. Chem.Soc.* (55), 875.
- Rosaleen, J.A. Paul, W.G. Adam, T and Alan, J.W. (2012). *Antibacterial Agents; Chemistry, Mode of Action, Mechanisms of Resistance and Clinical Applications*, 1st Edition, John Wiley and Sons Ltd, Chichester, 105-124.
- Sharma, R.C. Thripathi, S.P. Kanna, K.S. and Sharma, R.S. (1981). Biologically active mixed-ligand complexes of rare earths. *Current Science*, (17), 748–750.
- Sindhu, Y. Athira, C.J. Sujamol, M.S. Joseyphus, R.S, Mohanan, K. (2013). Synthesis, Characterization, DNA Cleavage, and Antimicrobial Studies of some Transition Metal Complexes with a Novel Schiff Base Derived from 2-aminopyrimidine. *J.Syn. React.Inorg.Met-Org. Nano-Met.Chem.*, (43), 226.
- Williamson, K. L. Minard, R. D. and Masters, K. M. (2007). *Macroscopic and Microscale Organic Experiments*, 5th Edition, Houghton Mifflin, Boston, 617.

Preliminary interpretation of aeromagnetic anomalies around Nsukka and Udi areas of southeastern Nigeria

Gladys Ujunwa Edeh, Johnson Cletus Ibuot, John Akor Yakubu and Daniel Nnaemeka Obiora*

Department of Physics and Astronomy, University of Nigeria, Nsukka, Enugu State, Nigeria.

*Corresponding author email address: daniel.obiora@unn.edu.ng

Abstract

Aeromagnetic data of Nsukka and Udi areas were analyzed qualitatively and quantitatively. The study was aimed at determining the depth to magnetic sources using Source Parameter Imaging (SPI) technique. Regional-residual separation was applied to total aeromagnetic intensity contour map to produce a residual aeromagnetic intensity contour map. The total magnetic intensity (TMI) varies from -110 nT to 140 nT, while the residual intensity varies from -150 nT to 120 nT. The area is marked by the high and low magnetic signatures. The upward continuation map varies from -35 to 80 nT, while the reduction to pole (RTP) varies from -1200 to 1100 nT. The SPI estimated depth ranges from 472.3 m to 6051.8 m. The sedimentary thickness in the area is considered high and therefore may favour hydrocarbon generation and accumulation.

Keyword: Aeromagnetic data, magnetic sources, source parameter imaging, regional-residual separation, Nsukka and Udi areas

Introduction

Aeromagnetic surveys are widely used to aid in the production of geophysical maps and are also commonly used during mineral exploration. It is a powerful tool for delineating the regional geology (lithology and structure) and a detailed aeromagnetic map is proven to be very effective in cases where the geology of the study area is clearly known (Hassanein and Soliman, 2008). The purpose of magnetic surveying is to identify and describe regions of the Earth's crust that have anomalous magnetizations. In the realm of applied geophysics, these anomalous magnetizations might be associated with local mineralization that is potentially of commercial interest, or they could be due to subsurface structures that have bearing on the location of oil deposits.

The aeromagnetic geophysical method plays a distinguished role when compared with other geophysical methods in its rapid rate of coverage and low cost per unit area

explored. Onuba et al. (2011) pointed out that the main purpose of magnetic survey is to detect rocks or minerals possessing unusual magnetic properties that reveal themselves by causing disturbances or anomalies in the intensity of the earth magnetic field. The aeromagnetic survey is applied in mapping these anomalies in the earth's magnetic field and this is correlated with the underground geophysical structure. Faults usually show up by abrupt changes or close spacing in orientation of the contours as revealed by the magnetic anomalies. For minerals and intrusive igneous rocks, residual magnetic anomaly maps are useful since they identify the presence of intrusives, lava flows, or igneous plugs.

Anambra Basin is one of the Basins suspected to have high hydrocarbon potential, besides other economic mineral deposits concentration (Obiora et al. 2015; Obiora et al., 2016). Generally, the Benue Trough is believed to have been formed when South America separated from Africa (Petters, 1978). The major

component units of the Lower Benue Trough include the Anambra Basin, the Abakaliki Anticlinorium and the Afikpo Syncline. There are some published works on the depths to basements/magnetic source bodies over the lower Benue Trough and Anambra Basin, but only one was found on Nsukka area (Obiora et al., 2015) and none was found on Nsukka and Udi areas combined. Hence, the main purpose of this work is to determine the depth of the magnetic anomalous bodies within Nsukka and Udi areas using source parameter imaging technique.

Geology of the study area

Figure 1 shows the geologic map of the area. The study area lies between Latitude 6°00' N – 7°00'N and Longitude 7°00'E – 7°30'E in the southeastern Nigeria and northern part of Enugu state. The study area (Nsukka and Udi areas) is within the Abakaliki Basin, the Anambra Basin and the Niger Delta. They are underlain by rocks of Coniacian-Paleocene series.

Sedimentary rocks of the study areas commenced with the Agwu Formation (Abakaliki Basin), followed by sedimentary successions of the Anambra Basin which consist of two major groups namely Nkporo Group (Campano-Maastrichtian Owelli, Nkporo and Enugu formations), and the Coal Measure (which comprises of the Mamu, Ajali and Nsukka formations). Palaeocene transgression commenced with the deposition of Imo Formation at the onset of the Niger Delta (Nwajide and Reijers, 1995; Onwuemesi, 1995; Nwajide, 2013). Sediments deposited within Coniacian-Paleocene time interval occur in four distinct physiographic provinces, namely: the Cross River plains, the Escarpment, the Plateau and the Anambra plains. It was discovered that over 3,965 m of sediments comprising shales, sandstones, limestone and coal were deposited in the area. Their environment of deposition varied from marine, through brackish water to entirely continental.

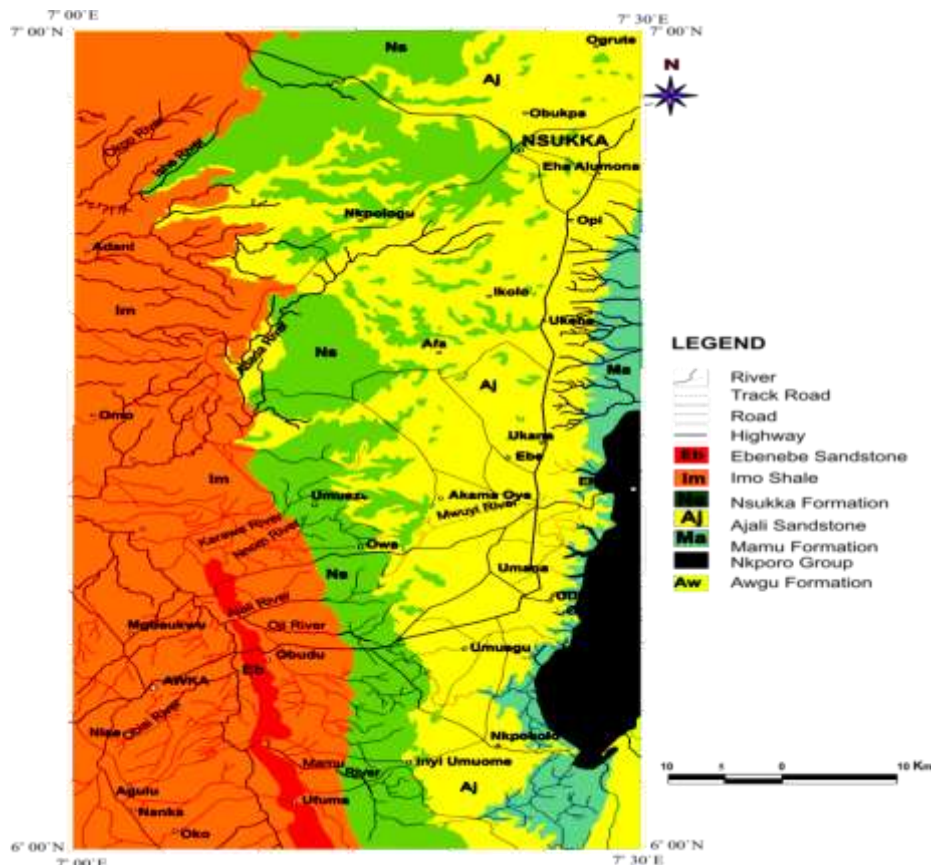


Figure 1. Geologic map of Nsukka and Udi areas

Source of data

Aeromagnetic data of Nsukka (sheet 287) and Udi (sheet 301) areas were gotten from the Nigerian Geological Survey Agency (NGSA). The data, covering sixty minutes (One degree) by thirty minutes (Half-degree) sheet at a scale of 1:100,000 were acquired at a flight altitude of 80 m, along NE-SW flight lines that were spaced at 500 m. It was recorded in digitized form (X, Y, Z text file) after removing the geomagnetic gradient from the raw data using International Geomagnetic Reference Field (IGRF), 2009, with intensity of 33095 nT (nanoTesla). The angles of inclination and declination were -13.279° and -1.449° respectively. The X and Y represent the longitude and latitude of Nsukka and Udi areas in meters respectively, while the Z represents the magnetic field intensity measured in nanoTesla.

Method and data analysis

The two sheets (287 and 301) were merged and Total Magnetic Intensity (TMI) grid of the study area was produced into map using Oasis Montaj software. Gridding, Polynomial fitting (Regional and residual separation), and enhancement processes such as reduction to pole, derivatives and Upward and downward continuation were applied to the TMI grid using WingLink software. The general purpose of enhancement processes is to enhance anomalies of interest and to gain some basic information on source location or magnetization. The upward continuation operation smoothen the anomalies obtained at the ground surface by projecting the surface mathematically upward above the original datum (Revees, 2005). Noise (random noise) was removed by upward continuation of the aeromagnetic anomaly field to a height of 125 m before producing the upward continued aeromagnetic anomaly map of the sheet in colour. By implementation of reduction to pole on both the amplitude and phase spectra of the original TMI grid,

the shapes of the magnetic anomalies were simplified so that they appeared like the positive anomalies located directly above the source expected for induce magnetized bodies at the magnetic pole where the angle of inclination is 90° and zero declination. Derivatives helped to sharpen the edges of anomaly and enhanced shallow features (Revees, 2005). This includes first and second vertical derivatives, and horizontal derivative.

The source parameter imaging (SPI) is a technique that uses an extension of the complex analytical signal to estimate magnetic depths. The estimate of the depth is independent of the magnetic inclination, declination, dip, strike and remnant magnetization. The Source Parameter Imaging (SPI) function is a quick, easy, and powerful method for calculating the depth of magnetic sources. Source parameter imaging (SPI) was used to evaluate the depths of magnetic source bodies. SPI method calculated source parameters for gridded magnetic data. The Source Parameter Imaging (SPI) technique is represented mathematically (Thurston and Smith, 1997) as:

$$Depth = \frac{1}{K_{max}} = \frac{1}{(\sqrt{(\partial Tilt / \partial x)^2 + (\partial Tilt / \partial y)^2})_{max}}$$

where Tilt is given as:

$$Tilt = \arctan\left(\frac{\partial T / \partial z}{\sqrt{(\partial T / \partial x)^2 + (\partial T / \partial y)^2}}\right) = \arctan\left(\frac{\partial T / \partial z}{HGRAD}\right), \quad 2$$

where HGRAD is horizontal gradient, T is total magnetic intensity (TMI), K is the wave number, $\partial T / \partial x$, $\partial T / \partial y$, $\partial T / \partial z$ are derivatives of T with respect to x, y and z. The method assumes either a 2D sloping contact or a 2D dipping thin-sheet model and is based on the complex analytical signal. The SPI depth of magnetic data was determined using Oasis Montaj software and employing the first vertical derivatives and horizontal gradient. SPI method made the task of interpreting magnetic data significantly easier.

Results and discussion of results

The total magnetic intensity (TMI) map of the study area (Fig. 2) varies from -110 nT to 140 nT. The area is marked by the high (red colour) and low (green, blue and purple colours) magnetic signatures. In

TMI curve (Fig. 2), we can observe obvious contour truncation, linear alignment of circular bodies and colour matching, which gives room for the presence of faults.

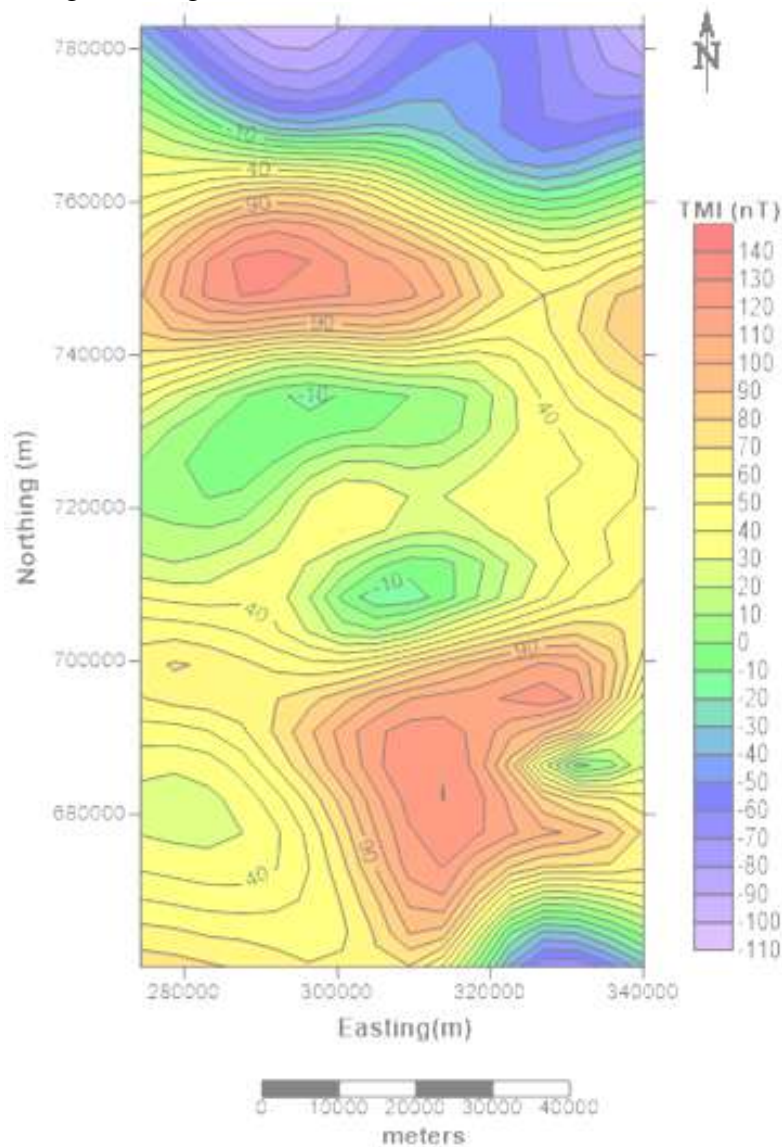


Figure 2. TMI map of the Study Area

Figure 3 depicts the Upward Continuation map of the study area. The upward continuation operation smoothen the anomalies obtained at the ground surface by projecting the surface mathematically

upward above the original datum (Reeves, 2005). In projecting downward, the regional effects are suppressed while the residual effects are enhanced.

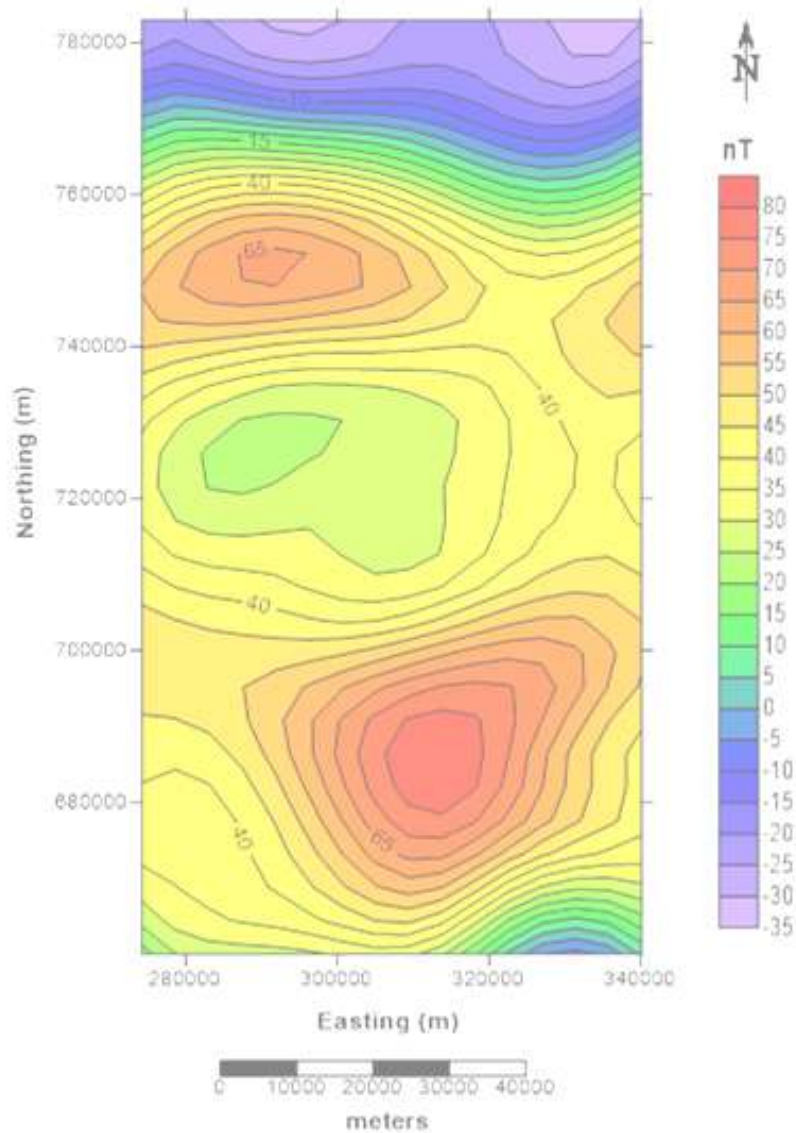


Figure 3. Upward Continuation Map

Reduction to pole was performed on the digitized aeromagnetic data of the study area and this is shown in figure 4. This method has simplified the interpretation because for sub-vertical prisms or sub-vertical contacts (including faults), it transforms their asymmetric responses to simpler symmetric and anti-symmetric forms. The symmetric “highs” are directly centered on the body, while the maximum

gradient of the anti-symmetric dipolar anomalies coincides exactly with the body edges. The regional field was removed from the total magnetic intensity map to obtain the residual map with a first order polynomial fitting using WinGlink Software. Figure 5 shows the residual map of the area. The residual map varies from -150 nT to 120 nT.

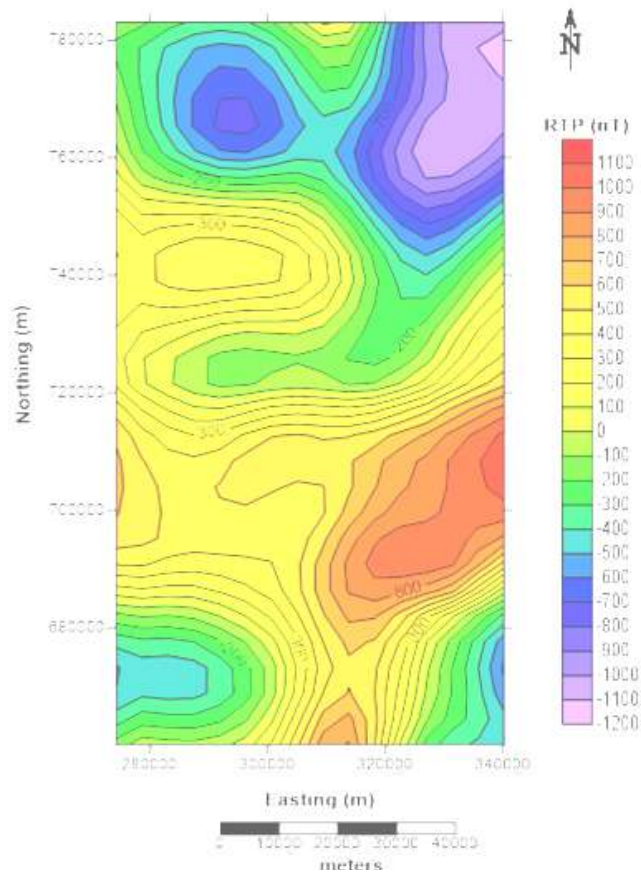


Figure 4. Map Showing the Reduction to Pole

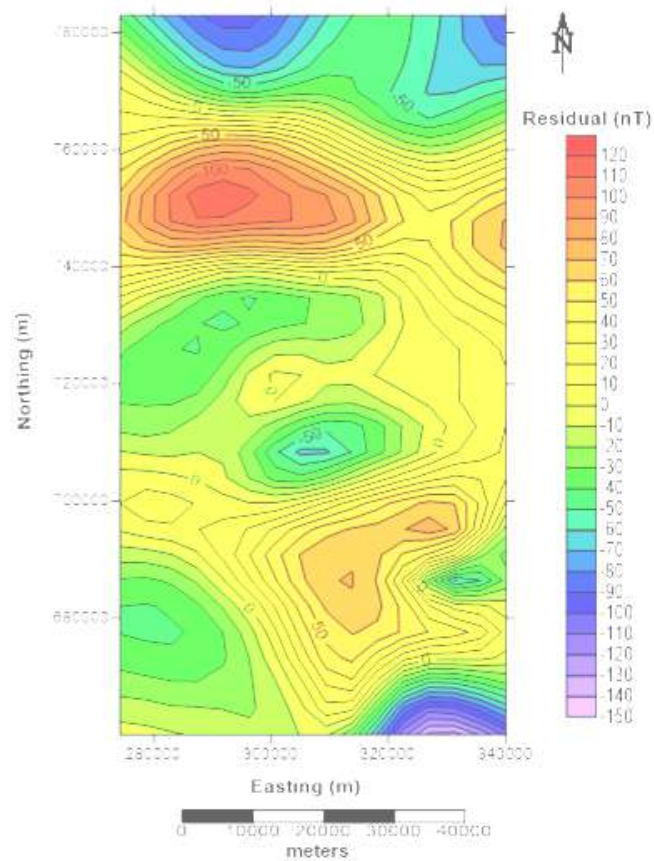
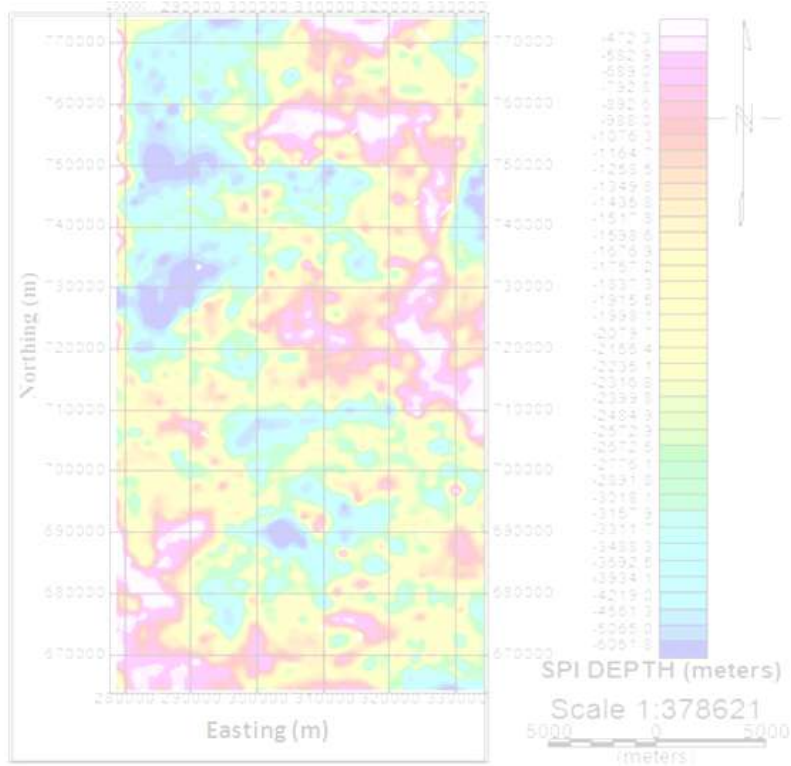


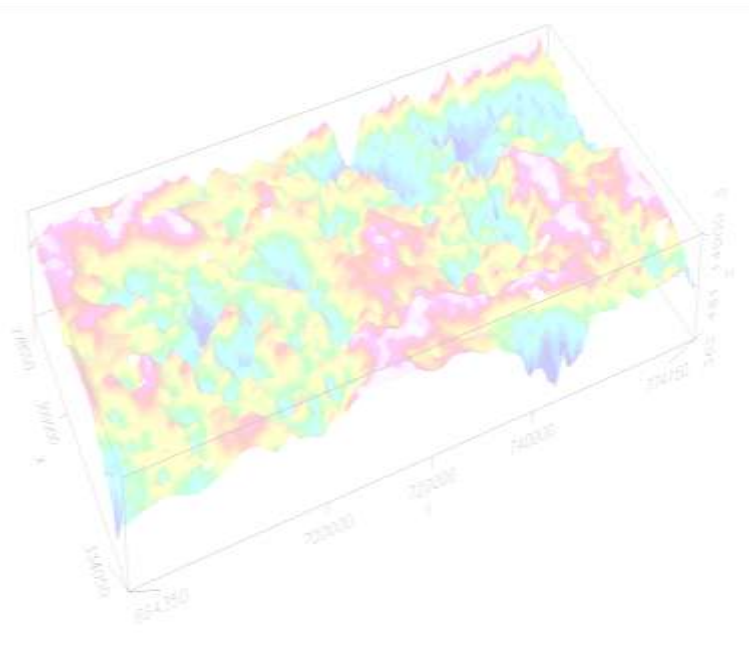
Figure 5. Residual Map of the Study Area

The SPI grid image and legend colours are shown in figure 6. The negative values on the legend depict the depths of buried magnetic bodies, which maybe deep seated basement rocks or near surface intrusive. The light purple colour generally indicates the areas occupied by shallow magnetic bodies while the deep blue colour depicts

areas of deep lying magnetic bodies. The SPI depths range from -472.3 m (Shallow magnetic bodies) to -6051.8 m (deep lying magnetic bodies). Figure 6a is the 2-D (2-dimensional) SPI grid map, while figure 6b shows the 3-D (3-dimensional) SPI grid map of the study area.



(a)



(b)

Figure 6: SPI Grid Map (a) 2D and (b) 3D of the Study Area

From the TMI curve (Fig. 2), it is seen that TMI anomaly values vary from -110 nT to 140 nT, while the residual values vary from -150 nT to 120 nT (Fig. 5). The colour legend bar helps to reveal areas of low and high TMI values which may be attributed to variations in depth, differences in magnetic susceptibility, and differences in lithology or degree of strike. The map highlights the high amplitude anomalies which can be seen in the southeastern and northwestern parts of the study area. Low amplitude anomalies are found in the northcentral part of the study area. The TMI contour map drawn at intervals of 10 nT also reveals the trends of the magnetic signatures within the area. It shows that circular contours are associated with spherical anomalies within some low TMI regions of the study area and long narrow patterns which are associated with dyke-like anomalies within the northern region of the study area. The depths obtained from SPI (Fig. 6) ranges from 472.3 m to 6051.8 m. The depth obtained from this study exceeds the depth (151.6 m- 3082.7 m) obtained by Obiora et al. (2015) who worked on Nsukka area alone. The depth results obtained in this work is in close agreement with the results obtained by Onwuemesi (1997) who worked on the Anambra Basin. He employed spectral analysis in his aeromagnetic data analysis on Anambra Basin and obtained a depth range between 0.9 and 5.6 km which is in close agreement with the depth value obtained in this work using SPI technique. The maximum depth (6051.8 m) obtained from the method employed in this work shows sufficient thick sediments favourable for accumulation of hydrocarbon which agrees with the work of Wright et al. (1985) which states that the minimum thickness of the sediment required for the commencement of oil formation from marine organic remains would be 2.3 km if other conditions are favourable.

Conclusion

Determination of depth to magnetic sources in Nsukka and Udi areas was carried out through the interpretation of aeromagnetic data by employing source parameter imaging (SPI) technique. The total magnetic intensity and the residual magnetic intensity maps showed that the area is marked by high and low magnetic signatures. The depth results obtained from SPI ranges from 472.3 m to 6051.8 m. The maximum depth obtained is sufficient enough for hydrocarbon generation and accumulation, if other factors are favourable.

Acknowledgement

The authors are grateful to Dr. IfeanyiOha of Geology Department, University of Nigeria, Nsukka, for his useful advice and Nigerian Geological Survey Agency for the aeromagnetic data.

References

- Hassanien, H.I.E. &Soliman, K.S. (2008). Aeromagnetic Data Interpretation of WadiHawashiya Area for Identifying Surface Structures, North Eastern Desert, Egypt. *Earth Science*, 20(1), 117–139
- Nwajide, C.S. (2013). Geology of Nigerian Sedimentary Basins. CSS Bookshops Ltd.
- Nwajide, C.S. &Reijers, T.J.A. (1995). Sedimentology and sequence stratigraphy of selected outcrops in the upper cretaceous of lower Tertiary of the Anambra Basin. SPDC Exploration Report, XPMW 96007, 21–37
- Obiora, D.N., Ossai, M.N. &Okwoli, E. (2015). A case study of aeromagnetic data interpretation of Nsukka area, Enugu State, Nigeria, for hydrocarbon exploration. *International Journal of Physical Sciences*, 10(17), 503–519
- Obiora, D.N., Ossai, M.N., Okeke, F.N. &Oha, A.I. (2016). Interpretation of airborne geophysical data of Nsukka area, southeastern Nigeria. *Journal of the*

Geological Society of India, 88, 654-667

Onuba, L.N., Audu, G.K., Chiaghanam, O.I. & Anakwuba, E.K. (2011). Evaluation of aeromagnetic anomalies over Okigwe area, Southern Nigeria. *Res. J. Environ. Earth Sci.*, 3(5), 498–507

Onwuemesi, A.G. (1997). One dimensional spectral analysis of aeromagnetic anomalies and curie depth isotherm in Anambra Basin of Nigeria. *J. Geodynamics*, 23(2), 95-107

Onwuemesi, A.G. (1995). Interpretation of magnetic anomalies from the Anambra Basin of southeastern Nigeria. (Unpublished PhD thesis). Nnamdi Azikiwe University, Awka, Nigeria.

Petters, S.W. (1978). Stratigraphic Evolution of the Benue Trough and its implications for the Upper Cretaceous Paleogeography of West Africa. *J. Geol.*, 86(3), 11-322

Reeves, C. (2005). *Aeromagnetic Surveys; Principles, Practice and Interpretation*. GEOSOFT

Thurston, J.B. & Smith, R.S. (1997) Automatic conversion of magnetic data to depth, dip and susceptibility contrast using the SPI method. *Geophysics*, 62, 807-813

Wright, J.B., Hastings, D., Jones, W.B. & Williams, H.R. (1985). *Geology and Mineral resources of West Africa*. London: George Allen and Urwin

AN INTEGRATED APPROACH TO PETROLEUM EXPLORATION IN THE EASTERN COASTAL SWAMP DEPOBELT OF THE NIGER DELTA BASIN, NIGERIA.

*Chidozie Izuchukwu Princeton DIM., K. Mosto ONUOHA and Chukwudike Gabriel OKEUGO
Department of Geology, Faculty of Physical Sciences, University of Nigeria, Nsukka. Enugu State, Nigeria.

*Corresponding Author (Email: princeton.dim@unn.edu.ng)

Abstract: *Sequence stratigraphic, structural and reservoir analytical tools have been employed in interpreting the geology of the eastern Coastal Swamp Depobelt of the Niger Delta Basin. The aim was to understand the stratigraphic framework, structural styles and hydrocarbon reservoir distribution for improved regional hydrocarbon exploration across the onshore Niger Delta Basin. This study made use of well logs, biostratigraphic and petrophysical data, integrated with 3D regionalseismic volume spanning across several fields. Results reveal the occurrence of nine key chronostratigraphic surfaces (five maximum flooding surfaces and four sequence boundaries) that were tied to well-established bio-zones for high resolution sequence stratigraphic interpretation. The sediment stacking patterns recognized from gamma ray log signatures were used in delineating the lowstand system tract (LST), transgressive system tract (TST) and highstand system tract (HST) genetic units. Well log sequence stratigraphic correlation reveals that stratal packages were segmented into three depositional sequences occurring from middle to late Miocene age. In addition, strata packages thicken from north to south (basinwards), due possibly to the influence of syn-depositional structures on stratigraphy. The combination of reservoir sands of LST and HST, source and seal shales of TST and HST, and structural traps allow for good hydrocarbon accumulation. Reservoir evaluation studies using petrophysical parameters indicate the presence of good quality reservoir intervals, which are laterally continuous across several fields and partly compartmentalized within individual fields. Structural top maps of reservoirs show good amplitude response that are structurally controlled. The presence of key structural styles offer good hydrocarbon entrapment mechanism. Overall, the study has unraveled the existence of undrilled hydrocarbon leads at deeper depths that should be further revalidated for development.*

Keywords: Sequence stratigraphic framework, Structural configuration, Reservoir distribution, Coastal Swamp Depobelt.

Introduction

A lot of the earlier hydrocarbon prospectivity studies carried out over the years in the onshore Niger Delta Basin, were focused mainly on individual fields or leases except where adjacent fields or leases belonged to the same operator or company (Balogun, 2003; Magbagbeola, and Willis, 2007; Ehinola *et al.*, 2010). Those earlier studies were unable to provide information on stratigraphic intervals, structural features, and reservoir zones on a regional basis. This research work was aimed at utilizing a recently merged and reprocessed

regional 3D (Pre-Stack Depth Migrated - PreSDM) seismic volume and data from several wells in furthering our understanding of the stratigraphic framework, structural styles and reservoir distribution using integrated exploration techniques. The target was to identify stratigraphic intervals and delineate potential reservoirs and better define hydrocarbon leads and prospects within the paralic sequence of the Niger Delta Basin. The study area lies on the eastern part of the Coastal Swamp Depo-belt of the Niger Delta Basin of Nigeria (Fig. 1).

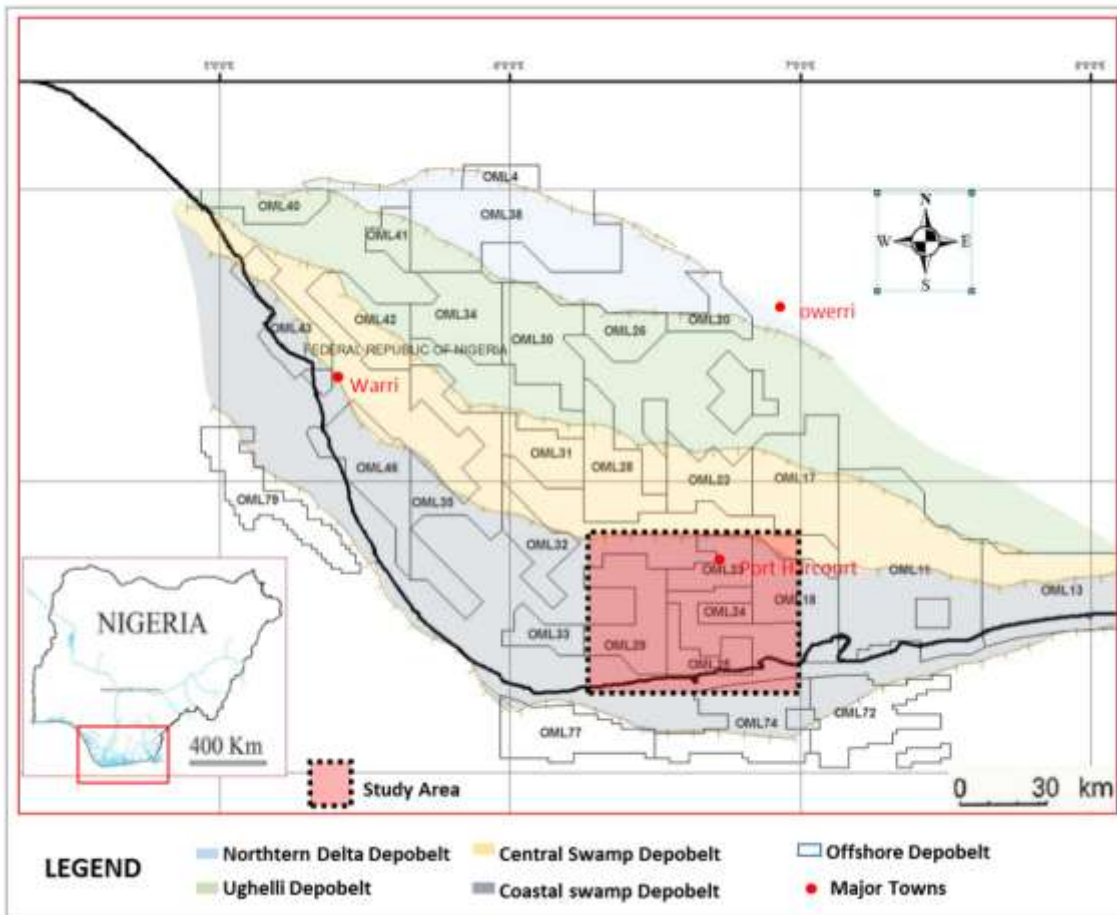


Fig. 1: Depobelt map with the oil and gas, onshore and offshore Niger Delta Basin showing the study area which lies on the eastern part of the Coastal Swamp Depobelt.

Geologic Framework

The evolution of the Niger delta was controlled by pre- and synsedimentary tectonics as described by Evamy et al. (1978), Ejedawe (1981) and Stacher (1995). The Niger Delta Basin is located in the Gulf of Guinea on the western coast of Africa (Fig. 1). The tectonic evolution and structural features in the Niger Delta basin has been widely documented in several works (Evamy et al., 1978; Lawrence et al., 2002). The stratigraphic succession comprises an upward-coarsening regressive association of Tertiary clastics up to 12 km thick (Weber and Daukoru 1975; Evamy et al. 1978). Three lithostratigraphic units have been recognized in the subsurface of the Niger Delta. These are the marine pro-delta shales of Akata (claystones and shales), paralic intervals of Agbada (alternation of sandstones, siltstones and claystones) and continental sequence of

Benin (alluvial sands) formations, all of which are strongly diachronous (Short and Stauble, 1967; Doust, 1990). These three sedimentary environments, typical of most deltaic environments, extend across the whole Niger delta and ranges in age from early Paleocene to Holocene/Recent (Reijerset al., 1997). The lithostratigraphic units are thick, complex sedimentary units deposited rapidly during high-frequency, fluvio-deltaic-eustatic sea level oscillations (Mitchum et al., 1994). The surface upon which they were deposited is underlain by thick, under-compacted unstable mobile shales of the Akata Formation, producing a complex series of gliding surfaces and depobelts. In these depobelts, deposition commonly is controlled by large contemporaneous glide-plane extensional faults and folds (Fig. 2).

Regionally, sediment dispersal in the Niger Delta Basin were controlled by marine

transgressive/regressive cycles related to eustatic sea-level changes with varying duration. Differential subsidence locally influenced sediment accumulation. Collectively, these controls resulted in eleven chronostratigraphically confined delta-wide

megasequences with considerable internal lithological variation (Reijers, 2011). The basin structures and stratigraphy have been controlled by the interplay between rates of sediment supply and subsidence (Doust and Omatsola, 1990).

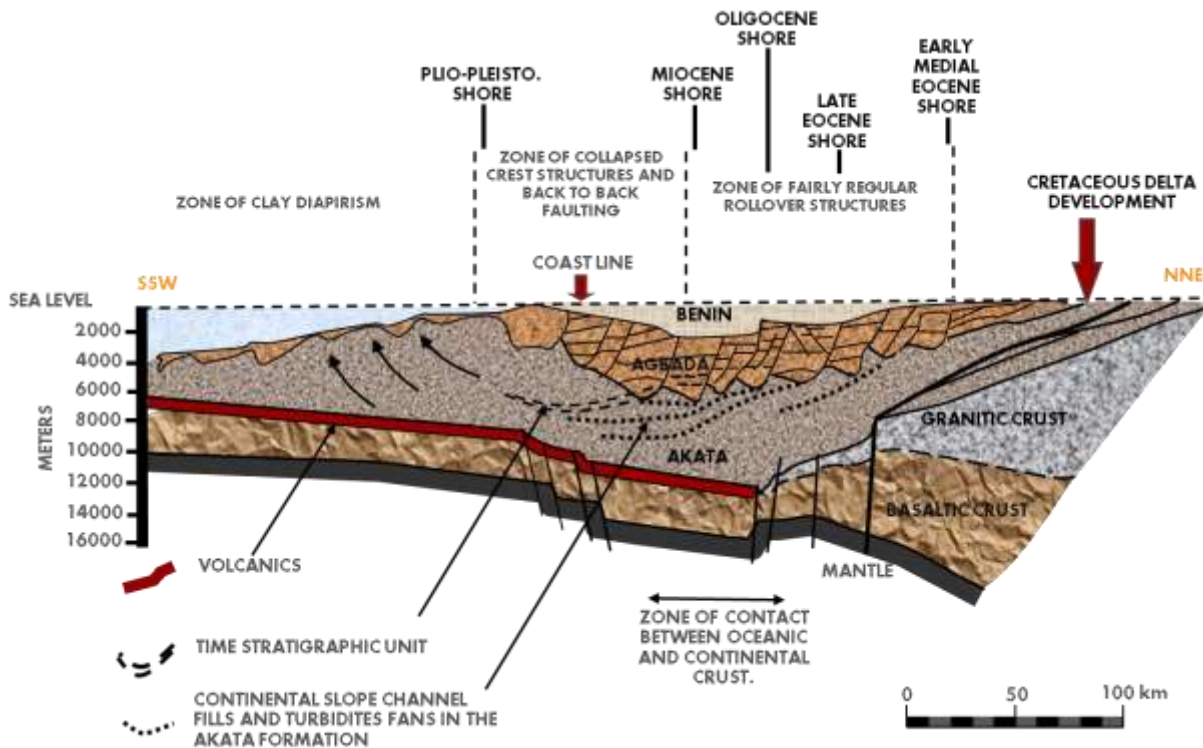


Fig. 2: Schematic Dip Section of the Niger Delta (Modified after Weber and Daukoru, 1975)

Methodology

The study made use of regional merged 3D pre-stack time migrated (PreSTM) seismic data volume of nine fields and twenty-five wells with corresponding suites of wireline logs (Fig. 3). Key delineated stratigraphic bounding surfaces such as maximum flooding surfaces (MFSs) and sequence boundaries (SBs), were tied to well-defined palynological (P) and foraminiferal (F) zones. Maximum flooding surfaces were dated using biostratigraphic markers and were correlated with regional marker shales on the chronostratigraphic chart. In addition, paleobathymetric data (paleo-water depth) were used to constrain stratigraphic bounding surface interpretation (Fig. 4). These were calibrated using Shell Petroleum Development Company's 2010 Niger Delta Chronostratigraphic Chart (zonation schemes) (Fig. 5). These chrono-stratigraphic surfaces were

also correlated on well logs and mapped across the seismic volume respectively. Stacking pattern, system tracts and sequence stratigraphic models (Van Wagoner et al., 1990; Kendall, 2008) aided well log sequence stratigraphic and depositional environment interpretations (Fig. 4). The fault stick picking and horizon mapping were done systematically at very close spacings in order to get as much detail as possible. Time – depth (T-Z) curves (polynomial) were generated from plots using check-shot data for depth-converting time structural maps (Fig. 6). Software used for this research includes; Petrel™ software, which aided in well log correlation, seismic interpretation and generation of structural top maps; Shell's nDI that was used in generating the semblance volume and Interactive Petrophysics™ that was used for reservoir delineation and petrophysical evaluation.

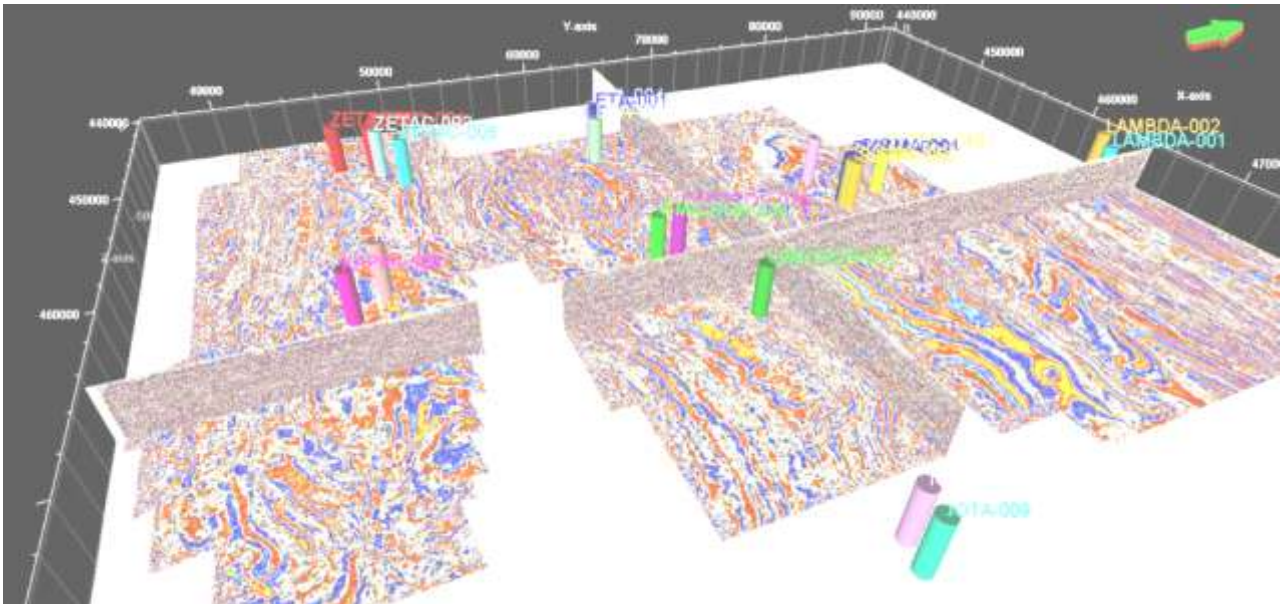
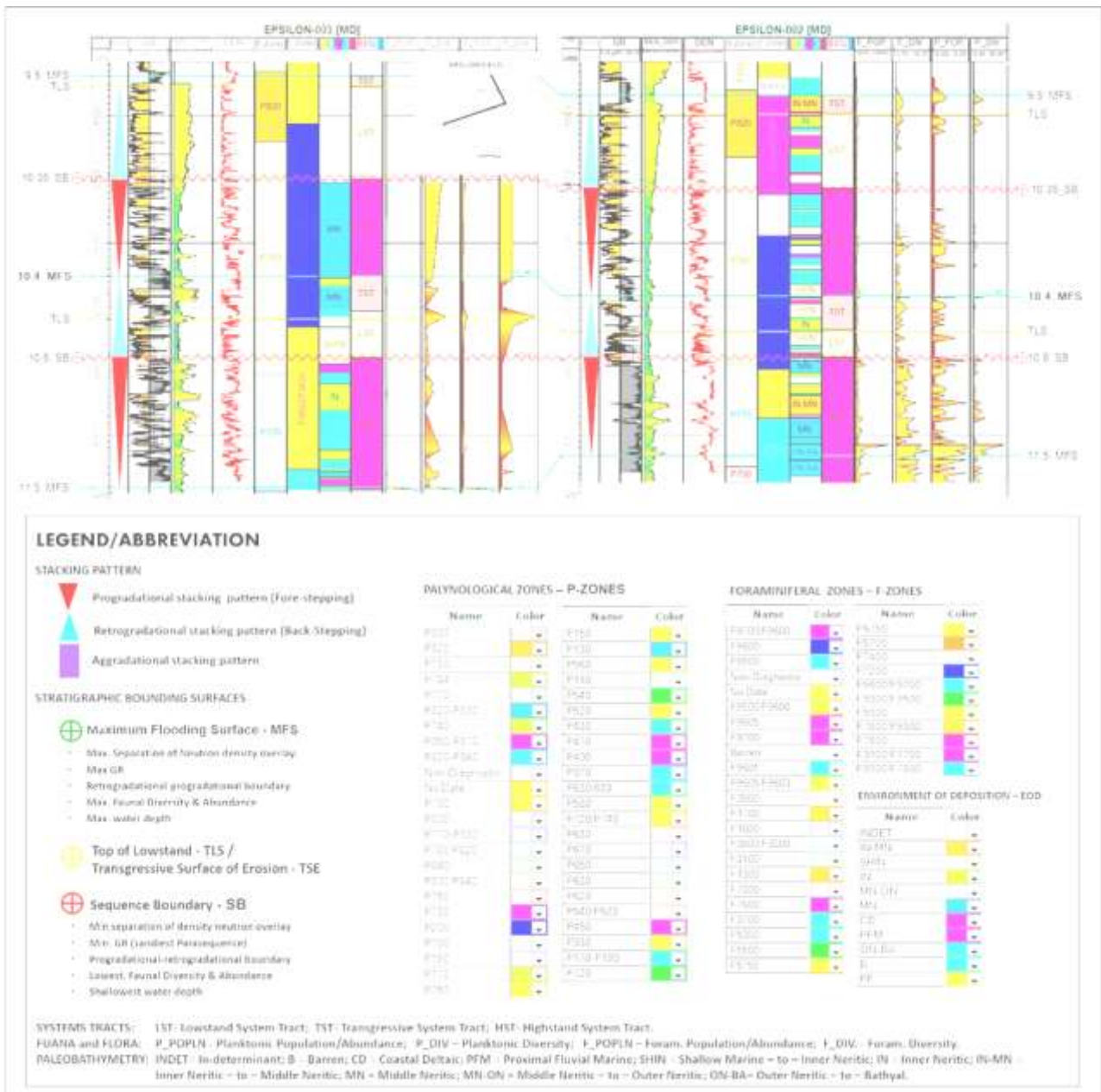


Fig. 3: 3D preSDM seismic volume showing time slice, in-line and cross-line intersections with well bores across the study area (NB: presence of amplitude enhanced stratigraphic and structural features in the time slice).



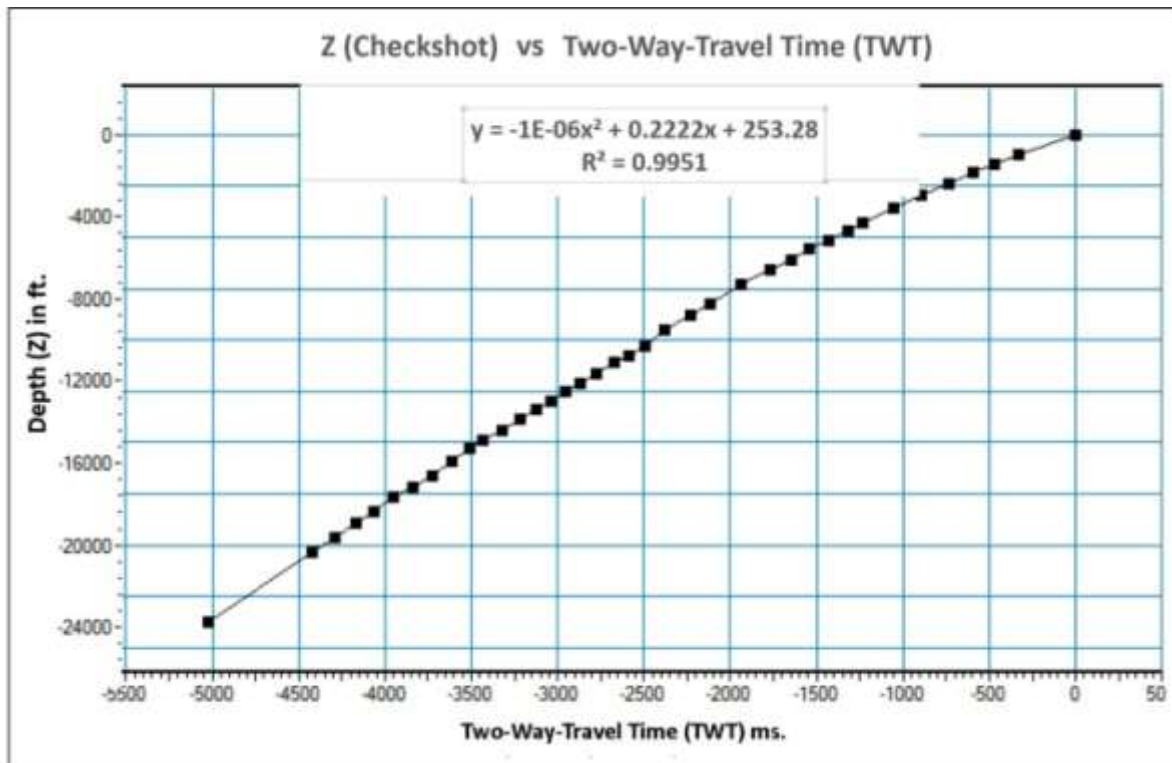


Fig. 6: Polynomial plot (T-Z) showing the time to depth relationship, a curve generated using checkshots from wells.

Results and Discussion

Stratigraphic analysis reveals the occurrence of five sequence boundaries identified in the study area with the oldest identified sequence boundary being dated SB_13.1 Ma. Other Sequence Boundaries are dated 12.1 Ma, 10.6 Ma, 10.35 and 8.5 Ma respectively, based on their relative positions in the stratigraphic sections. In addition, five intervening maximum flooding surfaces were also identified. These surfaces, from the oldest to the youngest with their corresponding bio-zones have been described as follows: (i) 12.8 Ma Maximum Flooding Surface (*Ser-2-Cassidulina* regional marker). The surface occurrence of this event is within P680 and F9300/9500 bio-zones. (ii) 11.5 Ma Maximum Flooding Surface (*Ser-3-Dodo Shale* regional marker). This surface occurred within P770 and F9500/F9600 bio-zones. (iii) 10.4 Ma Maximum Flooding Surface (*Tor-Nonion-4* regional marker), which occurred within P780 and F9600 bio-zones. (iv) 9.5 Ma Maximum Flooding Surface (*Tor-1-Uvigerina-8*

regional marker) that occurred within P820 and F9600 bio-zones. (v) 7.4 Ma Maximum Flooding Surface (*Tor-2* marker). This MFS occurred within P830 and F9700 bio-zones. Four depositional sequences (SEQ1, SEQ2, SEQ3, and SEQ4) and the component systems tracts were recognized. The three systems tracts observed in this study namely, lowstand system tracts (LST), transgressive system tract (TST) and highstand system tract (HST) are all characterized by variable thicknesses that appear to be structurally controlled. The average thickness distribution of these system tracts is such that there is a higher percentage of HST (57%) relative to LST (30%) and much lesser TST (13%) packages. In addition, interpretations reveal that the genetic units of LST (predominantly sand package), TST (predominantly shale package), and HST (sand and shale packages).

The correlation across the fields shows that the main reservoirs (the sand packages of the lowstand systems tract and

highstand systems tract) are within the sequences from 8.5 to 12.1 Ma. (Fig. 7). The occurrence of the identified chronostratigraphic surfaces at different depths along dip and strike directions in the wells shows evidence of structural (faulting) influence on stratigraphy. Hence, the sediments are thinner in the up-dip (northeast) section and thicken down-dip (southwest). Generally, sediment

package thickens on the down thrown section of the major listric / growth fault which characterizes the area in basin-ward directions (N–S). The flattening at various MFS(s) reveals a shift of depocenter from northern section towards the southern which is a typical scenario of the progradational pattern in the Niger Delta Basin. (Modeet *al*, 2015; Dim, 2017).

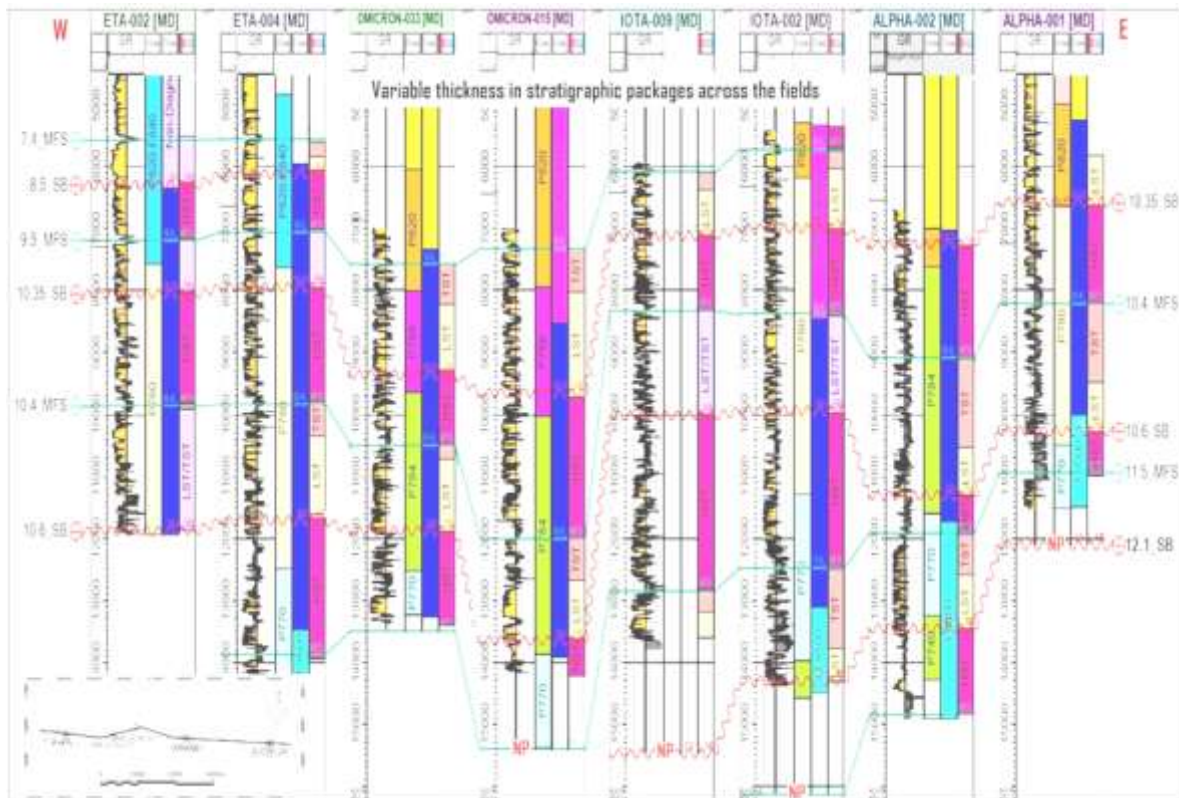


Fig. 7: Well log sequence stratigraphic correlation across representative well from various fields showing key chronostratigraphic surfaces – MFSs and SBs (Note: NP = Not Penetrated/Drilled).

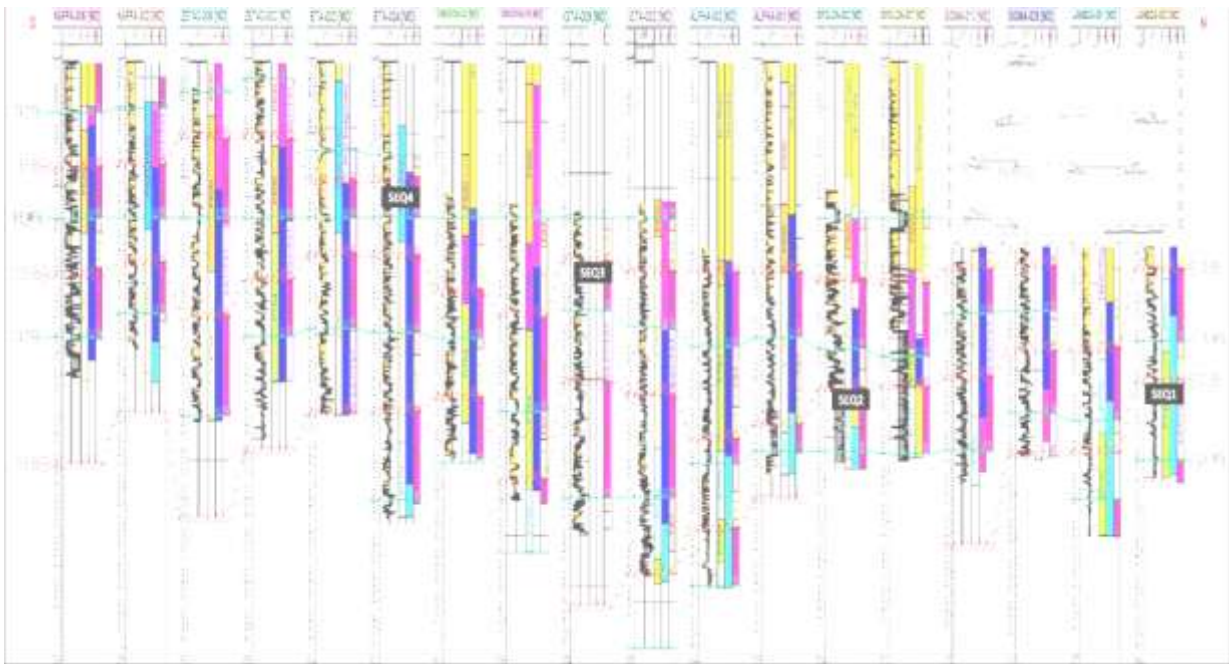


Fig.8: Regional stratigraphic correlation panel flattened at 9.5 Ma. MFS showing a shift of depositional centers toward the southern section of the area.

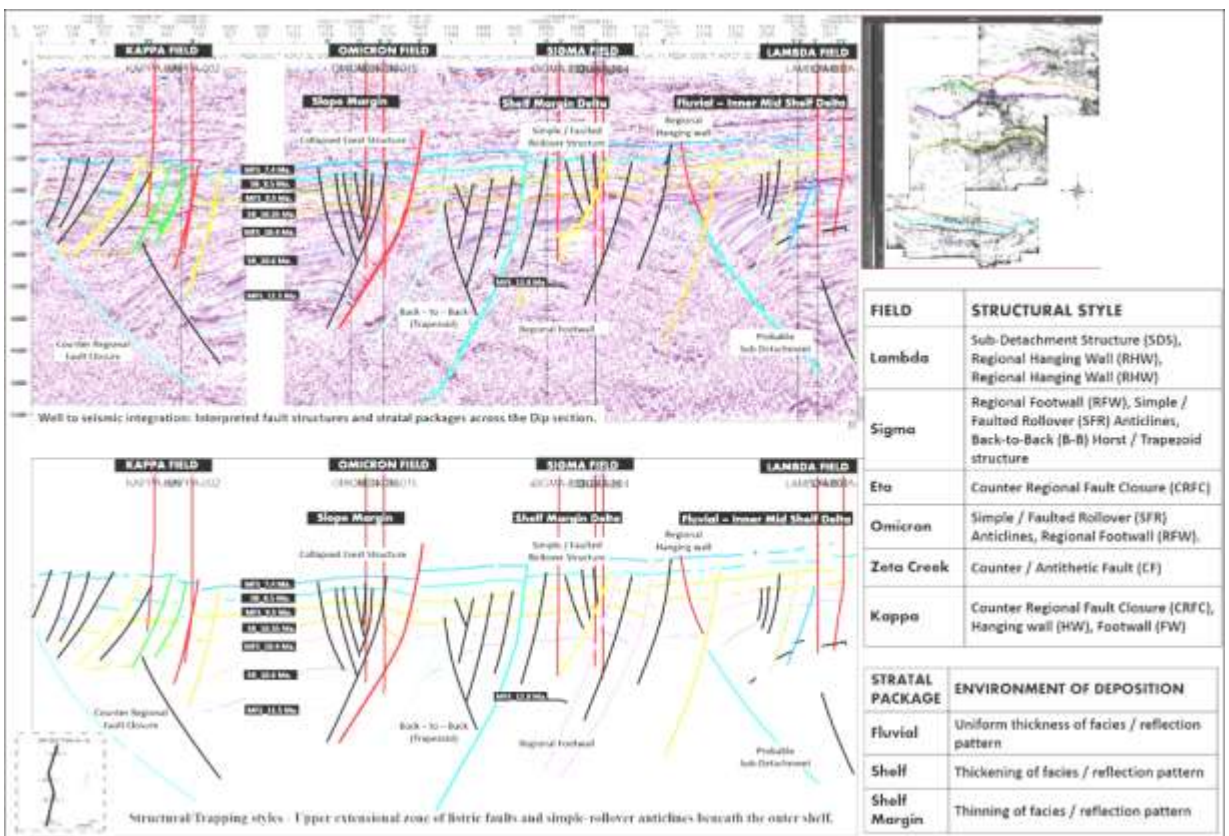


Fig. 9: Multiple dip line sections (using Petrel™ software), showing interpreted stratigraphic surfaces and structural styles across various study area and inset structural semblance map (Adopted from Dim and Onuoha, 2017).

Structural interpretation across the fields reveal down to basin listric faults that are large and regionally extensive. Majority of these faults dip in the same direction as the regional stratigraphy (synthetic faults), whereas few dip against the regional stratigraphic dip (counter regional faults). Generally the following structural configuration / styles were distinguished namely; simple/faulted rollovers, regional footwalls / hanging walls and associated fault dependent closures, back to back horst block (trapezoid zone), collapse crest structures, and sub-detachment structures (Fig. 9).

Reservoir formation evaluation studies indicate that the LST packages of the basin floor fans and channel, and HST packages of the shoreface constitute potential hydrocarbon reservoirs (Fig. 10). The shale unit (marine shales) of the TST, which is capped by MFS, also provides regional seals to the reservoir units. A combination of the reservoir sands of the LST and HST with the shale units of the TST offers good stratigraphic hydrocarbon traps with associated numerous fault structures, associated with rapidly subsiding delta, hence should be targeted during hydrocarbon exploration and

production (Mode *et al*, 2015; Dim, 2017; Dim and Onuoha, 2017).

Studies show that these reservoir intervals are partly compartmentalized and laterally continuous extending regionally across several fields at intermediate and deeper zones (Fig. 11). There is also observable variation in reservoir thickness (with gross thickness of 30.5 – 239ft and a net thickness of 0.5 – 215ft). Reservoir properties such as net-to-gross (0.1 – 0.96 or 10 – 96%), porosity (0.13 – 0.28 or 13 – 28%), water saturation (0.1 – 0.95 or 10 – 95%) and hydrocarbon saturation (0.07 – 0.89 or 7 – 89%) indicate favourable condition for hydrocarbon accumulation and production (Fig. 12 and Table 1). Generated structural time and structural depth maps (Fig. 13a and Fig. 13b) with the seismic attribute attraction (amplitude) map (Fig. 13c) show evidence of booming amplitude, an indication of possible hydrocarbon leads. A closer examination reveals these hydrocarbon leads (potential accumulation but poorly defined and requires more data or evaluation in order to be classified as a prospect) to be predominantly structurally controlled. The leads with high amplitude suggests that the hydrocarbons, which due to their buoyant nature, have been trapped within structural closures (fault dependent closures).

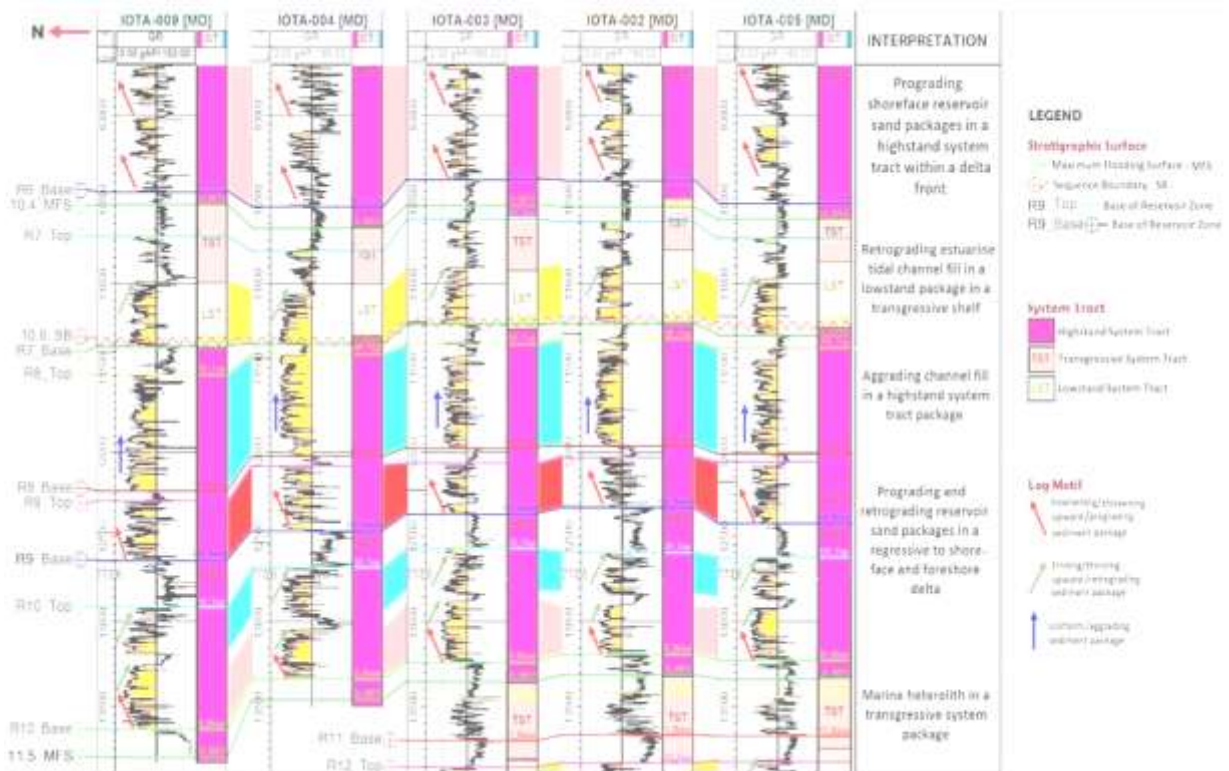


Fig. 10: Interpreted composite well correlation panel across the IOTA field showing the distribution of reservoir packages (R_{TOPS} and R_{BASE}), continuity of sequence stratigraphic surfaces (MFSs and SBs), system tracts (LSTs, TSTs and HSTs) distribution and environments of deposition

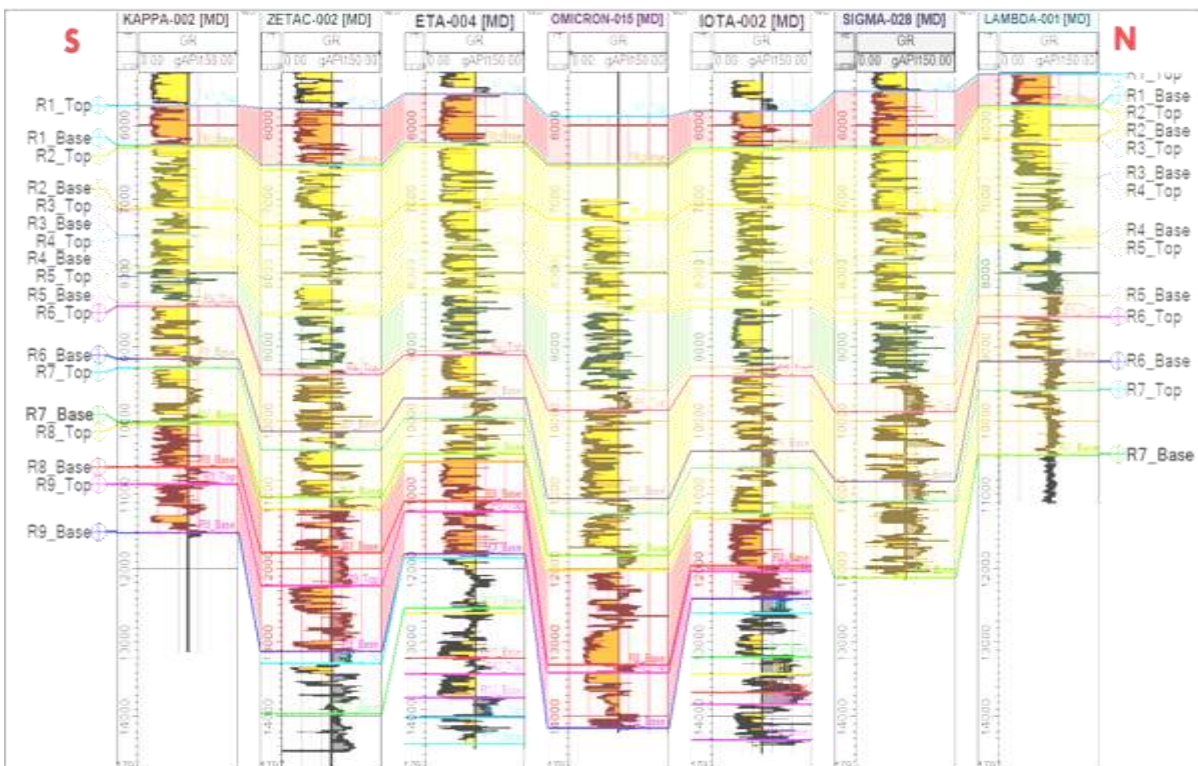


Fig. 11: Well log correlation panel showing spatial distribution of reservoir packages that are correlatable and continuous across several fields in the area (thickening of reservoir package at the central section and thinning at the flanks)

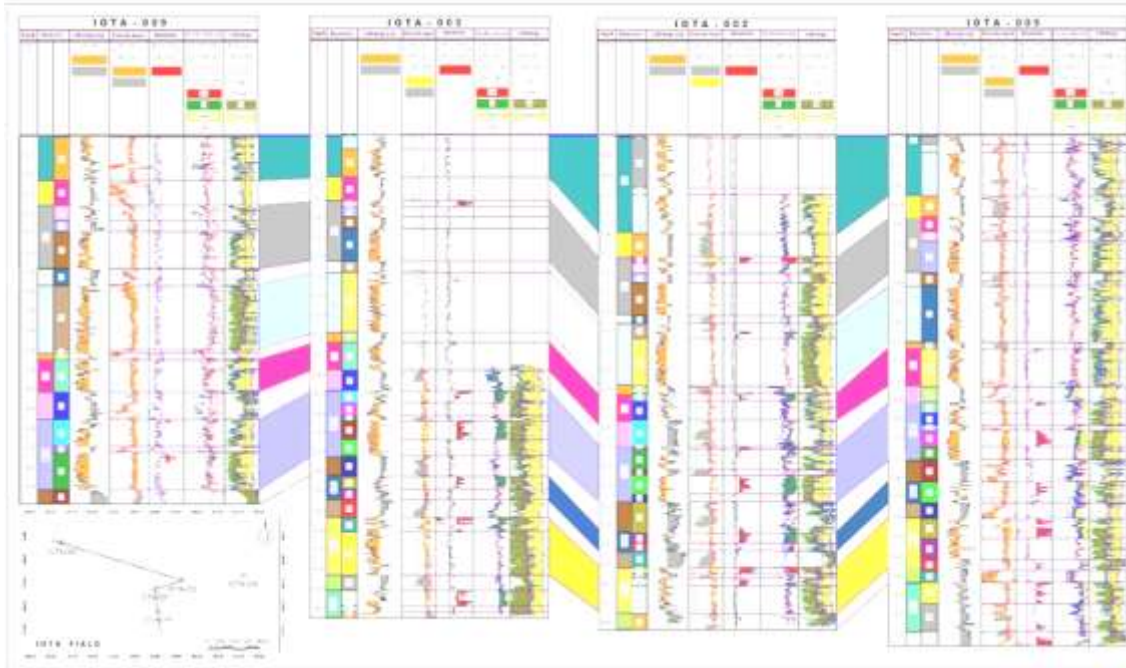


Fig. 12: Intra-well correlation panel on Interactive Petrophysics software interface showing delineated reservoir at intermediate and deeper zones in the Iota field (Iota-002, Iota-003, Iota-005 and Iota-009 wells). Note: Delineated reservoir zones show variable thicknesses and are laterally continuous across the field.

Table 1: Summary of some estimated petro-physical parameters from Iota 002

WELL: IOTA-002										
NET RESERVOIR ROCK SUMMARY										
Reservoir Zone	Top Depth (ft)	Bottom Depth (ft)	Gross Thickness (ft)	Net Thickness (ft)	N/G	Av. Vcl	Av. Phi	Av. Sw	Av. Sh	Fluid Type
R7	10399.5	10638.5	239	21.5	0.09	0.262	0.176	0.923	0.077	Gas
	10638.5	10699.5	61	60	0.984	0.123	0.189	0.176	0.824	
	10699.5	10807.5	108	72.5	0.671	0.145	0.206	0.804	0.196	
	10807.5	10906.5	99	29.5	0.298	0.256	0.139	0.953	0.047	
R8	11237	11399.5	162.5	39.75	0.245	0.195	0.156	0.894	0.106	Water
	11399.5	11475	75.5	59.25	0.785	0.136	0.158	0.365	0.635	
R9	11963.5	12033	69.5	25	0.36	0.212	0.285	0.688	0.312	Oil
	12033	12136	103	93.5	0.908	0.136	0.2	0.234	0.766	
R10	12331	12602.5	271.5	29.25	0.108	0.226	0.177	0.762	0.238	Oil
	12602.5	12633	30.5	29.5	0.967	0.147	0.184	0.129	0.871	
	12633	12841.5	208.5	129	0.619	0.16	0.187	0.791	0.209	
	12841.5	12897.5	56	0.5	0.009	0.264	0.146	0.782	0.218	
R11	12897.5	13090	192.5	178	0.925	0.124	0.176	0.207	0.793	Oil
	13169.5	13486.5	317	64.75	0.204	0.216	0.164	0.516	0.484	
	13486.5	13588	101.5	88.25	0.869	0.159	0.176	0.156	0.844	
R12	13669.5	13840.5	171	4.5	0.026	0.241	0.147	0.657	0.343	Gas/Oil
	13840.5	13901.5	61	51.25	0.84	0.114	0.148	0.103	0.897	
R13	13945	14030	85	62.5	0.735	0.128	0.133	0.249	0.751	Water
	14030	14312	282	215.25	0.763	0.129	0.149	0.869	0.131	
	14312	14479	167	13.75	0.082	0.136	0.135	0.616	0.384	

Note: N/G =net-to-gross, Av. Vcl = average volume of clay, Av. Phi = average effective porosity, Av Sw =average water saturation and AvSh =average hydrocarbon saturation.

Conclusion

Regional geologic studies carried out across several fields, provided a rare opportunity for a better understanding of the stratigraphic and structural framework and reservoir distribution across the eastern Coastal Swamp Depobelt of the Niger Delta Basin. Maximum flooding surfaces mark regional seals and cap the major reservoir units across the various fields in the study area. Observed structural styles and associated entrapment mechanisms fault such as rollover anticlines, fault dependent closures, regional hanging wall and footwalls are typical of those found most giant oil fields of the world. These structural features have thrown

light to several possible existing hydrocarbon leads identified at intermediate and deeper intervals at several zones that are yet to be drilled. In terms of hydrocarbon exploration, the alternation of sands of the LST and HST and the shale units of the TST offer good reservoir and seal / source rocks. Well stratigraphic correlation and event mapping on seismic sections have also helped in unravelling zones and intervals that have not been drilled, but were possibly by-passed. Petrophysical evaluation revealed the presence of hydrocarbon fluid such oil and gas occurring at several reservoir intervals.

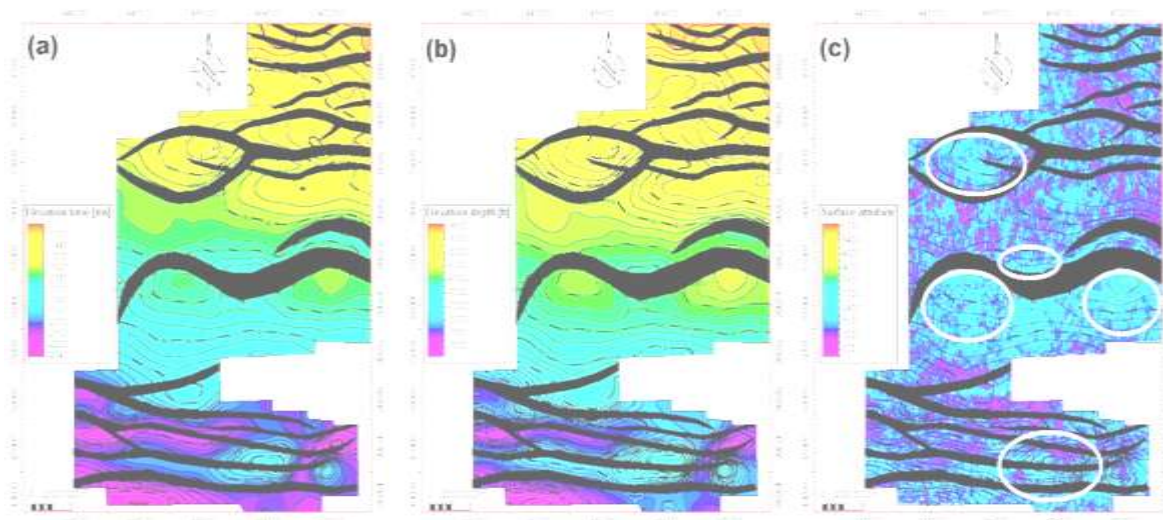


Figure 13. a) Structural time maps (STM), b) Structural depth maps (SDM) c). Amplitude Map with encircled (white ring) section with booming amplitude – hydrocarbon indicator.

The deepest well in the area is 16,000 feet, but beneath are possible leads that could hold great potential in deep and ultra-deep prospects, as seen from seismic sections and structural top maps. Hence, this points to the existence of prospectivity at intermediate and deeper horizons in the eastern Coastal Swamp Depobelt of the Niger Delta Basin.

Acknowledgements

The authors are grateful to the entire Geological Services, Geophysics, Exploration and IT-Help Desk teams of the Shell Petroleum Development

Company of Nigeria Limited for provision of dataset and technical support which were instrumental to the success of this work.

References

- Balogun, A.O. (2003). Sequence Stratigraphy of "X" Field in the Coastal Swamp Depobelt of the Niger Delta, Nigeria. Extended Abstract, AAPG Search and Discovery Article #90017, ©2003 AAPG International Conference, Barcelona, Spain.

- Dim, C.I.P. (2017). Hydrocarbon Prospectivity in the Eastern Coastal Swamp Depo-belt of the Niger Delta Basin – Stratigraphic Framework and Structural Styles, SpringerBriefs in Earth Sciences, 71p. Doi 10.1007/978-3-319-44627-1.
- Dim, C.I.P., and Onuoha, K.M. (2017). Insight into sequence stratigraphic and structural framework of the onshore Niger Delta Basin: Integrating well logs, biostratigraphy, and 3D seismic data. *Arabian Journal of Geosciences*, 10 (14), 1–20.
- Doust, H.(1990). Petroleum Geology of the Niger Delta. Geochemical Society, London, Special Publications, 50, 365 p.
- Doust, H. and Omatsola, E. (1990). Niger Delta: In: J.D. Edwards and P.A. Santogrossi (eds) Divergent/passive margin basins: *American Association of Petroleum Geologists Bulletin Memoir 48*, 239–248.
- Ehinola, O.A., Falode, O.A. and Ologun, T.A. (2010). Sequence Stratigraphic Framework of Nemo Field, Onshore Niger Delta. Abstract, AAPG Search and Discovery Article #90108, ©2010 AAPG International Convention and Exhibition, September 12-15, 2010 Calgary, Alberta, Canada.
- Ejedawe, J. E. (1981). Patterns of incidence of oil reserves in Niger Delta Basin. *American Association of Petroleum Geologists Bulletin*, 65, pp.1574–1585.
- Evamy, B.D., Haremboure, J., Kamerling, P., Knaap, W.A., Molloy, F.A. and Rowlands, P.H. (1978). Hydrocarbon habitat of Tertiary Niger Delta: *American Association of Petroleum Geologists Bulletin*, 62, pp.1–39.
- Kendall, C.G. (2008). Template for “conceptual models” used to interpret depositional systems USC Sequence Stratigraphy Web. <http://strata.geol.sc.edu/index.html>, University of South Carolina.
- Lawrence S.R., Munday, S. and Bray, R. (2002). Regional geology and geophysics of the eastern Gulf of Guinea (Niger Delta to Rio Muni). *The Leading Edge*, 21, 1112–1117.
- Magbagbeola, O.A. and Willis, B.J. (2007). Sequence stratigraphy and syndepositional deformation of the Agbada formation, Robertkiri field, Niger Delta, Nigeria. *American Association of Petroleum Geologists Bulletin*, 91(7), 945–958.
- Mitchum, R.M., Sangree, J.B., Vail, P.R. and Wornardt, W.W. (1994). Recognizing sequences and systems tracts from well logs, seismic data and biostratigraphy: Examples from the Late Cenozoic of the Gulf of Mexico, in P. Weimer and H. W. Posamentier (eds), *American Association of Petroleum Geologists Memoir 58*, 163–197.
- Mode, A.W., Dim, C.I.P. and Ozumba, B.M. (2015). Sequence Stratigraphy and depositional environments of Middle – late Miocene Sediments in the eastern part of the Coastal Swamp Depobelt, Niger Delta Basin, Nigeria. *Arabian Journal of Geosciences*, 8, 9815 – 9827.
- Reijers, T.J.A., Petters, S.W. and Nwajide, C.S. (1997). The Niger Delta Basin. In: R.C. Selley (ed) *African basins. Sedimentary Basins of the World 3*, 145–168.
- Reijers, T.R.A (2011) Stratigraphy and sedimentology of the Niger Delta. *Geologos*, 17(3), 133–162. Doi: 10.2478/v10118-011-0008-3.
- Shell, (2010). SPDC 2010 Chronostratigraphic Scheme – An intermediate update to the current 1998 Niger Delta Cenozoic Chronostratigraphic Chart. Shell Petroleum Development Company UIG-T/DGX Geological Services, Warri.

Short, K.C., and Stauble, A.J.(1967).
Outline of geology of Niger Delta.
*American Association of Petroleum
Geologists Bulletin*, 51, 761–779.

Stacher, P.(1995). Present understanding
of the Niger Delta hydrocarbon habitat; In:
M.N. Oti and G.Postma (eds) *Geology of
Deltas*; A. A. Balkema, Rotterdam, 257–
267.

Van Wagoner, J.C., Mitchum, R.M.,
Campion, K.M., and Rahmanian,

V.D.(1990).Siliciclastic Sequence
Stratigraphy in Well Logs, Cores, and
Outcrops.American Association of
Petroleum Geologists, Tulsa, p.55.

Weber, K.J. and Daukoru, E.M. (1975).
Petroleum geology of the Niger Delta:
*Proceedings of the 9th World Petroleum
Congress, Vol. 2, Geology: London,*
Applied Science Publishers, Ltd., 210–
221.

Iterative Approximation of Fixed Points of k -Strictly Asymptotically Pseudocontractive Mappings Using Averaging Hybrid Scheme

P.U. Nwokoro* and M.O. Osilike

Let H be a real Hilbert space. Weak and strong convergence theorems for approximation of fixed points of k -strictly asymptotically pseudocontractive mapping, $T : H \rightarrow H$ are proved using an averaging hybrid iterative scheme $\{x_n\}_{n=1}^{\infty}$. Furthermore, if H is replaced with an arbitrary Banach space E , necessary and sufficient conditions that guarantee the strong convergence of our iterative scheme, $\{x_n\}$ to a fixed point of T in E are given. Our results extend recent results of Osilike, Isiogugu and Nwokoro (*J. Nigerian Math. Soc.*, **27** (2008), 91-108) which are themselves extensions and generalizations of results of Wang [*Fixed Point Theory and Applications* Vol **2007**, ID 28619 (2007), 1-8, <http://fixedpointtheoryandapplication.springeropen.com/article/10.1155/2007/28619>] from the class of strictly pseudocontractive mappings of Browder-Petryshyn type to the class of k -strictly asymptotically pseudocontractive mappings.

1. Introduction

Let E be an arbitrary real Banach space and let J denote the generalized duality mapping from E into 2^{E^*} given by

$$J(x) = \{f \in E^* : \|f\|^2 = \|x\|^2 = \langle x, f \rangle\},$$

where E^* denotes the dual space of E and $\langle \cdot, \cdot \rangle$ denotes the generalized duality pairing. If E^* is strictly convex, then J is single-valued. In the sequel we shall denote single-valued duality mapping by j .

Let E be a real Banach space. A mapping $T : E \rightarrow E$ is said to be L -Lipschitzian if there exists $L > 0$ such that

$$\|Tx - Ty\| \leq L \|x - y\|, \quad \forall x, y \in E. \quad (1.1)$$

T is said to be *nonexpansive* if $L = 1$ in (1.1).

A mapping T with domain $D(T)$ and range $R(T)$ in E is called *strictly pseudocontractive* in the terminology of Browder and Petryshyn [1] if for all $x, y \in D(T)$ there exist $\lambda > 0$ and $j(x - y) \in J(x - y)$ such that

$$\langle Tx - Ty, j(x - y) \rangle \leq \|x - y\|^2 - \lambda \|x - y - (Tx - Ty)\|^2. \quad (1.2)$$

Fixed Points, k -strictly Asymptotically Pseudocontractive Mappings, Hilbert Spaces, Averaging Hybrid Scheme.

2010 *Mathematics Subject Classification*. 47H10, 47H09, 47H15, 47H17, 65J15

*Corresponding Author

Without loss of generality we may assume that $\lambda \in (0,1)$. If I denotes the identity operator, then (1.2) can be written in the form

$$\langle (I-T)x - (I-T)y, j(x-y) \rangle \geq \lambda \| (I-T)x - (I-T)y \|^2. \quad (1.3)$$

In Hilbert spaces, (1.2) (and hence (1.3)) is equivalent to the inequality

$$\|Tx - Ty\|^2 \leq \|x - y\|^2 + k \| (I-T)x - (I-T)y \|^2, \quad k = (1-2\lambda) < 1. \quad (1.4)$$

From (1.3) we obtain

$\|x - y\| \geq \lambda \|x - y - (Tx - Ty)\| \geq \lambda \|Tx - Ty\| - \lambda \|x - y\|$, for $Tx - Ty \neq x - y$, so that

$$\|Tx - Ty\| \leq \frac{(1+\lambda)}{\lambda} \|x - y\| = L_* \|x - y\|, \quad \forall x, y \in D(T),$$

where $L_* = \frac{(1+\lambda)}{\lambda}$. Hence T is Lipschitz. In Hilbert spaces, it also follows from (1.4) that

$$\|Tx - Ty\| \leq \frac{(1+\sqrt{k})}{(1-\sqrt{k})} \|x - y\| = L_* \|x - y\|, \quad \text{where } L_* = \frac{1+\sqrt{k}}{1-\sqrt{k}}. \text{ Let } E \text{ be an arbitrary real}$$

Banach space, K a nonempty subset of E . A mapping $T : K \rightarrow K$ is called k -strictly asymptotically pseudocontractive with sequences $\{k_n\}_{n=1}^\infty \subseteq [1, \infty)$, $\lim_{n \rightarrow \infty} k_n = 1$ (see for instance [6],[10],[13],[14]), if for all $x, y \in K$, there exists $j(x-y) \in J(x-y)$ and a constant $k \in [0,1)$ such that

$$\langle (I-T^n)x - (I-T^n)y, j(x-y) \rangle \geq \frac{1}{2}(1-k) \| (I-T^n)x - (I-T^n)y \|^2 - \frac{1}{2}(k_n^2 - 1) \|x - y\|^2 \quad (1.5)$$

for all $n \in \mathbb{N}$.

Several authors have studied various methods for the iterative approximation of fixed points of k -strictly asymptotically pseudocontractive maps (see for example [6],[8],[10],[13],[14]). Recently, Wang [18] studied the following iteration method in Hilbert spaces:

The Hybrid Iteration Method (Wang [18]). Let H be a real Hilbert space, $T : H \rightarrow H$ a nonexpansive mapping with $F(T) = \{x \in H : Tx = x\} \neq \emptyset$ and $F : H \rightarrow H$ an L -Lipschitzian mapping which is also η -strongly monotone, where a mapping T is η -strongly monotone if there exists $\eta > 0$ such that

$$\langle Tx - Ty, x - y \rangle \geq \eta \|x - y\|^2, \quad \forall x, y \in H. \quad (1.6)$$

Let $\{\alpha_n\}_{n=1}^\infty$ and $\{\lambda_n\}_{n=1}^\infty$ be real sequences in $[0,1)$, and $\mu > 0$, then the sequence $\{x_n\}_{n=1}^\infty$ is generated from an arbitrary $x_1 \in H$ by

$$x_{n+1} = \alpha_n x_n + (1-\alpha_n) T^{\lambda_{n+1}} x_n, \quad n \geq 1, \quad (1.7)$$

where $T^{\lambda_{n+1}} x_n := Tx_n - \lambda_{n+1} \mu F(Tx_n)$, $\mu > 0$.

Observe that: (i) if $\alpha_n = 0 \forall n$, and $\lambda_n = 0 \forall n > 1$, then (1.7) reduces to the Picard Iteration Scheme

(ii) if $\lambda_n = 0 \forall n \geq 1$, then (1.7) reduces to the Mann Iteration Scheme.

(iii) if $F(x) = x - u$ for some fixed point $u \in H$, then F is Lipschitz and

$\langle F(x) - F(y), x - y \rangle = \|x - y\|^2$. In this case if

$\alpha_n = 0, \forall n \geq 1$, then $x_{n+1} = (\lambda_{n+1}\mu)u + (1 - \lambda_{n+1}\mu)Tx_n$ which is Halpern-type of iteration scheme.

Wang's work was motivated by earlier results of Xu and Kim [19], Yamada [20], and several other related results. Using this iteration method, Wang proved the following main results:

Lemma 1.1 ([18], Page 3). Let H be a real Hilbert space, $T : H \rightarrow H$ a nonexpansive mapping with $F(T) = \{x \in H : Tx = x\} \neq \emptyset$, and $F : H \rightarrow H$ an η -strongly monotone and L -Lipchitzian mapping. Let $\{x_n\}_{n=1}^\infty$ be the sequence generated from an arbitrary $x_1 \in H$ by

$$x_{n+1} = \alpha_n x_n + (1 - \alpha_n) T^{\lambda_{n+1}} x_n, \quad n \geq 1,$$

where $T^{\lambda_{n+1}} x_n := Tx_n - \lambda_{n+1} \mu F(Tx_n)$, $\mu > 0$, and let $\{\alpha_n\}_{n=1}^\infty$ and $\{\lambda_n\}_{n=1}^\infty$ be real sequences in $[0, 1)$ satisfying the conditions:

(i) $0 < \alpha \leq \alpha_n \leq \beta < 1$, for some $\alpha, \beta \in (0, 1)$

(ii) $\sum_{n=1}^\infty \lambda_n < \infty$

(iii) $0 < \mu < \frac{2\eta}{L^2}$.

Then

(a) $\lim_{n \rightarrow \infty} \|x_n - x^*\|$ exists for each $x^* \in F(T)$

(b) $\lim_{n \rightarrow \infty} \|x_n - Tx_n\| = 0$.

Theorem 1.1 ([18], P.5). Let $H, T, F(T), F, \{T^{\lambda_{n+1}}\}_{n=1}^\infty, \{x_n\}_{n=1}^\infty, \{\alpha_n\}_{n=1}^\infty, \{\lambda_n\}_{n=1}^\infty, \mu, \alpha$ and β be as in Lemma 1.1. Let $\{x_n\}_{n=1}^\infty$ be the sequence generated from an arbitrary $x_1 \in H$ by

$$x_{n+1} = \alpha_n x_n + (1 - \alpha_n) T^{\lambda_{n+1}} x_n, \quad n \geq 1,$$

Then

(a) $\{x_n\}_{n=1}^\infty$ converges weakly to a fixed point of T .

(b) $\{x_n\}_{n=1}^\infty$ converges strongly to a fixed point of T if and only if

$\liminf_{n \rightarrow \infty} d(x_n, F(T)) = 0$, where $d(x, F(T)) := \inf \{\|x - p\| : p \in F(T)\}$.

Remark 1.1 Osilike *et al* [11] extended the works of Wang [18] from the class of nonexpansive maps to the more general class of k -strictly pseudocontractive mappings of Browder-Petryshyn type. Osilike *et al* [10] also proved that the class of k -strictly pseudocontractive mappings of Browder-Petryshyn type and that of k -strictly asymptotically pseudocontractive maps are independent.

It is our purpose in this paper to extend Lemma 1.1 and Theorem 1.1 from the class of nonexpansive maps to the class of k -strictly asymptotically pseudocontractive mappings. Furthermore, if E is an arbitrary real Banach space and $T : E \rightarrow E$ is a k -strictly asymptotically pseudocontractive mapping with $F(T) \neq \emptyset$, we obtain necessary and sufficient conditions that guarantee the strong convergence of $\{x_n\}$ to a fixed point of T .

2. Preliminaries

In the sequel we shall need the following: A Banach space E is said to satisfy *Opial's condition* (see for example [5]) if for each sequence $\{x_n\}_{n=1}^\infty$ in E which converges weakly to a point $x \in E$ we have

$$\liminf_{n \rightarrow \infty} \|x_n - x\| < \liminf_{n \rightarrow \infty} \|x_n - y\|, \quad \forall y \in E.$$

Let E be a Banach space. A mapping T with domain $D(T)$ and range $R(T)$ in E is said to be *demiclosed at a point* $p \in D(T)$ if whenever $\{x_n\}_{n=1}^\infty$ is a sequence in E which converges weakly to a point $x \in E$ and $\{Tx_n\}_{n=1}^\infty$ converges strongly to p , then $Tx = p$. Furthermore, T is said to be *demicompact* if whenever $\{x_n\}_{n=1}^\infty$ is a bounded sequence in $D(T)$ such that $\{x_n - Tx_n\}_{n=1}^\infty$ converges strongly, then $\{x_n\}_{n=1}^\infty$ has a subsequence which converges strongly. T is said to satisfy condition (A) if $F(T) \neq \emptyset$ and there exists a nondecreasing function $f : [0, \infty) \rightarrow [0, \infty)$ with $f(0) = 0$ and $f(t) > 0$ for all $t \in (0, \infty)$ such that $\|x - Tx\| \geq f(d(x, F(T)))$ for all $x \in D(T)$, where $d(x, F(T)) := \inf\{\|x - p\| : p \in F(T)\}$.

Lemma 2.1 ([10]) Let E be a real 2-uniformly smooth Banach which is also uniformly convex and let K be a nonempty closed convex subset of E . Let $T : K \rightarrow K$ be a strictly asymptotically pseudocontractive mapping of Browder Petryshyn type. Then $(I - T)$ is demiclosed at zero on K , where I is the identity mapping.

Lemma 2.2 ([7], Page 1184, see also [8]) Let $\{a_n\}_{n=1}^\infty$, $\{b_n\}_{n=1}^\infty$ and $\{\delta_n\}_{n=1}^\infty$ be sequences of nonnegative real numbers satisfying the inequality

$$a_{n+1} \leq (1 + \delta_n)a_n + b_n, \quad n \geq 1.$$

If $\sum_{n=1}^\infty \delta_n < \infty$ and $\sum_{n=1}^\infty b_n < \infty$, then $\lim_{n \rightarrow \infty} a_n$ exists. In particular, if $\{a_n\}_{n=1}^\infty$ has a subsequence which converges strongly to zero, then $\lim_{n \rightarrow \infty} a_n = 0$.

3. Main Results

We prove here, the following results:

Theorem 3.1 Let H be a real Hilbert space, $T : H \rightarrow H$ a k -strictly asymptotically pseudocontractive mapping with $F(T) \neq \emptyset$. and sequence $\{k_n\}_{n=1}^\infty \subseteq [1, \infty)$ such that

$\sum_{n=1}^\infty (k_n - 1) < \infty$. Let $F : H \rightarrow H$ be an L -Lipschitzian mapping. Let $\{x_n\}_{n=1}^\infty$ be the sequence generated from an arbitrary $x_1 \in H$ by

$$x_{n+1} = \alpha_n x_n + (1 - \alpha_n) T^{\lambda_{n+1}} x_n, \quad n \geq 1,$$

where $T^{\lambda_{n+1}} x_n := T^n x_n - \lambda_{n+1} \mu F(T^n x_n)$, $\mu > 0$, and $\{\alpha_n\}_{n=1}^\infty, \{\lambda_n\}_{n=1}^\infty$, are real sequences in $[0, 1)$ satisfying the conditions:

(i) $k < a \leq \alpha_n \leq b < 1$, for some $a, b \in (0, 1)$

(ii) $\sum_{n=1}^{\infty} \lambda_n < \infty$

Then

(a) $\lim_{n \rightarrow \infty} \|x_n - x^*\|$ exists for each $x^* \in F(T)$

(b) $\lim_{n \rightarrow \infty} \|x_n - Tx_n\| = 0$.

(c) $\{x_n\}_{n=1}^{\infty}$ converges weakly to a fixed point of T .

(d) $\{x_n\}_{n=1}^{\infty}$ converges strongly to a fixed point of T if and only if

$\liminf_{n \rightarrow \infty} d(x_n, F(T)) = 0$.

Proof. Let $x^* \in F(T)$ be arbitrary. Then using the well known identity

$$\|\alpha x + (1-\alpha)y\|^2 = \alpha \|x\|^2 + (1-\alpha) \|y\|^2 - \alpha(1-\alpha) \|x - y\|^2$$

which holds in H for all $x, y \in H$ and for all $\alpha \in [0,1]$ we obtain

$$\begin{aligned} \|x_{n+1} - x^*\|^2 &= \|\alpha_n(x_n - x^*) + (1-\alpha_n)(T^n x_n - x^*) - (1-\alpha_n)\lambda_{n+1}\mu F(T^n x_n)\|^2 \\ &= \|\alpha_n(x_n - x^*) + (1-\alpha_n)(T^n x_n - x^*)\|^2 + (1-\alpha_n)^2 \lambda_{n+1}^2 \mu^2 \|F(T^n x_n)\|^2 \\ &\quad - 2(1-\alpha_n)\lambda_{n+1}\mu \langle F(T^n x_n), \alpha_n(x_n - x^*) + (1-\alpha_n)(T^n x_n - x^*) \rangle \\ &\leq \alpha_n \|x_n - x^*\|^2 + (1-\alpha_n) \|T^n x_n - x^*\|^2 - \alpha_n(1-\alpha_n) \|x_n - T^n x_n\|^2 \\ &\quad + (1-\alpha_n)^2 \lambda_{n+1}^2 \mu^2 \|F(T^n x_n)\|^2 \\ &\quad + 2(1-\alpha_n)\lambda_{n+1}\mu \|F(T^n x_n)\| \|\alpha_n(x_n - x^*) + (1-\alpha_n)(T^n x_n - x^*)\| \\ &\leq \alpha_n \|x_n - x^*\|^2 + (1-\alpha_n)[k_n \|x_n - x^*\|^2 + k \|x_n - T^n x_n\|^2] \\ &\quad - \alpha_n(1-\alpha_n) \|x_n - T^n x_n\|^2 + (1-\alpha_n)^2 \lambda_{n+1}^2 \mu^2 \|F(T^n x_n)\|^2 \\ &\quad + 2(1-\alpha_n)\lambda_{n+1}\mu \|F(T^n x_n)\| \|\alpha_n(x_n - x^*) + (1-\alpha_n)(T^n x_n - x^*)\| \\ &= \|x_n - x^*\|^2 + (1-\alpha_n)(k_n - 1) \|x_n - x^*\|^2 \\ &\quad - (1-\alpha_n)(\alpha_n - k) \|x_n - Tx_n\|^2 + (1-\alpha_n)^2 \lambda_{n+1}^2 \mu^2 \|F(T^n x_n)\|^2 \\ &\quad + 2(1-\alpha_n)\lambda_{n+1}\mu \|F(T^n x_n)\| \|\alpha_n(x_n - x^*) + (1-\alpha_n)(T^n x_n - x^*)\| \end{aligned} \tag{1.7}$$

Observe that

$$\|F(T^n x_n)\| \leq LL_* \|x_n - x^*\| + \|F(x^*)\|, \tag{1.8}$$

and

$$\|\alpha_n(x_n - x^*) + (1-\alpha_n)(T^n x_n - x^*)\| \leq (1+L_*) \|x_n - x^*\|. \tag{1.9}$$

Using (1.7) and (1.8) in (1.9) we obtain

$$\begin{aligned} \|x_{n+1} - x^*\|^2 &\leq \|x_n - x^*\|^2 + (1-\alpha_n)(k_n - 1) \|x_n - x^*\|^2 - (1-\alpha_n)(\alpha_n - k) \|x_n - T^n x_n\|^2 \\ &\quad + (1-\alpha_n)^2 \lambda_{n+1}^2 \mu^2 [(LL_*)^2 \|x_n - x^*\|^2 + 2LL_* \|x_n - x^*\| \|F(x^*)\| + \|F(x^*)\|^2] \\ &\quad + 2(1-\alpha_n)\lambda_{n+1}\mu [LL_* \|x_n - x^*\| + \|F(x^*)\|] (1+L_*) \|x_n - x^*\| \\ &= \|x_n - x^*\|^2 + (1-\alpha_n)(k_n - 1) \|x_n - x^*\|^2 - (1-\alpha_n)(\alpha_n - k) \|x_n - T^n x_n\|^2 \\ &\quad + (1-\alpha_n)^2 \lambda_{n+1}^2 \mu^2 (LL_*)^2 \|x_n - x^*\|^2 + 2LL_*(1-\alpha_n)^2 \lambda_{n+1}^2 \mu^2 \|x_n - x^*\| \\ &\quad \times \|F(x^*)\| + (1-\alpha_n)^2 \lambda_{n+1}^2 \mu^2 \|F(x^*)\|^2 \\ &\quad + 2(1-\alpha_n)\lambda_{n+1}\mu LL_*(1+L_*) \|x_n - x^*\|^2 \\ &\quad + 2(1-\alpha_n)\lambda_{n+1}\mu(1+L_*) \|x_n - x^*\| \|F(x^*)\| \\ &\leq \|x_n - x^*\|^2 + (1-\alpha_n)(k_n - 1) \|x_n - x^*\|^2 - (1-\alpha_n)(\alpha_n - k) \|x_n - T^n x_n\|^2 \end{aligned}$$

$$\begin{aligned}
 & + (1-\alpha_n)^2 \lambda_{n+1}^2 \mu^2 (LL_*)^2 \|x_n - x^*\|^2 + 2LL_*(1-\alpha_n)^2 \lambda_{n+1}^2 \mu^2 \|x_n - x^*\|^2 \\
 & + 2LL_*(1-\alpha_n)^2 \lambda_{n+1}^2 \mu^2 \|F(x^*)\|^2 + (1-\alpha_n)^2 \lambda_{n+1}^2 \mu^2 \|F(x^*)\|^2 \\
 & + 2(1-\alpha_n)\lambda_{n+1}\mu LL_*(1+L_*) \|x_n - x^*\|^2 + 2(1-\alpha_n)\lambda_{n+1}\mu(1+L_*) \|x_n - x^*\|^2 \\
 & + 2(1-\alpha_n)\lambda_{n+1}\mu(1+L_*) \|F(x^*)\|^2 \\
 & = [1+(1-\alpha_n)(k_n-1)+(1-\alpha_n)^2 \lambda_{n+1}^2 \mu^2 (LL_*(2+LL_*)) \\
 & + 2(1-\alpha_n)\lambda_{n+1}\mu(1+L_*)(1+LL_*)] \|x_n - x^*\|^2 \\
 & - (1-\alpha_n)(\alpha_n - k) \|x_n - T^n x_n\|^2 \\
 & + [(1-\alpha_n)^2 \lambda_{n+1}^2 \mu^2 (1+2LL_*) \\
 & + 2(1-\alpha_n)\lambda_{n+1}\mu(1+L_*)] \|F(x^*)\|^2 \\
 & \leq [1+a_n] \|x_n - x^*\|^2 - (1-b)(a-k) \|x_n - T^n x_n\|^2 + b_n, \tag{1.10}
 \end{aligned}$$

where,

$a_n = (1+(1-\alpha_n)(k_n-1)+(1-\alpha_n)^2 \lambda_{n+1}^2 \mu^2 (LL_*(2+LL_*))+2(1-\alpha_n)\lambda_{n+1}\mu(1+L_*)(1+LL_*))$, and

$$b_n = [(1-\alpha_n)^2 \lambda_{n+1}^2 \mu^2 (1+2LL_*) + 2(1-\alpha_n)\lambda_{n+1}\mu(1+L_*)] \|F(x^*)\|^2.$$

It follows from Lemma 2.2 and equation (1.10) that $\lim_{n \rightarrow \infty} \|x_n - x^*\|$ exists, completing the proof of

(a).

Since $\{\|x_n - x\|\}$ is bounded, there exist $M > 0$ such that $\|x_n - x^*\|^2 \leq M$ for all $n \geq 1$. Thus it follows from (1.10) that

$$\|x_{n+1} - x^*\|^2 \leq \|x_n - x^*\|^2 - (1-b)(a-k) \|x_n - T^n x_n\|^2 + \sigma_n, \tag{1.11}$$

where $\sigma_n = b_n + Ma_n$, so that

$$\sum_{j=1}^n (1-b)(a-k) \|x_j - T^j x_j\|^2 \leq \|x_1 - x^*\|^2 + \sum_{j=1}^n \sigma_j,$$

and since $\sum_{n=1}^{\infty} \sigma_n < \infty$, it follows that $\lim_{n \rightarrow \infty} \|x_n - T^n x_n\| = 0$. Furthermore

$$\begin{aligned}
 \|x_{n+1} - x_n\| & = \|\alpha_n x_n + (1-\alpha_n)T^{\lambda_{n+1}} x_n - x_n\| \\
 & = (1-\alpha_n) \|T^{\lambda_{n+1}} x_n - x_n\| \\
 & \leq (1-\alpha_n) \|x_n - T^n x_n\| + (1-\alpha_n)\lambda_{n+1}\mu F \|T^n x_n\| \\
 & \leq (1-\alpha_n) \|x_n - T^n x_n\| + (1-\alpha_n)\lambda_{n+1}\mu [LL_* \|x_n - x^*\| + F(x^*)].
 \end{aligned}$$

Hence $\|x_{n+1} - x_n\| \rightarrow 0$ as $n \rightarrow \infty$.

Observe that

$$\begin{aligned}
 \|x_n - Tx_n\| & \leq \|x_n - T^n x_n\| + \|T^n x_n - Tx_n\| \\
 & \leq \|x_n - T^n x_n\| + L_* \|T^{n-1} x_n - x_n\| \\
 & \leq \|x_n - T^n x_n\| + L_* [\|T^{n-1} x_n - T^{n-1} x_{n-1}\| + \|T^{n-1} x_{n-1} - x_n\|] \\
 & \leq \|x_n - T^n x_n\| + L_*^2 \|x_n - x_{n-1}\| + L_* \|T^{n-1} x_{n-1} - x_{n-1}\| + L_* \|x_{n-1} - x_n\| \\
 & \leq \|x_n - T^n x_n\| + L_* \|x_{n-1} - T^{n-1} x_{n-1}\| + L_*(1+L_*) \|x_n - x_{n-1}\|.
 \end{aligned}$$

It follows that $\lim_{n \rightarrow \infty} \|x_n - Tx_n\| = 0$ and this completes the proof of (b).

From Osilike *et al* [10] $(I - T)$ is demiclosed at zero (since every Hilbert space is 2 -uniformly smooth). Since $\{x_n\}$ is bounded and H is reflexive, then $\{x_n\}$ has a weakly convergent

subsequence $\{x_{n_j}\}_{j=1}^{\infty}$. Assuming $x_{n_j} \rightarrow p$. Then $p \in K$, because K is closed and convex and

hence weakly closed. Since $\|x_{n_j} - Tx_{n_j}\| \rightarrow 0$ as $j \rightarrow \infty$, it follows from the demiclosedness

property of $(I - T)$ at zero that $p \in F(T)$. Using the Opial's Condition it follows from standard argument that $\{x_n\}$ converges weakly to $p \in F(T)$ and this completes the proof of (c).

We now prove (d). Observe that if $\{x_n\}_{n=1}^\infty$ converges strongly to a fixed point p of T , then

$$\lim_{n \rightarrow \infty} \|x_n - p\| = 0. \text{ Since}$$

$$0 \leq d(x_n, F(T)) \leq \|x_n - p\|$$

we have $\liminf_{n \rightarrow \infty} d(x_n, F(T)) = 0$. Conversely, suppose $\liminf_{n \rightarrow \infty} d(x_n, F(T)) = 0$. Then from (1.11)

we obtain

$$\text{Thus } \|x_{n+1} - p\|^2 \leq \|x_n - p\|^2 + \sigma_n.$$

and it follows that $a_{n+1} \leq a_n$, where $a_n = d^2(x_n, F(T))$

$$d(x_{n+1}, F(T)) \leq d(x_n, F(T)) + \sigma_n.$$

It follows from Lemma (2.2) that $\lim_{n \rightarrow \infty} d(x_n, F(T))$ exists and since $\liminf_{n \rightarrow \infty} d(x_n, F(T)) = 0$ we

have $\lim_{n \rightarrow \infty} d(x_n, F(T)) = 0$. Thus for arbitrary $\varepsilon > 0$, there exists a positive integer N_1 such that

$d(x_n, F(T)) < \frac{\varepsilon}{4}$, $\forall n \geq N_1$. Furthermore, $\sum_{n=1}^\infty \sigma_n < \infty$ implies that there exists a positive integer

N_2 such that $\sum_{j=n}^\infty \sigma_j < \frac{\varepsilon^2}{16}$, $\forall n \geq N_2$. Choose $N = \max\{N_1, N_2\}$, then $d(x_N, F(T)) < \frac{\varepsilon}{4}$ and

$\sum_{j=N}^\infty \sigma_j < \frac{\varepsilon^2}{16}$. It follows from (1.11) that for all $n, m \geq N$ and for all $p \in F(T)$ we have

$$\begin{aligned} \|x_n - x_m\|^2 &\leq (\|x_n - p\| + \|x_m - p\|)^2 \\ &\leq 2[\|x_n - p\|^2 + \|x_m - p\|^2] \\ &\leq 2[\|x_N - p\|^2 + \sum_{j=N+1}^n \sigma_j + \|x_N - p\|^2 + \sum_{j=N+1}^m \sigma_j] \\ &\leq 4\|x_N - p\|^2 + 4\sum_{j=N}^\infty \sigma_j \quad \forall n, m \geq N. \end{aligned}$$

Thus

$$\|x_n - x_m\| \leq 2\|x_N - p\| + 2\left(\sum_{j=N}^\infty \sigma_j\right)^{\frac{1}{2}}.$$

Taking infimum over all $p \in F(T)$, we obtain

$$\|x_n - x_m\| \leq 2d(x_N, F(T)) + 2\left(\sum_{j=N}^\infty \sigma_j\right)^{\frac{1}{2}} < \varepsilon, \quad \forall n, m \geq N.$$

Thus $\{x_n\}_{n=1}^\infty$ is Cauchy. Suppose $\lim_{n \rightarrow \infty} x_n = u$, then since T is continuous and $\lim_{n \rightarrow \infty} \|x_n - Tx_n\| = 0$,

we have $u \in F(T)$. This completes the proof of Theorem 3.1. \uparrow

Remark 3.1. It follows from Lemma 2.2 and Theorem 3.1 that under the hypothesis of Theorem 3.1, $\{x_n\}_{n=1}^\infty$ converges strongly to a fixed point p of T if and only if $\{x_n\}_{n=1}^\infty$ has a subsequence $\{x_{n_j}\}_{j=1}^\infty$ which converges strongly to p . Thus under the hypothesis of Theorem 3.1, if T is in

addition completely continuous or demicontact, then $\{x_n\}_{n=1}^\infty$ converges strongly to a fixed point of T .

Furthermore, if T satisfies condition (A), then $\liminf_{n \rightarrow \infty} d(x_n, F(T)) = 0$, so that if in addition to the hypothesis of Theorem 3.1 T satisfies condition (A), then $\{x_n\}_{n=1}^\infty$ converges strongly to a fixed point of T .

Remark 3.2. Theorem 3.1 and Remark 3.1 extend the results of [18] from the class of nonexpansive maps to the more general class of strictly asymptotically pseudocontractive maps. Furthermore, the strong monotonicity condition imposed on F in [18] is not required in our results.

Prototypes of our real sequences $\{\alpha_n\}_{n=1}^\infty$ and $\{\lambda_n\}_{n=1}^\infty$ are: $\alpha_n = k + \frac{n(1-k)}{2(n+1)}$, $n \geq 1$ and

$$\lambda_n = \frac{1}{(n+1)^2}, \quad n \geq 1,$$

where $k \in [0, 1)$ is the constant parameter the definition of the operator.

Theorem 3.2 Let E be a real Banach space, $T : E \rightarrow E$ a k -strictly asymptotically pseudocontractive mapping with $F(T) \neq \emptyset$ and sequence $\{k_n\}_{n=1}^\infty \subseteq [1, \infty)$ such that

$\sum_{n=1}^\infty (k_n - 1) < \infty$. Let $F : E \rightarrow E$ be an L -Lipschitzian mapping. Let $\{x_n\}_{n=1}^\infty$ be the sequence generated from an arbitrary $x_1 \in E$ by

$$x_{n+1} = \alpha_n x_n + (1 - \alpha_n) T^{\lambda_{n+1}} x_n, \quad n \geq 1,$$

where $T^{\lambda_{n+1}} x_n := T^n x_n - \lambda_{n+1} \mu F(T^n x_n)$, $\mu > 0$, and $\{\alpha_n\}_{n=1}^\infty, \{\lambda_n\}_{n=1}^\infty$, are real sequences in $[0, 1)$ satisfying the conditions:

- (i) $\sum_{n=1}^\infty (1 - \alpha_n) = \infty$
- (ii) $\sum_{n=1}^\infty (1 - \alpha_n)^2 < \infty$
- (iii) $\sum_{n=1}^\infty \lambda_n < \infty$.

Then

- (a) $\lim_{n \rightarrow \infty} \|x_n - x^*\|$ exists for each $x^* \in F(T)$
- (b) $\liminf_{n \rightarrow \infty} \|x_n - T x_n\| = 0$.
- (c) $\{x_n\}_{n=1}^\infty$ converges strongly to a fixed point of T if and only if $\liminf_{n \rightarrow \infty} d(x_n, F(T)) = 0$.

Proof. Let $x^* \in F(T)$ be arbitrary. Then using the well known inequality

$$\|x + y\|^2 \leq \|x\|^2 + 2\langle y, j(x + y) \rangle$$

which holds for all $x, y \in E$ and $j(x + y) \in J(x + y)$ we obtain

$$\begin{aligned} \|x_{n+1} - x^*\|^2 &= \|x_n - x^* + (1 - \alpha_n)[T^n x_n - x_n - \lambda_{n+1} \mu F(T^n x_n)]\|^2 \\ &\leq \|x_n - x^*\|^2 + 2(1 - \alpha_n) \langle T^n x_n - x_n - \lambda_{n+1} \mu F(T^n x_n), j(x_{n+1} - x^*) \rangle \\ &= \|x_n - x^*\|^2 + 2(1 - \alpha_n) \langle T^n x_n - x_n, j(x_{n+1} - x^*) \rangle \\ &\quad - 2(1 - \alpha_n) \lambda_{n+1} \mu \langle F(T^n x_n), j(x_{n+1} - x^*) \rangle \end{aligned}$$

$$\begin{aligned}
 &= \|x_n - x^*\|^2 - 2(1-\alpha_n)\langle x_{n+1} - T^n x_{n+1}, j(x_{n+1} - x^*) \rangle \\
 &+ 2(1-\alpha_n)\langle x_{n+1} - T^n x_{n+1}, j(x_{n+1} - x^*) \rangle \\
 &+ 2(1-\alpha_n)\langle T^n x_n - x_n, j(x_{n+1} - x^*) \rangle \\
 &- 2(1-\alpha_n)\lambda_{n+1}\mu\langle F(T^n x_n), j(x_{n+1} - x^*) \rangle \\
 \leq &\|x_n - x^*\|^2 - 2(1-\alpha_n)\left[\frac{1}{2}(1-k)\|x_{n+1} - T^n x_{n+1}\|^2 - \frac{1}{2}(k_n - 1)\|x_{n+1} - x^*\|^2\right] \\
 &+ 2(1-\alpha_n)\langle x_{n+1} - x_n, j(x_{n+1} - x^*) \rangle \\
 &+ 2(1-\alpha_n)\langle T^n x_n - T^n x_{n+1}, j(x_{n+1} - x^*) \rangle \\
 &- 2(1-\alpha_n)\lambda_{n+1}\mu\langle F(T^n x_n), j(x_{n+1} - x^*) \rangle \\
 \leq &\|x_n - x^*\|^2 - (1-\alpha_n)(1-k)\|x_{n+1} - T^n x_{n+1}\|^2 \\
 &+ (1-\alpha_n)(k_n - 1)\|x_{n+1} - x^*\|^2 + 2(1-\alpha_n)\langle x_{n+1} - x_n, j(x_{n+1} - x^*) \rangle \\
 &+ 2(1-\alpha_n)\langle T^n x_n - T^n x_{n+1}, j(x_{n+1} - x^*) \rangle \\
 &- 2(1-\alpha_n)\lambda_{n+1}\mu\langle F(T^n x_n), j(x_{n+1} - x^*) \rangle \\
 \leq &\|x_n - x^*\|^2 - (1-\alpha_n)(1-k)\|x_{n+1} - T^n x_{n+1}\|^2 \\
 &+ (1-\alpha_n)(k_n - 1)\|x_{n+1} - x^*\|^2 \\
 &+ 2(1-\alpha_n)\|x_n - x_{n+1}\|\|x_{n+1} - x^*\| \\
 &+ 2(1-\alpha_n)L_*\|x_n - x_{n+1}\|\|x_{n+1} - x^*\| \\
 &+ 2(1-\alpha_n)\lambda_{n+1}\mu\|F(T^n x_n)\|\|x_{n+1} - x^*\| \\
 = &\|x_n - x^*\|^2 - (1-\alpha_n)(1-k)\|x_{n+1} - T^n x_{n+1}\|^2 \\
 &+ (1-\alpha_n)(k_n - 1)\|x_{n+1} - x^*\|^2 \\
 &+ 2(1-\alpha_n)^2(1+L_*)^2\|x_n - x^*\|\|x_{n+1} - x^*\| \\
 &+ 2(1-\alpha_n)^2(1+L_*)\lambda_{n+1}\mu\|F(T^n x_n)\|\|x_{n+1} - x^*\| \\
 &+ 2(1-\alpha_n)\lambda_{n+1}\mu\|F(T^n x_n)\|\|x_{n+1} - x^*\| \tag{1.12}
 \end{aligned}$$

Observe that,

$$\|x_{n+1} - x^*\| \leq (1+L_*)\|x_n - x^*\| + (1-\alpha_n)\lambda_{n+1}\mu\|F(T^n x_n)\|. \tag{1.13}$$

Substituting (1.13) into (1.12) yields

$$\begin{aligned}
 \|x_{n+1} - x^*\|^2 \leq &\|x_n - x^*\|^2 - (1-\alpha_n)(1-k)\|x_{n+1} - T^n x_{n+1}\|^2 \\
 &+ [(1-\alpha_n)(k_n - 1)]\|x_n - x^*\|^2 \\
 &+ 2(1+L_*)(1-\alpha_n)\lambda_{n+1}\mu\|x_n - x^*\|\|F(T^n x_n)\| + (1-\alpha_n)^2\lambda_{n+1}^2\mu^2\|F(T^n x_n)\|^2 \\
 &+ 2(1-\alpha_n)^2(1+L_*)^2\|x_n - x^*\|\|(1+L_*)\|x_n - x^*\| + (1-\alpha_n)\lambda_{n+1}\mu\|F(T^n x_n)\| \\
 &+ 2(1-\alpha_n)^2(1+L_*)\lambda_{n+1}\mu\|F(T^n x_n)\|\|(1+L_*)\|x_n - x^*\| + (1-\alpha_n)\lambda_{n+1}\mu\|F(T^n x_n)\| \\
 &+ 2(1-\alpha_n)\lambda_{n+1}\mu\|F(T^n x_n)\|\|(1+L_*)\|x_n - x^*\| + (1-\alpha_n)\lambda_{n+1}\mu\|F(T^n x_n)\| \\
 = &\|x_n - x^*\|^2 - (1-\alpha_n)(1-k)\|x_{n+1} - T^n x_{n+1}\|^2 \\
 &+ (1-\alpha_n)(k_n - 1)(1+L_*)^2\|x_n - x^*\|^2 \\
 &+ 2(1-\alpha_n)^2(k_n - 1)(1+L_*)\lambda_{n+1}\mu\|x_n - x^*\|\|F(T^n x_n)\| \\
 &+ (1-\alpha_n)^3(k_n - 1)\lambda_{n+1}^2\mu^2\|F(T^n x_n)\|^2 \\
 &+ 2(1-\alpha_n)^2(1+L_*)^3\|x_n - x^*\|^2
 \end{aligned}$$

$$\begin{aligned}
 &+ 2(1-\alpha_n)^3(1+L_*)^2\lambda_{n+1}\mu\|x_n-x^*\| \|F(T^n x_n)\| \\
 &+ 2(1-\alpha_n)^2(1+L_*)^2\lambda_{n+1}\mu\|x_n-x^*\| \|F(T^n x_n)\| \\
 &\quad + 2(1-\alpha_n)^3(1+L_*)\lambda_{n+1}^2\mu^2\|F(T^n x_n)\|^2 \\
 &+ 2(1-\alpha_n)(1+L_*)\lambda_{n+1}\mu\|x_n-x^*\| \|F(T^n x_n)\| \\
 &+ 2(1-\alpha_n)^2\lambda_{n+1}^2\mu^2\|F(T^n x_n)\|^2 \\
 \leq &\|x_n-x^*\|^2-(1-\alpha_n)(1-k)\|x_{n+1}-T^n x_{n+1}\|^2 \\
 &+ (1-\alpha_n)(k_n-1)(1+L_*)^2\|x_n-x^*\|^2 \\
 &+ (1-\alpha_n)^2(k_n-1)(1+L_*)\lambda_{n+1}\mu[\|x_n-x^*\|^2+\|F(T^n x_n)\|^2] \\
 &+ (1-\alpha_n)^3(k_n-1)\lambda_{n+1}^2\mu^2\|F(T^n x_n)\|^2 \\
 &+ 2(1-\alpha_n)^2(1+L_*)^3\|x_n-x^*\|^2 \\
 &+ [(1-\alpha_n)^2(1+L_*)^2(2-\alpha_n)\lambda_{n+1}\mu[\|x_n-x^*\|^2+\|F(T^n x_n)\|^2] \\
 &+ 2(1-\alpha_n)^3(1+L_*)\lambda_{n+1}^2\mu^2\|F(T^n x_n)\|^2 \\
 &+ (1-\alpha_n)(1+L_*)\lambda_{n+1}\mu[\|x_n-x^*\|^2+\|F(T^n x_n)\|^2] \\
 &+ 2(1-\alpha_n)^2\lambda_{n+1}^2\mu^2\|F(T^n x_n)\|^2 \\
 = &\|x_n-x^*\|^2-(1-\alpha_n)(1-k)\|x_{n+1}-T^n x_{n+1}\|^2 \\
 &+ (1-\alpha_n)(k_n-1)(1+L_*)^2\|x_n-x^*\|^2 \\
 &+ (1-\alpha_n)^2(k_n-1)(1+L_*)\lambda_{n+1}\mu\|x_n-x^*\|^2 \\
 &+ (1-\alpha_n)^2(k_n-1)(1+L_*)\lambda_{n+1}\mu\|F(T^n x_n)\|^2 \\
 &+ (1-\alpha_n)^3(k_n-1)\lambda_{n+1}^2\mu^2\|F(T^n x_n)\|^2 \\
 &+ 2(1-\alpha_n)^2(1+L_*)^3\|x_n-x^*\|^2 \\
 &+ [(1-\alpha_n)^2(1+L_*)^2(2-\alpha_n)\lambda_{n+1}\mu\|F(T^n x_n)\|^2 \\
 &+ [(1-\alpha_n)^2(1+L_*)^2(2-\alpha_n)\lambda_{n+1}\mu\|x_n-x^*\|^2 \\
 &\quad + 2(1-\alpha_n)^3(1+L_*)\lambda_{n+1}^2\mu^2\|F(T^n x_n)\|^2 \\
 &+ (1-\alpha_n)(1+L_*)\lambda_{n+1}\mu\|x_n-x^*\|^2 \\
 &+ (1-\alpha_n)(1+L_*)\lambda_{n+1}\mu\|F(T^n x_n)\|^2 \\
 &+ 2(1-\alpha_n)^2\lambda_{n+1}^2\mu^2\|F(T^n x_n)\|^2 \tag{1.14}
 \end{aligned}$$

Observe that $\|F(T^n x_n)\| \leq LL_* \|x_n - x^*\| + \|F(x^*)\|$,

and hence

$$\|F(T^n x_n)\|^2 \leq 2(L^2 L_*^2 \|x_n - x^*\|^2 + \|F(x^*)\|^2) \tag{1.15}$$

Substituting (1.15) into (1.14) yields

$$\begin{aligned}
 \|x_{n+1}-x^*\|^2 \leq &\{1+(1-\alpha_n)(k_n-1)(1+L_*)^2+(1-\alpha_n)^2(k_n-1)(1+L_*)\lambda_{n+1}\mu \\
 &+ 2(1-\alpha_n)^2(1+L_*)^3+[(1-\alpha_n)^2(1+L_*)^2(2-\alpha_n)\lambda_{n+1}\mu \\
 &+ (1-\alpha_n)(1+L_*)\lambda_{n+1}\mu\}\|x_n-x^*\|^2 - (1-\alpha_n)(1-k)\|x_{n+1}-T^n x_{n+1}\|^2 \\
 &+ \{(1-\alpha_n)^2(k_n-1)(1+L_*)\lambda_{n+1}\mu+(1-\alpha_n)^3(k_n-1)\lambda_{n+1}^2\mu^2 \\
 &+ [(1-\alpha_n)^2(1+L_*)^2(2-\alpha_n)\lambda_{n+1}\mu \\
 &+ 2(1-\alpha_n)^3(1+L_*)\lambda_{n+1}^2\mu^2 \\
 &+ (1-\alpha_n)(1+L_*)\lambda_{n+1}\mu \\
 &+ 2(1-\alpha_n)^2\lambda_{n+1}^2\mu^2\} \times [2L^2 L_*^2 \|x_n-x^*\|^2 + 2\|F(x^*)\|^2]
 \end{aligned}$$

$$\begin{aligned}
 &\leq \{[1+(1-\alpha_n)(k_n-1)(1+L_*)^2 + (1-\alpha_n)^2(k_n-1)(1+L_*)\lambda_{n+1}\mu \\
 &+ 2(1-\alpha_n)^2(1+L_*)^3 + ((1-\alpha_n)^2(1+L_*)^2)(2-\alpha_n)\lambda_{n+1}\mu \\
 &+ (1-\alpha_n)(1+L_*)\lambda_{n+1}\mu] + 2L^2L_*^2[(1-\alpha_n)^2(k_n-1)(1+L_*)\lambda_{n+1}\mu \\
 &+ (1-\alpha_n)^3(k_n-1)\lambda_{n+1}^2\mu^2 + ((1-\alpha_n)^2(1+L_*)^2)(2-\alpha_n)\lambda_{n+1}\mu \\
 &+ 2(1-\alpha_n)^3(1+L_*)\lambda_{n+1}^2\mu^2 + (1-\alpha_n)(1+L_*)\lambda_{n+1}\mu \\
 &+ 2(1-\alpha_n)^2\lambda_{n+1}^2\mu^2]\} \|x_n - x^*\|^2 \\
 &\quad - (1-\alpha_n)(1-k) \|x_{n+1} - T^n x_{n+1}\|^2 \\
 &+ 2\{(1-\alpha_n)^2(k_n-1)(1+L_*)\lambda_{n+1}\mu + (1-\alpha_n)^3(k_n-1)\lambda_{n+1}^2\mu^2 \\
 &+ [(1-\alpha_n)^2(1+L_*)^2](2-\alpha_n)\lambda_{n+1}\mu \\
 &+ 2(1-\alpha_n)^3(1+L_*)\lambda_{n+1}^2\mu^2 + (1-\alpha_n)(1+L_*)\lambda_{n+1}\mu \\
 &+ 2(1-\alpha_n)^2\lambda_{n+1}^2\mu^2\} \|F(x^*)\|^2 \\
 &= [1 + a_n] \|x_n - x^*\|^2 - (1-\alpha_n)(1-k) \|x_{n+1} - T^n x_{n+1}\|^2 + b_n, \quad (1.16)
 \end{aligned}$$

where,

$$\begin{aligned}
 a_n = & (1-\alpha_n)(k_n-1)(1+L_*)^2 + (1-\alpha_n)^2(k_n-1)(1+L_*)\lambda_{n+1}\mu \\
 & + 2(1-\alpha_n)^2(1+L_*)^3 + ((1-\alpha_n)^2(1+L_*)^2)(2-\alpha_n)\lambda_{n+1}\mu \\
 & + (1-\alpha_n)(1+L_*)\lambda_{n+1}\mu + 2L^2L_*^2[(1-\alpha_n)^2(k_n-1)(1+L_*)\lambda_{n+1}\mu \\
 & + (1-\alpha_n)^3(k_n-1)\lambda_{n+1}^2\mu^2 + ((1-\alpha_n)^2(1+L_*)^2)(2-\alpha_n)\lambda_{n+1}\mu \\
 & + 2(1-\alpha_n)^3(1+L_*)\lambda_{n+1}^2\mu^2 + (1-\alpha_n)(1+L_*)\lambda_{n+1}\mu \\
 & + 2(1-\alpha_n)^2\lambda_{n+1}^2\mu^2],
 \end{aligned}$$

and,

$$\begin{aligned}
 b_n = & 2\{(1-\alpha_n)^2(k_n-1)(1+L_*)\lambda_{n+1}\mu + (1-\alpha_n)^3(k_n-1)\lambda_{n+1}^2\mu^2 \\
 & + [(1-\alpha_n)^2(1+L_*)^2](2-\alpha_n)\lambda_{n+1}\mu \\
 & + 2(1-\alpha_n)^3(1+L_*)\lambda_{n+1}^2\mu^2 + (1-\alpha_n)(1+L_*)\lambda_{n+1}\mu \\
 & + 2(1-\alpha_n)^2\lambda_{n+1}^2\mu^2\}.
 \end{aligned}$$

Conditions (ii), (iii) and $\sum_{n=1}^\infty (k_n - 1) < \infty$ of our Theorem 3.2 imply that $\sum_{n=1}^\infty a_n < \infty$ and $\sum_{n=1}^\infty b_n < \infty$. It now follows from Lemma 2.2 and equation (1.16) that $\lim_{n \rightarrow \infty} \|x_n - x^*\|$ exists and

this completes the proof of (a).

Since $\{\|x_n - x^*\|^2\}$ is bounded, there exists $M > 0$ such that $\|x_n - x^*\|^2 \leq M$ for all $n \geq 1$. Thus it follows from (1.16) that

$$\|x_{n+1} - x^*\|^2 \leq \|x_n - x^*\|^2 - (1-\alpha_n)(1-k) \|x_{n+1} - T^n x_{n+1}\|^2 + \sigma_n \quad (1.17)$$

where $\sigma_n = b_n + Ma_n$, $n \geq 1$.

We prove that $\liminf_{n \rightarrow \infty} \|x_{n+1} - T^n x_{n+1}\| = 0$. If $\liminf_{n \rightarrow \infty} \|x_{n+1} - T^n x_{n+1}\| = \delta > 0$. Then \exists a positive

integer N such that $\|x_{n+1} - T^n x_{n+1}\| \geq \frac{\delta}{2} \forall n \geq N$. It follows from (1.17) that

$$(1-k) \frac{\delta}{2} \sum_{j=N}^n (1-\alpha_j) \leq \|x_N - x^*\|^2 + \sum_{j=N}^n \sigma_j \quad (1.18)$$

Since, $\sum_{n=1}^\infty \sigma_n < \infty$, it follows from (1.18) that $\sum_{n=1}^\infty (1-\alpha_n) < \infty$, contradicting condition (i) of our Theorem 3.2.

Observe that

$$\begin{aligned}
 \|x_n - T^n x_n\| &\leq \|x_n - x_{n+1}\| + \|x_{n+1} - T^n x_{n+1}\| + \|T^n x_{n+1} - T^n x_n\| \\
 &\leq (1 + L_*) \|x_{n+1} - x_n\| + \|x_{n+1} - T^n x_{n+1}\| \\
 &= (1 + L_*) \|(1 - \alpha_n)[T^n x_n - x_n - \lambda_{n+1} \mu F(T^n x_n)]\| \\
 &\quad + \|x_{n+1} - T^n x_{n+1}\| \\
 &\leq (1 + L_*)(1 - \alpha_n)[\|T^n x_n - x_n\| + \lambda_{n+1} \mu \|F(T^n x_n)\|] \\
 &\quad + \|x_{n+1} - T^n x_{n+1}\| \\
 &\leq (1 + L_*)(1 - \alpha_n)[(1 + L_*) \|x_n - x^*\| \\
 &\quad + \lambda_{n+1} \mu (LL_* \|x_n - x^*\| + \|F(x^*)\|)], \\
 &\quad + \|x_{n+1} - T^n x_{n+1}\| \tag{1.19}
 \end{aligned}$$

Since $\{\|x_n - x^*\|\}$ is bounded, $\lim_n(1 - \alpha_n) = 0$, and $\liminf_n \|x_{n+1} - T^n x_{n+1}\| = 0$, then it follows from (1.19) that

$$\liminf_n \|x_n - T^n x_n\| = 0.$$

It now follows as in the proof of Theorem 3.1 (see page 6) that

$$\liminf_n \|x_n - Tx_n\| = 0.$$

If $\{x_n\}_{n=1}^\infty$ converges strongly to a fixed point p of T , then $\lim_{n \rightarrow \infty} \|x_n - p\| = 0$. Since

$$0 \leq d(x_n, F(T)) \leq \|x_n - p\|,$$

we have $\liminf_{n \rightarrow \infty} d(x_n, F(T)) = 0$.

Conversely, suppose $\liminf_{n \rightarrow \infty} d(x_n, F(T)) = 0$, then it follows from Lemma 2.2 and (1.18) that

$\lim_{n \rightarrow \infty} d(x_n, F(T)) = 0$. Thus for arbitrary $\varepsilon > 0$, there exists a positive integer N_1 such that

$d(x_n, F(T)) < \frac{\varepsilon}{4}$, $\forall n \geq N_1$. Furthermore, $\sum_{n=1}^\infty \sigma_n < \infty$ implies that there exists a positive integer

N_2 such that $\sum_{j=n}^\infty \sigma_j < \frac{\varepsilon^2}{16}$, $\forall n \geq N_2$. Choose $N = \max\{N_1, N_2\}$, then $d(x_N, F(T)) < \frac{\varepsilon}{4}$ and

$\sum_{j=N}^\infty \sigma_j < \frac{\varepsilon^2}{16}$. It follows from (1.16) that for all $n, m \geq N$ and for all $p \in F(T)$ we have

$$\begin{aligned}
 \|x_n - x_m\|^2 &\leq [\|x_n - p\| + \|x_m - p\|]^2 \\
 &\leq 2[\|x_n - p\|^2 + \|x_m - p\|^2] \\
 &\leq 2[\|x_N - p\|^2 + \sum_{j=N+1}^n \sigma_j + \|x_N - p\|^2 + \sum_{j=N+1}^m \sigma_j] \\
 &\leq 4\|x_N - p\|^2 + 4\sum_{j=N}^\infty \sigma_j \quad \forall n, m \geq N
 \end{aligned}$$

Thus

$$\|x_n - x_m\| \leq 2\|x_N - p\| + 2\left(\sum_{j=N}^\infty \sigma_j\right)^{\frac{1}{2}}$$

Taking infimum over all $p \in F(T)$, we obtain

$$\|x_n - x_m\| \leq 2d(x_N, F(T)) + 2\left(\sum_{j=N}^\infty \sigma_j\right)^{\frac{1}{2}} < \varepsilon, \quad \forall n, m \geq N.$$

Thus $\{x_n\}_{n=1}^\infty$ is Cauchy. Suppose $\lim_{n \rightarrow \infty} x_n = u$, then since $\lim_{n \rightarrow \infty} \|x_n - Tx_n\| = 0$, we have $u \in F(T)$.

This completes the proof of Theorem 3.2. \uparrow

Remark 3.3. Prototype for our real sequences $\{\alpha_n\}$ and $\{\lambda_n\}$ in our Theorem 3.2 are:

$$\alpha_n = \frac{n}{n+1}, \quad n \geq 1; \quad \text{and} \quad \lambda_n = \frac{1}{(n+1)^2}, \quad n \geq 1.$$

Remark 3.4 Let K be a nonempty closed convex subset of a real Hilbert space H and $T : K \rightarrow K$ a k -strictly asymptotically pseudocontractive map. Let $F : H \rightarrow H$ be an L -Lipschitzian mapping and let $P_K : H \rightarrow K$ be the proximity map defined for each $x \in H$ by

$P_K(x) = x^* \in K \ni \|x - x^*\| = \inf\{\|x - y\| : y \in K\}$. Then we can obtain results similar to the results in Theorem 3.1 using the iterative sequence $\{x_n\}_{n=1}^\infty$ generated from an arbitrary $x_1 \in H$ by

$$x_{n+1} = \alpha_n x_n + (1 - \alpha_n) P_K T^{\lambda_{n+1}} x_n, \quad n \geq 1,$$

where $T^{\lambda_{n+1}} x_n := T^n x_n - \lambda_{n+1} \mu F(T^n x_n)$.

Remark 3.5 The hybrid iteration method studied above is very useful for solving variational inequality problem of the form:

$VIP(F, F(T))$: find $u^* \in F(T) \ni \langle F(u^*), v - u^* \rangle \geq 0 \quad \forall v \in F(T)$ (see for example ([19],[20]).

We shall explore this important application in our subsequent work.

Acknowledgment.

The authors are grateful to the referees for their useful comments and suggestions.

References

- [1] F.E. Browder and W.V. Petryshyn, Construction of fixed points of nonlinear mappings in Hilbert spaces, *J. Math. Anal. Appl.*, **20(2)** (1967), 197-228
- [2] I. S. Ishikawa, Fixed Points by New Iteration Methods, *Proc. Amer. Math. Soc.*, **44** (1974), 147-150.
- [3] Genaro Lopez Acedo and Hong-Kun Xu, Iterative methods for strict pseudocontractions in Hilbert spaces, *Nonlinear Analysis*, **67(7)** (2007), 2258-2271.
- [4] Giuseppe Marino and Hong-Kun Xu, weak and strong convergence theorems for strictly pseudocontractions in Hilbert spaces, *J. Math. Anal. Appl.* **329(1)** (2007), 336-346.
- [5] Z. Opial, Weak convergence of successive approximations for nonexpansive mappings, *Bull. Amer. Math. Soc.* **73** (1967), 591-597. V
- [6] M. O. Osilike, Iterative Approximations of Fixed Points of Asymptotically Demicontractive Mappings, *Indian J. Pure Appl. Math.*, **29(12)** (1998), 1291-1300.
- [10] M.O. Osilike and S.C. Aniagbosor, Weak and strong convergence theorems for fixed points of asymptotically nonexpansive mappings, *Mathematical and Computer Modelling* **32** (2000) 1181-1191.
- [8] M.O. Osilike, S.C. Aniagbosor and B.G. Akuchu, Fixed Points of Asymptotically Demicontractive Mappings in Arbitrary Banach Spaces, *PanAmerican Mathematical Journal*, **12(2)**, (2002), 77-88.
- [9] M.O. Osilike and A. Udomene, Demiclosedness Principle and Convergence Results for Strictly Pseudocontractive Mappings of Browder-Petryshyn Type, *J. Math. Anal. Appl.* **256** (2001), 431-445.
- [10] M.O. Osilike and A. Udomene, D.I. Igbokwe and B.G. Akuchu, Demiclosedness Principle and Convergence Theorems for k - Asymptotically Strictly Pseudocontractive Maps *J. Math. Anal. Appl.* **326** (2007), 1334-1345.
- [11] M. O. Osilike, F. O. Isiogugu, and P. U. Nwokoro, Hybrid iteration method for fixed points of k – Strictly Pseudocontractive Mappings in Arbitrary Banach spaces, *Journal of Nigerian Mathematical Society* **Vol 27**, 91-108 2008.
- [12] M.O. Osilike and Y. Shehu, Cyclic algorithm for common fixed points of finite family of strictly pseudocontractive mappings of Browder-Petryshyn type, *Nonlinear Analysis: Theory, Methods & Applications* **70 (10)** (2009), 3575-3583.
- [13] M.O. Osilike and Y. Shehu, Explicit averaging cyclic algorithm for common fixed points of a finite family of asymptotically pseudocontractive maps in

- Banach spaces, *Computers & Mathematics with Applications* **57 (9)** (2009), 1502-1510.
- [4] M.O. Osilike and Y. Shehu, Explicit averaging cyclic algorithm for common fixed points of asymptotically strictly pseudocontractive maps, *Applied Mathematics & Computation* **213 (2)** (2009), 548-553.
- [15] B. E. Rhoades, Comments on two fixed point iteration methods, *J. Math. . Anal. App.*, **56** (1976), 741-750. *Anal. Appl.* **256** (2001), 431-445.
- [16] B.E. Rhoades, Fixed point iterations using infinite matrices, *Trans. Amer. Math. Soc.* **196** (1974), 161-176.
- [17] L. Qihou, Convergence Theorems of the Sequence of Iterates for Asymptotically Demicontractive and Hemicontractive Mappings, *Nonlinear Analysis*, **26(11)** (1996),1835-1842. *J. Math.*
- [18] Lin Wang, An iterative method for nonexpansive mappings in Hilbert spaces, *Fixed Point Theory and Applications* **Vol 2007** Article ID 28619 (2007) 1-8, <http://www.hindawi.com/journal/fpta/index.html>
- [19] H.K. Xu and T.H. Kim, Convergence of hybrid steepest-descent methods for variational inequalities, *J. Optimiz. Theory and Appl.* **119(1)** (2003) 185-201.
- [20] I. Yamada, The hybrid steepest descent method for the variational inequality problem over the intersection of fixed point sets of nonexpansive mappings, in *Inherently Parallel Algorithms in Feasibility and Optimization and their Applications Haifa (2000)* D. Butnariu, Y. Censor, and S. Reich, Eds., Vol 8 of *Stud. Comput. Math.*, pp. 473-504, North-Holland, Amsterdam, The Netherlands, (2001).

Department of Mathematics, University of Nigeria, Nsukka, Nigeria
Email: peter.nwokoro@unn.edu.ng

Department of Mathematics, University of Nigeria, Nsukka, Nigeria
Email: micah.osilike@unn.edu.ng

Monte Carlo Simulations of Energy Surface and Conformation of Complex Systems

Samson O. Aisida^{*1} and Chibuikwe D. Umeh²

^{1,2} Department of Physics and Astronomy, University of Nigeria Nsukka

*Corresponding author: E-mail: samson.aisida@unn.edu.ng

Abstract

The energy surfaces of complex systems such as spin glass and proteins are characterized by a large number of local minima and few global minima which correspond to many slightly different conformations that a complex system can assume. This complex energy landscape which specifies the dynamic and the conformation of the system have been described by highly frustrated interactions between components in the systems. In order to obtain the energy surface of these systems, we use Monte Carlo simulation techniques based on Markov chains which are very effective and distinct among many approaches to describe the behaviour of complex systems. We demonstrate our approach through Ising spin glasses and lattice protein model. In the Edwards-Anderson spin glass, we are able to produce the thermodynamic results of the densities of states for magnetization, specific heat and magnetic susceptibility using metropolis-biased Monte Carlo simulation. In hydrophobic-polar (HP) lattice model, we put forward a move-biased Monte Carlo simulation (MBMC) method based on self-avoiding walk in combination with the neighborhood (diagonal-pull) moves search strategy on the 2D square lattice on a set of benchmark protein sequences which produce optimal conformations with compact hydrophobic core surrounded by polar residues when compared with the state-of-the-art local search algorithm for protein structure prediction.

Keywords: Energy landscape, Ising model, Lattice Protein, Monte Carlo, H-P model

INTRODUCTION

Complex systems can be categorized broadly into passive (e.g. Glasses, Ising spin glass and spin glasses) and active (e.g. Protein)[1] systems. The energy surface of a complex system such as glass, spin glass and proteins show very large number of minima which correspond to many slightly different conformations that a complex system can assume. The complex energy landscape of these systems which specify their conformation and dynamic has long been a subject of discussion by many authors in different fields of science. These complex systems have been described by highly frustrated interactions between components in the systems. The most commonly studied frustrated passive is "Ising spin glass" while in the case of active it is "Protein"[2,3,4]. The Ising spin model is a simple and standard model of statistical physics that has a phase transition between a ferromagnetic and paramagnetic state and typical models to investigate the rough energy landscape of frustrated systems. The model in 2D has been solved to show a phase transition at the critical temperature by Onsager [5]. According to Wust et al. and Iveta et al. [3, 6] Ising spin glass is a disordered magnetic system with frustration and is quite challenging using local methods, both in statistical mechanics and computer simulation; because its free energy landscape is quite complicated with nontrivial properties and demands a lot of time with freezing transition at low temperature. As a result of this, Monte Carlo (MC) simulation with Metropolis algorithm has been viable to circumvent this challenge. The other extended MC methods are: Multicanonical Monte Carlo sampling [7] which preweights the evolution of the MC Markov chain in order to sample the interface configuration, cluster algorithm [8,9], Wang-Landau sampling [10] which is very potent in computing the density of state, Parallel tempering MC method [8] where multiple systems are simulated simultaneously at different temperature, simulated annealing algorithm (SA)[11], and replica exchange Monte Carlo method (REMC) [12].

Proteins on the other hand, which borrowed some concepts and techniques from physics of spin glass field are viewed as a system with minimal frustration in its native conformation. It exhibits similar complexity with spin glass for which many different folding configurations may have almost the same

energy. Also, the concept of two-state transitions (conformational transition) from unfolded (denatured) state to the folded (Native) state [13] is synonymous to spin glass phase transition [14]. There are two remarkable problems in the study of proteins. The first one is protein folding problem which is how the 20 natural amino acid monomers coupled with other physiological conditions ended up spontaneously in a unique tertiary structure [2,3,15,16,17,18]. The second problem is protein design (inverse of protein folding) i.e. finding the amino acid sequence from a given protein conformation which is stable and fold fast in the target conformation. These two problems have triggered the effort of many researchers experimentally and computationally in the past 20 decades [18,19,20,21]. The main goal of this paper is to use heuristic approaches to study the energy surface of complex systems via Ising spin glass and Hydrophobic-polar lattice model. The rest of the paper is organized as follows. In section 2, we describe the method used. In section 3, we describe the energy surface in an Ising spin glass and lattice protein model with the results of our simulation. A conclusion is given in section 4.

2.0 Methodology

2.1 The Ising Model

In the Ising model, the Metropolis algorithm starts with an arbitrary spin configuration to generate a new one (trial) and then calculate the energy. If the energy of the trial is less than or equal to the old, we accept the trial, but if the energy of the trial is greater than the old, we accept with probability $P = \exp(-\Delta E / KT)$ which depends on the random number $0 \leq r \leq 1$, where K is the Boltzmann constant, T is the temperature and ΔE is the change in energy.

2.2 The HP Model

In HP model, we put forward a move-biased Monte Carlo simulation (MBMC) method and the neighborhood search strategy (diagonal-pull moves) in our algorithm. Stochastic Local search algorithm according to Shatabda and Cebrian [22,23], is known for its effectiveness with quality solutions. It starts from an initial conformation and moves from one conformation to another to find a better conformation. Stochastic sampling like Monte Carlo method driven by random numbers and probability statistic is a veritable tool to sample conformational space when it is infeasible or impossible to compute an exact result with a deterministic algorithm [24,25]. Our approach involves the simulation of a protein conformation as a self-avoiding walk (SAW) on a square lattice to model the folding process; we vary the probabilities of the four possible directions (North, west, south and east) along which a self-avoiding walker may move. The procedures are as follows

The adopted method generates an initial conformation ' ξ ' following a SAW on square lattice points. It places the first amino acid at (0, 0) followed by a random selection of a basis vector to place the amino acid at a neighboring free lattice point. The mapping proceeds until a SAW is found in the whole protein sequence.

We compute the energy $\Psi(\xi)$ as a SAW on square lattice point for each conformation using equation 3.3.

We let $i = 1$

We execute coupled (diagonal-pull) moves for all legal move positions of the i th amino acid of the current conformation ξ . If the coupled move is executed successfully, we compute the energies of the corresponding legal conformations obtained by coupled moves and pick out the conformation with the lowest energy as a newly updated conformation of, ξ expressed as ξ^*

We compute $\Psi(\xi^*)$

If the $\Psi(\xi^*) < \Psi(\xi)$, then let $\xi = \xi^*$, $\Psi(\xi) = \Psi(\xi^*)$ and go to the last procedure; otherwise go to (7)

If $(0 \leq \mathfrak{R} \leq 1) < \exp\{[\Psi(\xi) - \Psi(\xi^*)] / k_B T\}$, where $\mathfrak{R}(0,1)$ denotes a random number between 0 and 1, then we let $\xi = \xi^*$, $\Psi(\xi) = \Psi(\xi^*)$, and go to (9); otherwise we go to (8)

From the current conformation ξ , we produce the new conformation ξ^* by coupled move search strategy. If ξ^* is a legal conformation, then we update the current conformation ξ with, ξ^* , i.e we let $\xi = \xi^*$ and $\Psi(\xi) = \Psi(\xi^*)$
 Stop if the move is ergodic; otherwise we go to step (2)

3.0 Results and Discussion

3.1 Ising Spin Glass

The study of spin glasses is an active and controversial area of statistical Physics. In particular the properties of these systems at zero temperature have been intensively studied in the last years. The problem of finding the ground states (G Ss) is a very difficult subject because of the quenched disorder and frustration that are present in most realistic spin glass models [26]. A simple spin glass model is the Edwards- Anderson model which consists of a set of N Ising spins $\zeta_i = \pm 1$ placed in a square or cubic lattice of linear dimension L, with periodic boundary conditions in all directions. Its Hamiltonian for 2D is

$$H = -\sum_{\langle i,j \rangle} J_{ij} \zeta_i \zeta_j - E \sum_i \zeta_i \tag{3.1}$$

Where $\langle i, j \rangle$ indicates a sum over nearest neighbors. The coupling constants between nearest neighbor followed a bimodal distribution, i.e., $J_{ij} = \pm 1$, with equal probability, E is an external magnetic field. For simplicity, we take $E = 0$. For relatively large system sizes, and due to the fact that the coupling constant is the independent variables, only configurations with half of the bonds of each sign are statistically significant. To preserve this feature for small sizes, we explicitly enforce the constraint

$$\sum_{i,j} J_{ij} = \begin{cases} 0 & \text{for even number of bonds} \\ \pm 1 & \text{for odd number of bonds} \end{cases} \tag{3.2}$$

For systems with an odd number of bonds, we enforce the constraint $\sum_{\langle i,j \rangle} J_{ij} = 1$ for the half of the samples and $\sum_{\langle i,j \rangle} J_{ij} = -1$, for the other half.

At high temperature, we expect a random assortment of spin and so a vanishing magnetization, while at low temperature it is expected to approach N/2 as all the spin get aligned.

$$M = \sum_{i=1}^N \zeta_i \tag{3.3}$$

The specific heat energy (C) is obtained by knowing the fluctuation in energy (U) occurring during a number of simulation calculated as:

$$C_v = 1/T^2 [\langle H^2 \rangle - \langle H \rangle^2] \tag{3.4}$$

The magnetic susceptibility (χ) gives the information about how much the magnetization changes by increasing the temperature

$$\chi = 1/T [\langle M^2 \rangle - \langle M \rangle^2] \tag{3.5}$$

The magnetic moments of the ferromagnetic materials domains are aligned along the direction of the applied magnetic field with equal magnitude resulting in a large net magnetic moment. Their crystalline structures allow for direct coupling interactions between the moments, which may strongly enhance the flux density. The materials are composed of domains, each containing large numbers of

atoms whose magnetic moments are parallel producing a net magnetic moment of the domain that points in the same direction due to unpaired electrons which still retain its magnetization after the external magnetic field has been removed (spontaneous magnetization) as a result of the residual magnetic moment. Any materials that retain permanent magnetization in the absence of an externally applied magnetic field are known as hard magnets. Good examples are: iron, nickel and cobalt [27, 28]. The magnetic moments of the atoms of a paramagnetic material are align along the direction of the applied magnetic field resulting to a weak net magnetic moment and small positive magnetic susceptibility ($\chi \approx 0$). This material has magnetic moment with no long-range order because above the *Ne'el* temperature, thermal energy is sufficient to cause the equal and oppositely aligned atomic moments to randomly fluctuate, leading to a disappearance of their long-range order. The atom of the materials has a net magnetic moment due to unpaired electrons, but magnetic domains are absent, a sequel to this, the material does not retain magnetic moment at the removal of the externally applied magnetic field. Good examples are: lithium, magnesium, gadolinium, tantalum and pyrite [27, 28,29,30]. In diamagnetic, the atom of the materials has a zero net magnetic moment and negative susceptibility ($\chi < 0$) due to the nonexistence of the unpaired electrons. Also, as a result of their weak response against the applied magnetic field (repel an applied magnetic field), the material does not retain the magnetic moment when the externally applied magnetic field is removed. Good examples are: silver, gold, copper, quartz and SiO_2 [27,28]. The magnetization was determined as shown in figure 1a, since at critical temperature the spontaneous magnetization vanishes, but above $T = 2.60$ of zero field the magnetization rapidly decreases. Below this temperature, the system is in a ferromagnetic state and above it, is in a paramagnetic state of the 2D Ising model. The specific heat as shown in figure 1b shows how much the energy changes with increasing temperature. Also, the magnetic susceptibility as shown in figure 1c shows that below and above the critical temperature (T_c) the magnetic susceptibility is about zero and around T_c it goes to infinity [31].

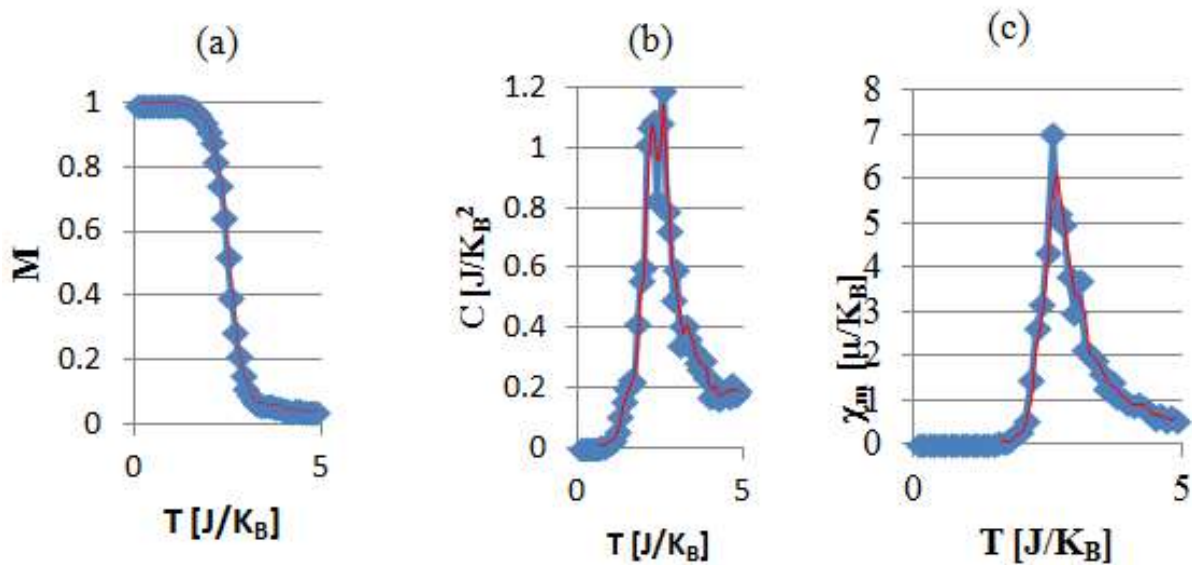


Figure 1: (a)Magnetization(b) Specific Heat and (c) Magnetic Susceptibility at zero fields for 2D Ising model

3.2 HP Lattice Protein Model

Currently, the investigation of the folding process of real proteins via full simulation or deterministic approaches is not feasible. Consequently, a stochastic heuristic lattice protein model which abstract from real protein and has the ability to extract minimal energy conformations efficiently has come to a full-fledged stage to address this complexity [3,32]. Lattice models have proven to be extremely useful tools to address the complexity of the protein structure prediction problem (PSP) that has been proven to be NP-complete by many authors [33,34,35]. This model can be used to extract essential principles, make predictions and harmonize our understanding of many different properties of proteins. Istrail et al. [36], classified Lattice models into two types: The first type is “designed to

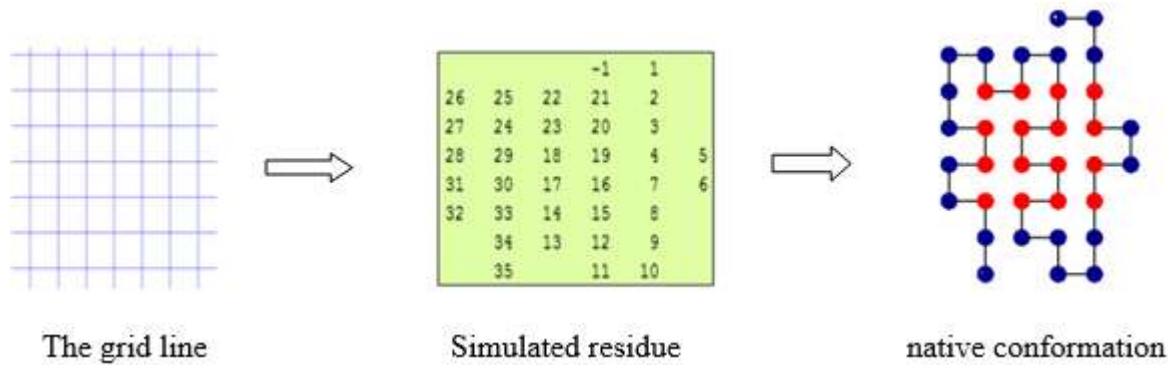


Figure 4. (Color online) The grid line coupled with the simulated residues gives the native conformation for $N = 36$, (PPPHPPHPPPPPPHHHHHHHPPHPPPPHPPHPP) is equivalent to (-1,1,1,2,3,4,5,6,7,8,9,10,11,12,13,14,15,16,17,18,19,20,21,22,23,24,25,26,27,28,29,30,31,32,33,34,35) where (3,4,7,8,14,15,16,17,18,19,20,23,24,29,30,33) are hydrophobic and (-1,1,2,5,6,9,10,11,12,13,21,22,25,26,27,28,31,32) are polar residues. The ground state energy is -14. The blue and red circles are the polar and the hydrophobic residues, respectively, while -1 is the starting point.

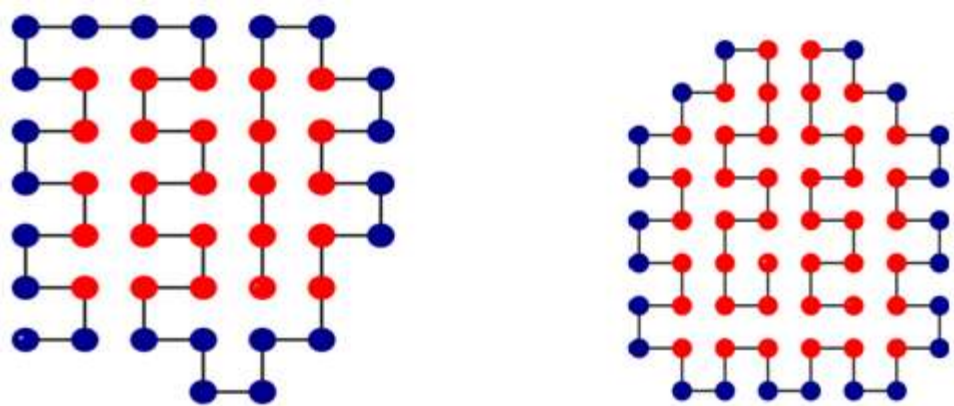


Figure 5. (Color online) the native conformation for $N = 48$ and 64 . The ground state energy is -23 and -42 respectively. The blue and red circles are the polar and the hydrophobic residues respectively while -1 is the starting point.

Figures 3 and 4 described how the simulated residues are embedded in the lattice grid to obtain the native conformation. The conformations in figures 3, 4 and 5 are the ground state (native) conformations obtained by MBMC for the instances considered. It is obvious that each of these conformations possesses a compact hydrophobic core surrounded by polar residues. The results obtained compared to other methods using 2-D as shown in table 1 indicate that MBMC is competitive with the Conventional Monte Carlo (CMC), Genetic algorithm (GA), Evolutionary Monte Carlo (EMC) and Ant colony Optimization (ACO) methods described in the literature. And even outperform them at the highest sequence with the lowest energy value.

4.0 Conclusion

Ising spin glass, and HP lattice model are in the forefront of computational physics of system with Complex energy landscapes. We have demonstrated using Monte Carlo (MC) simulation method which is very distinct among many methods like Wang-Landau sampling, parallel tempering and multicanonical sampling for complex systems. Firstly, we used Metropolis MC Simulation to obtain the thermodynamic properties with Ising model and secondly we used move-biased MC simulation with HP lattice protein model based on self-avoiding walk using diagonal-pull moves on the 2D square lattice to obtain optimal protein conformations that obey thermodynamic and kinetics hypothesis.

References

- [1] William, M. J., & Shakhnovich, E. I. (2016). Structure-Based Prediction of Protein-Folding Transition Paths. *Biophysical Journal*, *111*, 925–936.
- [2] Takeshi, K. (2009). Spin correlations in a non-frustrated one-dimensional spin system, and formation of the ground state as a model of protein folding. *Physica A*, *388*, 129-136.
- [3] Wust, T., Landau, D., Gervais, C., & Xu, Y. (2009). Monte Carlo simulations of systems with complex energy landscapes. *Computer Physics Communication*, *180*, 475-479.
- [4] Hans, F. (2010). *An Introduction to Biological Physics and Molecular Biophysics*. (C. S. Shirley, & C. S. Winnie, Eds.) New York: Springer.
- [5] Onsager, L. (1944). Crystal statistic. I. A two-dimensional model with an order-disorder transition. *Phys. Rev.*, *65*, 117-149.
- [6] Iveta, R., Pimentel, C., & De, D. (2015). Spin Glass Field Theory with Replica Fourier Transforms. *Physics Procedia*, *75*, 802–812.
- [7] Berg, B. A., & Neuhaus, T. (1991). Multicanonical algorithms for first order phase transitions. *Phys. Lett. B*, *267*, 249-253.
- [8] Swendsen, R., & Wang, J. (1987). Nonuniversal critical dynamics in Monte Carlo simulations. *Phys. Rev.Lett.*, *58*, 86-88.
- [9] Wolff, U. (1989). Collective Monte Carlo updating for spin systems. *Phy. Rev. Lett.*, *62*, 361-364.
- [10] Wang, F., & Landau, D. (2001). Efficient, multiple-range random walk algorithm to calculate the density of states. *Phys. Rev. Lett.*, *86*, 2050-2053.
- [11] Albrecht, A. A., Skaliotis, A., & Steinhofel, K. (2008). Stochastic Protein folding Simulation in three-dimensional HP-model. *Comput. Biol. Chem.*, *32*, 248-255.
- [12] Thachuk, C., Shmygelska, A., & Hoos, H. H. (2007). A replica exchange MOnTe Carlo algorithm for protein folding in the HP model. *BMC Bioinformatics*, *8*, 342-361.
- [13] Marek, C., & Jayanth, B. R. (2013). Energy landscape and dynamics of proteins: An exact analysis of a simplified lattice model. *Physical Review E*, *88*, 040702(R).
- [14] Millership, C., Phillips, J., & Main, E. (2016). Ising Model Reprogramming of a Repeat Protein's Equilibrium Unfolding Pathway. *J Mol Biol*, *428*, 1804–1817.
- [15] Bryan, A. K. (2002). *Protein folding: new methods unveil rate-limiting structures*. Chigago: Ph.D Thesis, University of Chicago.
- [16] Kerson, H. (2005). *Lectures on Statistical Physics and Protein Folding*. Singapore: World Scientific Publishing Co. Pte. Ltd.
- [17] Erik, S. (2000). *Thermodynamics of protein folding and design*. Lund, Sweden: Ph. D. Thesis, Lund University.
- [18] Seyed, M. N., Mehdi, M., Lan, Z., Jianhua, Z. H., & Xin, G. (2017). Protein Structure Classification and Loop Modeling Using Multiple Ramachandran Distributions. *Computational and Structural Biotechnology Journal*. Retrieved from <http://dx.doi.org/10.1016/j.csbj.2017.01.011>
- [19] Broglia, R. A., & Tiana, G. (2003). Physical Models for Protein Folding and Drug Design. *Proc. Idea-Finding Symposium* Germany: Frankfurt Institute for Advanced Studies, 23-33.
- [20] Irbach, A., & Sandelin, E. (1999). Monte Carlo Study of the Phase Structure of Compact Polymer Chains. *Journal of Chemical Physics*, *110*, 12256-12262.
- [21] Seno, F., Vendruscolo, M., Maritan, A., & Banaver, J. R. (1996). An Optimal Protein Design Procedure. *Phys. Rev. Lett.*, *77*, 1901-1904.
- [22] Shatabda, S., Newton, M., Pham, D., & Sattar, A. (2012). Memorybased local search for simplified protein structure prediction. *In proceedings of the ACM Conference on Bioinformatics, Computational Biology and Biomedicine. ACM*, *1*, 241-246.
- [23] Cebrian, M., Dotu, I., Van Hentenryck, P., & Clote, P. (2008). Protein Structure Prediction on the face centered cubic lattice by local search. *Proceedings of the Conference on Artificial Intelligence* , *1*, 241-246.
- [24] David, L. P., & Kurt, B. (2000). *Monte Carlo Simulations in Statistical Physics*. United Kingdom: Cambridge University Press.
- [25] Oren, B. M., Alexander, M. D., RouX, B., & Masaktsu, W. (2001). *Computational Biochemistry and Biophysics*. New York, United State of America: Eastern Hemisphere.

- [26] Roma, F., Risau-Gusman, S., Ramirez Pastor, A., Nieto, F., & Vogel, E. (2009). The ground state energy of the Edwards-Anderson spin glass model with a parallel tempering Monte Carlo algorithm. *Physica A*, 388, 2821-2838.
- [27] Abolfazl, A., Mohamad, S., & Soodabeh, D. (2012). Magnetic nanoparticles: preparation, physical properties, and applications in biomedicine. *Nanoscale Research Letters*, 7, 144 -156.
- [28] Bashar, I., Ihab, M. O., Borhan, A. A., & Yousef, H. (2013). Magnetic Nanoparticles: Surface Effects and Properties Related to Biomedicine Applications. *Int. J. Mol. Sci.*, 14, 21266-21305.
- [29] Chen, M., Liu, J., & Sun, S. (2004). One-step synthesis of FePt nanoparticles with tunable size. *J Am Chem Soc*, 126(27), 8394-8395.
- [30] Sun, S., Zeng, H., Robinson, D., Raoux, S., & Rice, P. e. (2004). Monodisperse MFe₂O₄ (M = Fe, Co, Mn) nanoparticles. *J Am Chem Soc*, 126(1), 273-279.
- [31] Drokina, T., Petrakovskii, G., Molokeyev, M., Arauzo, A., & Bartolomé, J. (2015). Spin-glass magnetism in RFeTi₂O₇ (R=Lu and Tb) compounds. *Physics procedia*, 75, 580-588.
- [32] Wenfei, L., Wang, J., Jing, Z., & Wang, W. (2015). Molecular simulations of metal coupled protein folding. *Current opinion in structural biology*, 30, 25-31.
- [33] Crescenzi, P., Goldman, D., Papadimitriou, C., Piccolboni, A., & Yannakakis, M. (1998). On the complexity of protein folding. *Journal of Computational Biology*, 5(3), 423-65.
- [34] Berger, B., & Leighton, T. (1998). Protein folding in the hydrophobic-hydrophilic (HP) model is NP-complete. *J. Comp. Biol.*, 5(1), 27-40.
- [35] Jingfa, L., Beibei, S., Zhaoxia, L., Weibo, H., Yuanyuan, S., & Wenjie, L. (2013). Energy-landscape paving for prediction of face-centered-cubic hydrophobic-hydrophilic. *Physical Review E*, 88, 052704.
- [36] Istrail, S., & Lam, F. (2009). Combinatorial algorithms for protein folding in lattice models: A survey of mathematical results,. *Commun. Inf. Syst.*, 9(4), 303-346.
- [37] Dill, K. A. (1985). Theory for the folding and Stability of globular proteins. *Biochemistry*, 24(6), 1501-9.
- [38] Ying, W. L., Thomas, W., & David, L. P. (2011). Monte Carlo simulation of the HP model (The "Ising model" of protein folding). *Computer Physics Communication*, 182, 1896-1899.
- [39] Michael, P. A., & Adam, D. (2012). Wang-Landau Simulations of Adsorbed and Confined Lattice Polymers. *Physics Procedia*, 34, 6-13.
- [40] Beutler, J., & Dill, K. (1996). Hydrophobic core biased Monte Carlo search: A fast search strategy for finding low energy structures of model proteins.
- [41] Toma, L., & Toma, S. (1996). Contact interactions method: A new algorithm for protein folding simulations. *Protein Science*, 5, 147-153.
- [42] Unger, R., & Moult, J. (1993). A genetic algorithm for 3D protein folding simulations. In soft computing-A Fusion of foundations, Methodologies and Applications. *The 5th International Conference on Genetic Algorithms* (p. 581). Morgan Kaufmann Publishers.
- [43] Mazzoni, L. N., & Casetti, L. (2006). Curvature of the energy landscape and folding of model proteins. *Physical Review Letters*, 97(21), 218, 104 - 107.
- [44] Klemm, K., Flamm, C., & Stadler, P. F. (2008). Funnels in energy landscapes. *The European Physical Journal B*, 63, 387-391.